

© 2019 Woowon Lee

IDENTIFICATION OF QUANTITATIVE SECOND-HARMONIC GENERATION IMAGING
METRICS FOR COLLAGENOUS TISSUE

BY

WOOWON LEE

DISSERTATION

Submitted in partial fulfillment of the requirements
for the degree of Doctor of Philosophy in Mechanical Engineering
in the Graduate College of the
University of Illinois at Urbana-Champaign, 2019

Urbana, Illinois

Doctoral Committee:

Associate Professor Kimani C. Toussaint, Chair
Professor Amy J. Wagoner Johnson
Professor Brendan A. Harley
Assistant Professor Mariana E. Kersh

ABSTRACT

Second-harmonic generation (SHG) imaging has high specificity to collagen, sub-micrometer resolution, and optical sectioning capability. It is applied to various unstained collagenous specimens to explore the microstructure. Since collagen is one of the most abundant proteins in biological tissue, understanding its spatial organizational structure could lend insight into its intrinsic mechanical properties and thus its potential function in various biological systems. It therefore is important to extract information on collagen organization from the obtained SHG images quantitatively.

Previously, our group, the PROBE Lab at Illinois, developed a technique using (spatial) Fourier transform combined with SHG imaging (FT-SHG) to measure the collagen fiber orientation quantitatively. Recently, I expanded this approach by adapting new parameters on two-dimensional (2D) images and significantly broadening the three-dimensional (3D) analysis of 3D-SHG images. Ultimately, these parameters such as circular and spherical variance become the building blocks for a catalog of useful quantitative SHG metrics. In this thesis, I identified measures and introduced the corresponding quantitative metrics for both 2D and 3D analysis of volumetric SHG images of collagen structure in various tissues. This work was applied to quantitatively categorize collagen fiber crimping, examine collagen fiber damage, growth and where possible, find correlations of the collagen structure with the mechanical properties of the tissue.

In an initial study, I quantitatively characterized crimp patterns occurring in ligament tissue using SHG microscopy. I developed a simple algorithm using FT-SHG to quantitatively classify the fiber crimp patterns in ligament into three classifications based on the collagen fiber alignment and crimp direction. The algorithm considered the non-collagenous regions and the collagen fiber

alignment in the 2D-SHG images of the 3D stack. This work revealed the 3D structural variation and the underlying helicity in the crimp patterns.

In another study, I applied quantitative 3D-SHG imaging of collagen fibers to assess potential damage induced by electron-beam (e-beam) irradiation from environmental-scanning electron microscopy (ESEM). In this case, the 2D metrics employed to analyze the structural alteration of tissues were obtained by measuring the SHG signal intensity and the intensity distribution in the spatial-frequency domain. SHG images obtained before and after ESEM e-beam exposure in low-vacuum mode, disclosed evidence of cross-linking of collagen fibers. Meanwhile, wet-mode ESEM appeared to radically alter the structure from a regular fibrous arrangement to a more random fiber orientation. This work provided insight on both the limitations of the ESEM for tissue imaging, and the potential opportunity to use as a complementary technique when imaging fine features in the non-collagenous tissue samples.

Lastly, I expanded the quantitative SHG analysis in three-dimensions to assess the 3D collagen organization in a manner that is consistent with direct observation from images, and applied this analysis on complex 3D collagenous structures. The algorithm that analyzes the 3D fiber organization simulated five classifications of fiber organization that are in natural tissues. The quantitative metrics used were based on 3D fiber orientation and spread to differentiate each classification in a repeatable manner. As a validation process, I applied SHG images of tendon tissue cut in specified orientations and found a strong agreement between the classification algorithm and the physical fiber structure. My 3D fiber analysis approach was further expanded to mouse bile ducts at different stages of growth. It was found that the obtained 3D parameters gradually changed with age, indicating as the fibers grow, the collagenous volume and the amount of fiber crimping increases. In yet another study, I have adapted my 3D-SHG analysis method to

analyze localized regions of rat cervix tissue, the results of which have been co-registered with the corresponding measured mechanical properties obtained via nanoindentation. The 3D-SHG parameters obtained were found to be significantly different in distinctive spatial regions of the cervix, and the results from the SHG data were found to be positively correlated with the mechanical properties. This work has the potential to contribute to understanding of collagen remodeling in cervix during pregnancy, and thus this could lead to developing improved methods for preterm birth prediction.

Finally, I discussed the future directions of the quantitative 3D-SHG image analysis, and the potential of the analysis method to be applied to other imaging modalities.

ACKNOWLEDGMENTS

There are so many people that I can think of who helped me during my Ph.D. First, I would like to express my gratitude to my Ph.D. advisor, Professor Kimani Toussaint. He introduced me to the field of optics and microscopy with patience and encouragement. His guidance in research taught me how to start and accomplish research projects and to present and write academically. He has been a true mentor to me not only in research but life in general. He also provided me fruitful advises on future careers and support on job search. I really wish him and his family a bright future.

I also would like to sincerely appreciate my research collaborators, committee members, and staff: Professor Mariana Kersh and Hafiz Rahman with great incites on biomechanics, Dr. Wells and Jessica Liewellyn introducing me to true biological problems and Dr. McFarlin, Professor Amy Wagoner Johnson, and Amir Ostadi Moghaddam for having a great collaborative work on the BWF project. I really enjoyed working on it, especially in the last phase! I would also like to express my gratitude to my thesis committee members, including Professor Brendan Harley, for providing me great feedback and comments on my work. I also enjoyed working with the staff at IGB, Beckman ITG, and the MechSE department.

In addition, I would like to thank my current and former fellow PROBE lab members: Emeka Okoro, Mohammad Mahfuzul Kabir, Qing Ding for coming along the way for most of my Ph.D. years, and Varun Kelkar, Hemang Rajput, Zixi Lin, Adriana Coariti, Gopala Inavalli, Hao Chen, Brian Roxworthy and Abdul Bhuiya.

Finally, I would like to thank my family, including my parents back at Korea and my sister, brother in law, and niece showing their support. Also, I would like to thank my girlfriend, Hyojung Kim, for her support and wonderful times we spent together during graduate school.

TABLE OF CONTENTS

| | |
|--|----|
| CHAPTER 1. INTRODUCTION | 1 |
| CHAPTER 2. BACKGROUND..... | 4 |
| 2.1 Collagen | 4 |
| 2.2 Second-harmonic generation | 6 |
| 2.3 Second-harmonic generation microscopy | 17 |
| 2.4 Quantitative second-harmonic generation imaging..... | 19 |
| 2.5 Two-dimensional versus three-dimensional quantitative imaging..... | 22 |
| CHAPTER 3. APPLICATION OF QUANTITATIVE SECOND-HARMONIC GENERATION IMAGING TO FIBER CRIMP ASSESSMENT IN POSTERIOR CRUCIATE LIGAMENT | 24 |
| 3.1 Introduction..... | 24 |
| 3.2 Methods | 25 |
| 3.3 Results and discussion..... | 29 |
| 3.4 Conclusion | 38 |
| CHAPTER 4. ASSESSMENT OF ELECTRON-BEAM IRRADIATION ON COLLAGENOUS TISSUES USING QUANTITATIVE SECOND-HARMONIC GENERATION IMAGING | 39 |
| 4.1 Introduction..... | 39 |
| 4.2 Methods | 41 |
| 4.3 Results and discussion..... | 43 |
| 4.4 Conclusion | 54 |
| CHAPTER 5. QUANTITATIVE CLASSIFICATION OF 3D COLLAGEN FIBER ORGANIZATION | 56 |
| 5.1 Introduction..... | 56 |
| 5.2 Methods | 58 |
| 5.3 Results and discussion..... | 63 |
| 5.4 Conclusion | 75 |

| | |
|---|------------|
| CHAPTER 6. 3D COLLAGEN FIBER ORGANIZATION ANALYSIS APPLIED ON MOUSE EXTRAHEPATIC BILE DUCTS | 76 |
| 6.1 Introduction..... | 76 |
| 6.2 Methods | 77 |
| 6.3 Results and discussion..... | 79 |
| 6.4 Conclusion | 85 |
| CHAPTER 7. 3D COLLAGEN FIBER ORGANIZATION ANALYSIS APPLIED ON NON-PREGNANT RAT CERVIX | 86 |
| 7.1 Introduction..... | 86 |
| 7.2 Methods | 88 |
| 7.3 Results and discussion..... | 91 |
| 7.4 Conclusion | 97 |
| CHAPTER 8. CONCLUSION AND FUTURE WORK | 99 |
| 8.1 Summary | 99 |
| 8.2 Future directions | 102 |
| APPENDIX A. THIRD-HARMONIC GENERATION IMAGING OF BREAST TISSUE BIOPSIES | 104 |
| REFERENCES | 113 |

CHAPTER 1. INTRODUCTION

Due to advancement in laser technology using ultrashort pulses, non-linear optical phenomena such as second-harmonic generation (SHG) became accessible to researchers in various experiments starting from the 1960s [1]. SHG is a second-order non-linear optical process occurring in a non-centrosymmetric medium (or sample), where the signal generated as a result of this process is at half the wavelength of the incident optical field [1,2]. As a microscopy technique, SHG imaging has become increasingly used on biological tissue samples. This is because SHG microscopy has various advantages including sub-micrometer spatial resolution, optical sectioning capability, and high specificity to collagen [2,3]. This specificity makes SHG imaging unique since collagen is one of the most abundant proteins in biological tissue [4] and is the primary load bearing component making it responsible for the biomechanical function in many types of tissues [5,6]. Thus, it is necessary to quantitatively analyze the obtained SHG images, which relays information about the collagen structure.

Most SHG microscopy studies have been conducted qualitatively [7–9], which refers to observing and analyzing SHG images with no or trivial subsequent quantitation (e.g., for digital image enhancement techniques). Solely for visualization purposes, qualitative imaging may be sufficient. However, by a lack of quantitation, images are evaluated subjectively by the individual observer, and could prevent accurate and standardized assessment from measurements.

Initial approaches to extract quantitative parameters from fibrous microstructural images primarily measure the SHG signal intensity, which includes the forward-to-backward propagating signal ratio [10,11], as well as the ratio to other fluorescence techniques [12,13]. These parameters are related to properties such as collagen density and fiber packing. There have also been studies

using basic morphological features such as fiber diameter [14], orientation [15], and collagen area fraction [16].

Notwithstanding the significance of these studies, there is very limited research that analyzes and quantifies the mechanically significant features such as crimping or cross-linking occurring on the collagen fibers. Since collagen, along with elastin fibers, contributes significantly to the mechanical strength of the overall tissue [17,18], characterizing mechanically significant features in collagen structures is important. In addition, most studies seldom apply quantitative analysis in three-dimension. Two-dimensional (2D) images in microscopy have been the standard for measuring objects in the image. However, quantitative analysis through 2D images may lead to inaccurate results due to the information loss when converting a three-dimensional (3D) object to a 2D image. Observing and analyzing tissues in three-dimensions would provide more insight to understanding the structure of the tissue while avoiding some artifacts such as surface errors due to cutting during tissue preparation.

Our group (PROBE Lab at Illinois) has previously shown that SHG combined with spatial Fourier transform (FT) analysis, FT-SHG, is a simple and powerful tool for analyzing collagen fiber organization in tendon [19], bone [5], and breast tissue [20]. Moreover, we have demonstrated how to apply FT-SHG on 3D-SHG images [21,22].

This thesis focuses on developing new 2D parameters and algorithms using the FT-SHG approach and extending the analysis to three-dimensions to quantitatively evaluate the 3D collagen spatial organization. This analysis is applied to various collagenous tissues including ligament, tendon, bile duct, and cervix and correlates the quantitative measurements with fiber damage, growth, and mechanical properties of the tissue. Chapter 2 describes the background of collagen, SHG and how it is applied as a microscopy technique. In Chapter 3, we discuss applying SHG

microscopy to analyze the collagen fiber crimp pattern in the porcine ligament using quantitative information determined in the Fourier domain [23]. Chapter 4 explores quantitatively assessing the effect of the electron-beam (e-beam) exposure to collagen fibers in tendon tissue by using SHG imaging [24]. Chapter 5 summarizes the 3D-image analysis, which can quantitatively assess different types of collagen organization. The 3D-image analysis is applied to mouse bile duct and rat cervix in Chapter 6 and Chapter 7 to explore how the fiber growth and measured mechanical properties are correlated to the 3D collagen structure. Lastly in Chapter 8, the quantitative SHG metrics that are identified to be useful in each application are tabulated in the conclusion and some potential future directions of the work are discussed.

CHAPTER 2. BACKGROUND

2.1 Collagen

2.1.1 Structure

Collagen is the most prominent protein in human bodies making up to around 30% of all the body's protein. It is the main component of the extracellular matrix (ECM) and can be found in various tissues such as tendon, skin, and bone. The molecule structure also known as tropocollagen, comprises three polypeptide chains arranged in a triple helix format [25–27] illustrated in Fig. 2.1 where each polypeptide chain has amino acids. The tropocollagen molecule is 300-nm long and 1.5 nm in diameter. Depending on the amino acids and how crystalline they are, collagen is separated into more than 25 different types. For example, collagen type I has a heterotrimeric chain, whereas collagen type II has a homotrimeric chain, indicating three α -chains forming the triple helix molecule.

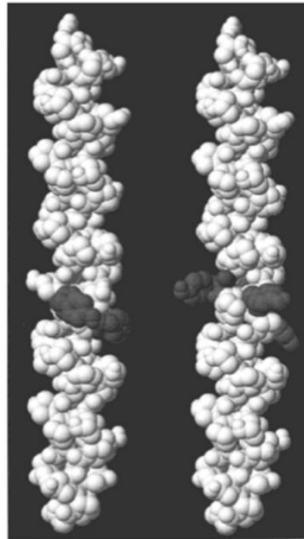


Figure 2.1: Collagen molecule showing a triple helical structure. Adapted from [26].

The collagen molecules congregate into different forms such as fibrils, mesh-like network, and beaded filaments [28]. The fibril-forming collagen will be the focus of this thesis. Fibrillar collagen is a long rope-like structure which has a continuous triple helix. The range of the fibril diameter is from 50 to a few hundred nanometers and are the elementary building block of the complex hierarchical structure. These fibrils assemble into fibers which range from 0.25 – 100 μm . The hierarchy of fibrillar collagen structure is shown in Fig. 2.2.

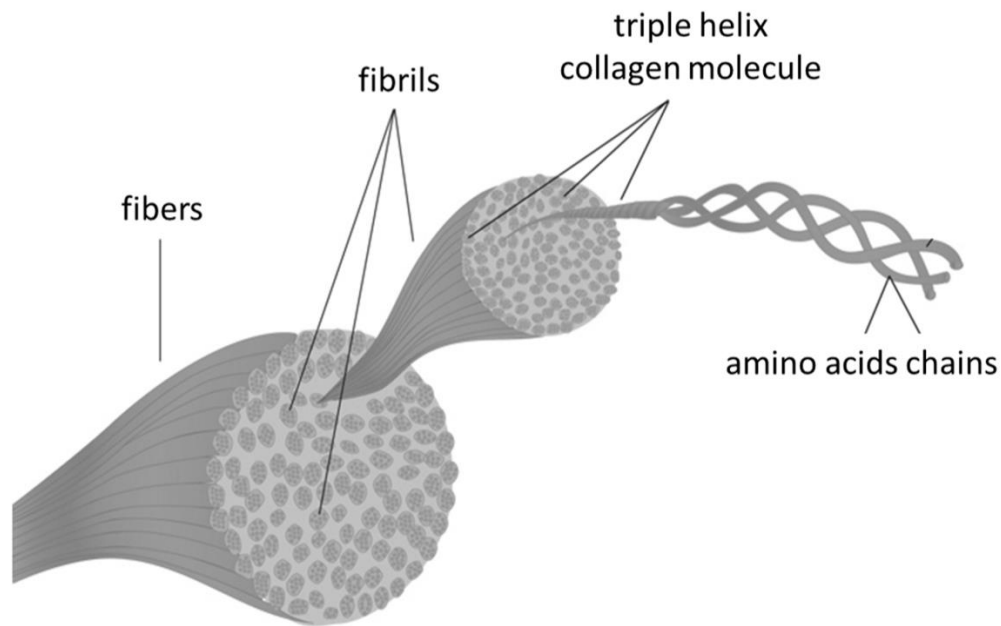


Figure 2.2: Hierarchy of fibrillar collagen. Adapted from [29].

2.1.2 Function of collagen

The word *collagen* comes from the ancient Greek word ‘kolla’, which refers to ‘glue’. This is perfectly related to its function to hold the human body together, providing firmness and strength, like glue. The mechanical role of collagen varies by the tissue in terms of mechanical stability, strength, and toughness. In ligament and tendon, collagen transmits load from muscles to bones

and stores elastic energy. This functionality helps us walk smoothly without any damage to the tissue [30]. Also, in bones and dentin, collagen provides the fracture resistance and tensile stiffness [30,31]. Collagen also is in skin to provide a firm structure and is responsible for wrinkles during aging since the collagen production decreases, which weakens the connection [32]. As such, each tissue has a different mechanical requirement such as some need to be elastic and store mechanical energy, while other tissues have to be stiff and tough; collagen changes based on this requirement.

Also, the collagen structure in ECM is responsible for various cellular activities such as cell attachment, differentiation, migration, and survival [33,34]. Specifically, studies have proven that the collagen network in ECM directs tumor cell migration [35] and orientation of collagen fibers promote cell and collagen interaction [36]. Also, researchers have revealed that the collagen environment affects the proliferation in certain cells such as human skin fibroblasts [37].

Mutations in the structure of collagen are associated with various types of diseases. In bone, collagen crosslinking and fibril size decreasing affect the bone stiffness and the resistance to fracture, thus leading to osteoporosis and osteogenesis imperfecta [33,38]. In addition, the collagen structure in cornea degrading due to the mutations in structure and composition may result in keratoconus, where the cornea bulges to a cone-like shape [39,40]. Also, collagen is related to fibrotic disorders, tumor stroma, and fibrosis due to the synthesis rate imbalance and breakdown [41].

2.2 Second-harmonic generation

2.2.1 Introduction

When an electric field (\vec{E}) is applied to a material, it will have an optical response, polarization density (\vec{P}). The polarization density is the sum of the dipole moments. When the applied electric

field is small, then the applied field and polarization density has a linear relationship as shown in equation 2.1

$$\vec{P} = \vec{P}^{(L)} = \varepsilon_0 \chi^{(1)} \vec{E} \quad (2.1)$$

where ε_0 is the permittivity in free space and $\chi^{(1)}$ is the linear susceptibility and has a relation with the material refractive index as $n = \sqrt{1 + \chi^{(1)}}$. The linear optical properties can also be explained as the classical harmonic oscillator, where the mass suspended on a spring is analogous to the atom surrounded by the electron cloud. The applied force to a harmonic oscillator to stretch the spring is equivalent to the applied electric field, forming a displaced electron cloud [42].

When a higher electric field is applied, comparable with the interatomic field, the non-linear terms come into play as in equation 2.2. This includes the second harmonic term indicating second-harmonic generation (SHG).

$$\vec{P} = \vec{P}^{(L)} + \vec{P}^{(NL)} = \varepsilon_0 (\chi^{(1)} \vec{E} + \chi^{(2)} \vec{E}^2 + \chi^{(3)} \vec{E}^3 + \dots) \quad (2.2)$$

$\chi^{(n)}$ is the non-linear susceptibility and is a n+1 order tensor.

On the energy diagram [Fig. 2.3], SHG is described as two photons exciting the sample simultaneously to virtual state and generating a single photon, which is exactly the two times the frequency as the incident photons [Fig. 2.3(a)]. As compared to two-photon-excited fluorescence (TPEF) illustrated in Fig. 2.3(b), there is no energy absorption onto the sample, making it a coherent process with no photobleaching.

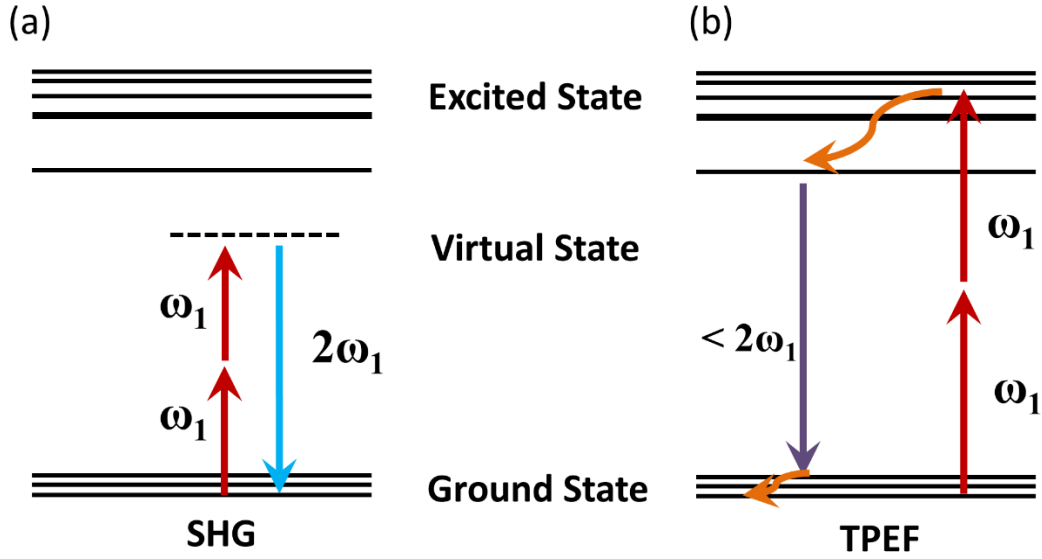


Figure 2.3: Energy diagram of (a) SHG and (b) TPEF.

2.2.2. Wave equation for SHG

In order to mathematically describe the SHG signal propagate through media, we begin with Maxwell's equations:

$$\nabla \cdot \vec{D} = \vec{\rho} \quad (2.3)$$

$$\nabla \cdot \vec{B} = 0 \quad (2.4)$$

$$\nabla \times \vec{E} = -\frac{\partial \vec{B}}{\partial t} \quad (2.5)$$

$$\nabla \times \vec{H} = -\frac{\partial \vec{D}}{\partial t} + \vec{J} \quad (2.6)$$

where \vec{D} is the electric flux density, \vec{B} is the magnetic flux density, and \vec{H} is the magnetic field. $\vec{\rho}$ and \vec{J} are the free charge and current, respectively, and since we assume that there is no free charge and current in the sample, both become 0. Also, the electric and magnetic flux density is related to the fields as follows:

$$\vec{B} = \mu_0 \vec{H} \quad (2.7)$$

$$\vec{D} = \epsilon_0 \vec{E} + \vec{P} \quad (2.8)$$

where μ_0 is the magnetic permittivity. To drive the wave equation, we take the curl on equation (2.5) and since $\nabla \times \vec{B}$ is interchangeable with $\mu_0 \frac{\partial \vec{D}}{\partial t}$ we can obtain

$$\nabla \times \nabla \times \vec{E} + \mu_0 \frac{\partial^2 \vec{D}}{\partial t^2} = 0 \quad . \quad (2.9)$$

The speed of light in vacuum c is

$$c = \frac{1}{\sqrt{\mu_0 \epsilon_0}} \quad . \quad (2.10)$$

Thus, after applying equation (2.8), (2.10), equation (2.9) can be rewritten as

$$\nabla \times \nabla \times \vec{E} + \frac{1}{c^2} \frac{\partial^2 \vec{E}}{\partial t^2} = -\frac{1}{\epsilon_0 c^2} \frac{\partial^2 \vec{P}}{\partial t^2} \quad . \quad (2.11)$$

This is the general form of the wave equation. To further simplify the wave equation, we can apply vector algebra to convert $\nabla \times \nabla \times \vec{E}$ to $\nabla(\nabla \cdot \vec{E}) - \nabla^2 \vec{E}$ and due to the slowly varying amplitude approximation, $\nabla \cdot \vec{E} = 0$, equation 2.11 becomes

$$\nabla^2 \vec{E} - \frac{1}{c^2} \frac{\partial^2 \vec{E}}{\partial t^2} = \frac{1}{\epsilon_0 c^2} \frac{\partial^2 \vec{P}}{\partial t^2} \quad . \quad (2.12)$$

After separating \vec{P} to linear and non-linear terms, equation (2.12) is rewritten as follows:

$$\nabla^2 \vec{E} - \frac{1}{c^2} \frac{\partial^2 \vec{E}}{\partial t^2} = \frac{1}{\epsilon_0 c^2} \frac{\partial^2 \vec{P}^{(L)}}{\partial t^2} + \frac{1}{\epsilon_0 c^2} \frac{\partial^2 \vec{P}^{(NL)}}{\partial t^2} \quad . \quad (2.13)$$

Considering the relative permeability $\epsilon_r = n^2 = 1 + \chi^{(1)}$ and applying equation (2.1), equation (2.13) results in

$$\nabla^2 \vec{E} - \frac{n^2}{c^2} \frac{\partial^2 \vec{E}}{\partial t^2} = \mu_0 \frac{\partial^2 \vec{P}^{(NL)}}{\partial t^2} \quad . \quad (2.14)$$

This is the non-linear wave equation. For second-harmonic generation, the electric field in space and time can be considered as

$$\vec{E}_1(z, t) = A_1 e^{-i(k_1 z - \omega_1 t)} + \text{c. c} \quad (2.15)$$

where A_1 is the amplitude of the electric field, z is the propagating direction, k_1 is the z -component of the wave vector and c. c is the complex conjugate. The subscript 1 refers to the property at wavelength, ω_1 . Also, the second-order induced polarization density $\vec{P}^{(2)}$ can be written as

$$\vec{P}^{(2)} = \epsilon_0 \chi^{(2)} \vec{E}^2 = 2\epsilon_0 d_{eff} \vec{E}^2 = 2\epsilon_0 d_{eff} A_1^2 e^{-i2k_1 z} \quad (2.16)$$

where d_{eff} is the effective scalar value for the second-order susceptibility, $\chi^{(2)}$. For SHG, the second-order polarization can be expressed as

$$\vec{P}_2 = P_2 e^{-i\omega_2 t} + \text{c. c} \quad (2.17)$$

where $\omega_2 = 2\omega_1$. After applying equation (2.15), (2.16), and (2.17) to the non-linear wave equation and further simplification, we obtain

$$\left[\frac{\partial^2 A_2}{\partial z^2} + 2ik_2 \frac{\partial A_2}{\partial z} - k_2^2 A_2 + \frac{n_2^2 \omega_2^2 A_2}{c^2} \right] e^{-i(k_2 z - \omega_2 t)} + \text{c. c} =$$

$$\frac{-2d_{eff} \omega_2^2}{c^2} A_1^2 e^{-i(2k_1 z - \omega_2 t)} + \text{c. c} \quad . \quad (2.18)$$

The third and fourth term cancel out and due to the slowly varying amplitude approximation,

$$\left| \frac{\partial^2 A_2}{\partial z^2} \right| \ll \left| k_2 \frac{\partial A_2}{\partial z} \right| \quad (2.19)$$

equation (2.18) becomes

$$\frac{\partial A_2}{\partial z} = \frac{id_{eff} \omega_2^2}{k_2 c^2} A_1^2 e^{-i(2k_1 - k_2)z} \quad . \quad (2.20)$$

2.2.3 Phase matching condition

By integrating equation (2.20) from $z=0$ to $z=L$, we yield

$$A_2(L) = \frac{id_{eff} \omega_2^2}{k_2 c^2} A_1^2 \int_0^L e^{-i(2k_1 - k_2)z} dz = \frac{id_{eff} \omega_2^2}{k_2 c^2} A_1^2 \left(\frac{e^{i(2k_1 - k_2)L} - 1}{i(2k_1 - k_2)} \right) \quad . \quad (2.21)$$

Due to the fact that the intensity is the magnitude of the time-averaged Poynting vector,

$$I = 2n\varepsilon_0 c |A|^2 \quad (2.22)$$

the intensity of ω_2 , the SHG intensity, can be expressed as

$$I_2 = 2n_2 \varepsilon_0 c |A_2|^2 = 2n_2 \varepsilon_0 c \left| \frac{id_{eff} \omega_2^2}{k_2 c^2} A_1^2 \left(\frac{e^{i\Delta k L} - 1}{i(2k_1 - k_2)} \right) \right|^2 =$$

$$\frac{2n_2 \varepsilon_0 d_{eff}^2 \omega_2^4 A_1^4}{k_2^2 c^3} L^2 \text{sinc}^2 \left(\frac{\Delta k L}{2} \right) \quad (2.23)$$

where

$$\Delta\vec{k} = 2\vec{k}_1 - \vec{k}_2 \quad (2.24)$$

which is known as the phase or momentum mismatch. Therefore, the SHG intensity I_2 is proportional to the sinc function and is maximum when $\Delta\vec{k} = 0$. This is known as perfect phase matching in SHG. For the perfect phase match to occur, the refractive indexes should also be the same, $n_1 = n_2$ resulting in a non-dispersive material. For dispersive materials, perfect phase matching can be achieved by adjusting the polarization of the incident light in uniaxial birefringent crystals such as potassium dihydrogen phosphate (KDP) and barium boron oxide (BBO) [3].

2.2.4 Relaxed phase matching

Perfect phase matching is a special case and in most materials including biological samples, the refractive index n varies on different wavelengths ($n_1 \neq n_2$) [43]. Also, the molecules are not perfectly aligned in a regular format like birefringent crystals. In these cases, Δk cannot be 0 and this is called the relaxed phase matching condition. We introduce the coherence length (L_{coh}) which indicates the maximum length of SHG intensity to have a constructive interference and is as follows:

$$I_2 = \frac{2n_2\varepsilon_0d_{eff}^2\omega_2^4A_1^4}{k_2^2c^3}L_{coh}^2\text{sinc}^2\left(\frac{\Delta kL_{coh}}{2}\right) = 0 \quad (2.25)$$

thus,

$$L_{coh} = \frac{2\pi}{\Delta k} \quad (2.26)$$

The L_{coh} varies from 5 to 15 μm in biological tissues and 30 μm in water [44]. When the sample has a periodic arrangement which matches with the L_{coh} , the SHG is consistently constructive along the propagation direction. This is called quasi-phase matching [3].

Because of the randomness of biological tissues, Δk is not a single value and a distribution and the SHG intensity, I_2 , is the total sum of all the Δk contributions. To examine how the Δk values affect the SHG intensity, we can mathematically compare how different the SHG intensity is in Δk_1 and $2\Delta k_1$ as a function of propagation length L . The result shows that the maximum SHG occurs by Δk_1 at L_{coh} , while the SHG by $2\Delta k_1$ is only half the value and oscillates in a sinusoidal fashion due to its shorter L_{coh} . Therefore, in the domain of the order of the L_{coh} , the SHG will mainly come from the smaller Δk , which comes from the dispersion in the material [3].

2.2.5 Non-centrosymmetry

To make SHG occur, the crystal structure of the sample has to be non-centrosymmetric. Centrosymmetry refers to a structure having an inversion point shown as Fig. 2.4. Thus, non-centrosymmetric is defined as having no inversion point such as mirror or polar symmetry.

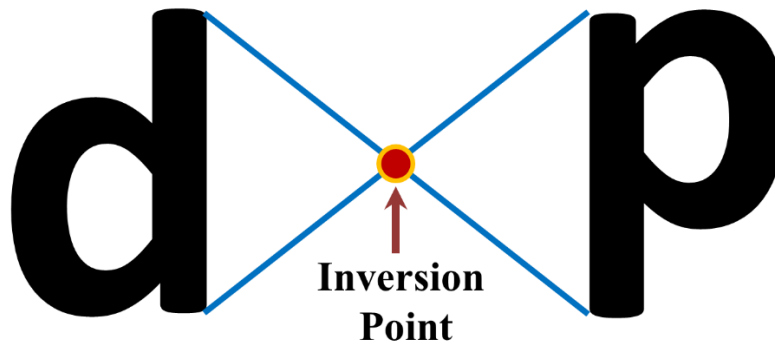


Figure 2.4: Centrosymmetric example with an inversion point.

Mathematically, a centrosymmetric medium is analyzed as, when the applied electric field at a location (x, y, z) has a polarization density \vec{P} , then the electric field applied at $(-x, -y, -z)$ should have $-\vec{P}$. Since the electric field \vec{E} is squared, the only case when \vec{P} and $-\vec{P}$ can be equal is when the second order susceptibility is 0. Thus, only non-centrosymmetric material can have a non-zero second-order susceptibility. This is demonstrated as

$$\vec{P} = \epsilon_0 \chi^{(2)} \vec{E}^2 = \epsilon_0 \chi^{(2)} (-\vec{E})^2 = -\vec{P} \quad . \quad (2.27)$$

Non-centrosymmetric structures include KDP or BBO crystals but also exist in biology such as collagen fibers [45], myosin [46], and microtubules in cells [47].

Researchers have pointed out the collagen molecules are arranged to have *pseudo-tetragonal* packing structure, which is verified by X-ray scattering [48,49]. However, on the order of the SHG microscopy illumination wavelength (700~800 nm), the local symmetries disappear and collagen is generally viewed as a cylindrical symmetry [50]. Therefore, collagen has a non-centrosymmetric structure and has an SHG signal.

2.2.6 Directionality

In ideal case, the SHG signal propagates in the forward direction, the same direction as the input light. This is because in the perfect phase match condition, $\Delta\vec{k} = 0$, \vec{k}_1 and \vec{k}_2 have to be in the same direction thus, the SHG signal is in the same direction as the incident light. This is demonstrated in Fig. 2.5. Non-linear optical media such as BBO crystals have only forward SHG signal.

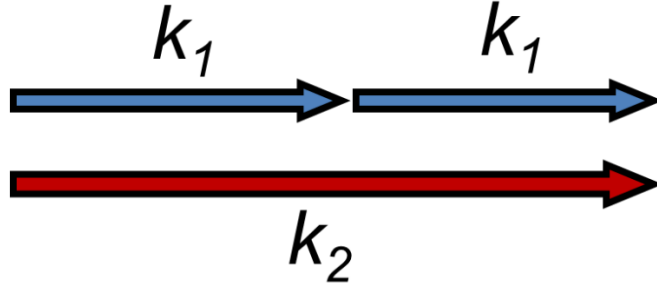


Figure 2.5: Forward SHG due to phase matching.

In some cases, there is also backward SHG signal, which is the reverse direction of the incident light. This can be explained in a few ways. Since SHG is a momentum conservation process, for the relaxed phase matching, $\Delta k \neq 0$, the SHG efficiency in the forward direction decreases, which indicates that the backward SHG is generated [51]. To form backward SHG, the sample has to provide a sufficiently large enough axial momentum, K , to change the direction of the photons propagating. Thus, the relaxed phase matching condition in the forward and backward case can be written as follows:

$$\Delta \vec{k}_f = \vec{K}_f - (\vec{k}_{2\omega} - 2\vec{k}_\omega) \quad (2.28)$$

$$\Delta \vec{k}_b = \vec{K}_b - (\vec{k}_{2\omega} + 2\vec{k}_\omega) \quad (2.29)$$

where $\Delta \vec{k}_f$, $\Delta \vec{k}_b$ represent the phase mismatches for the forward and backward SHG generation, respectively. \vec{K}_f and \vec{K}_b are the axial momentum for forward and backward direction. Compared to forward scattering, backward scattering needs a higher axial momentum, thus, $K_b > K_f$. This implies $\Delta k_b > \Delta k_f$ according to equation 2.28 and 2.29. As a result, forward SHG has a longer L_{coh} than backward SHG. As previously discussed in Section 2.1.4, small Δk elements dominate the SHG intensity in the order of its L_{coh} and this is essentially referring to the forward SHG. On

the other hand, backward SHG occurs when the size of the domain is smaller than the forward L_{coh} and comparable with the backward L_{coh} . This indicates that backward SHG, compared to forward SHG, is more sensitive to fine features on the sample which are in the range of the backward L_{coh} .

In addition, when the incident light with a Gaussian profile is tightly focused by a high NA objective lens, phase retardation of π occurs in the focal volume, a phenomenon known as Gouy shift [2]. Due to the phase lag in the incident light, the forward SHG starts to propagate at an angle and can eventually propagate backward depending on the molecular distribution [2].

Lastly, backward SHG is generated due to the forward SHG scattering backward [Fig. 2.6]. The forward scattered SHG loses phase information so is no longer coherent and becomes significant when the sample is thick [52–55], generally thicker than 100 μm . This is because, once the sample is thick, there is more space of the forward SHG to scatter backward. In contrast, for thin tissue sections, the majority of the forward SHG propagates towards the boundary of the tissue without scattering backward. Generally, backward SHG is a combination of the backward generated SHG and the backward scattered SHG. Researchers [56,57] have developed methods to measure the backward generated SHG versus backward scattered SHG and concluded that the and the percentage of each backward SHG depends on the thickness of the tissue, the optical components used for imaging and the tissue type.

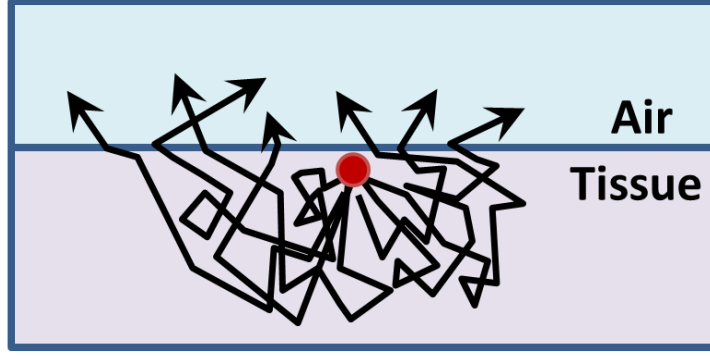


Figure 2.6: Backward SHG formed by forward SHG scattering backward. Adapted from [58].

2.3 Second-harmonic generation microscopy

2.3.1 Advantages

As an imaging technique, SHG microscopy is advantageous in many aspects. The non-linear reaction is very unlikely to happen thus to increase the probability, photons should be crowded in a limited volume. This is possible due to using femtosecond pulse lasers with an objective lens. Even for using highly advanced equipment, the SHG signal comes from a small volume compared on other linear imaging techniques. This is a huge benefit since it provides sub-micrometer spatial resolution and allows 3D imaging. The spatial resolution refers to the excitation volume, and because of the non-linear optical process, the excitation volume is smaller than the diffraction limit [3]. Researchers [59] were able to evaluate the optimum spatial resolution of SHG as follows:

$$w_{xy} = \frac{0.320\lambda_{ext}}{\sqrt{2}NA} \quad NA \leq 0.7 \quad (2.30)$$

$$w_{xy} = \frac{0.325\lambda_{ext}}{\sqrt{2}NA^{0.91}} \quad NA > 0.7 \quad (2.31)$$

$$w_z = \frac{0.532\lambda_{ext}}{\sqrt{2}} \left[\frac{1}{n - \sqrt{n^2 - NA^2}} \right] \quad (2.32)$$

where w_{xy} refers to the lateral resolution and w_z indicates the axial resolution. λ_{ext} is the excitation wavelength of the incident laser and NA is the numerical aperture of the objective lens.

In addition, the illumination of SHG lies in the therapeutic window, where there is less scattering from water and cells [60]. This allows the illumination source to penetrate deeper inside the tissue. For regular fluorescence, the emission signal is red-shifted so when illuminating the sample in the therapeutic window, the output signal will be in the near-infrared range, which requires a different set of optical components. On the contrary, SHG signal is blue-shifted thus, the output signal will be still in the visible wavelength range when illuminating the sample in the therapeutic window. The penetration depth using SHG microscopy on tissues have been reported as more than 400 μm .

2.3.2 Optical setup

A typical optical setup is demonstrated as Fig. 2.7. A femtosecond pulse laser is used to illuminate the sample. Along the beam path, a pair of lenses are used to expand the beam to fit the back aperture of the microscope. For point scan imaging, a Galvo scanner is used. The beam is focused down by an objective lens and interacts with the sample. We collect the backward SHG signal from the same objective. A dichroic mirror is used to transmit the SHG signal while reflecting the incident light. Finally, we use a laser blocking filter to filter out the remaining laser wavelength and use a bandpass filter to collect the SHG signal. In the setup shown in Fig. 2.7, since the incident wavelength is 780 nm, the SHG signal is 390 nm.

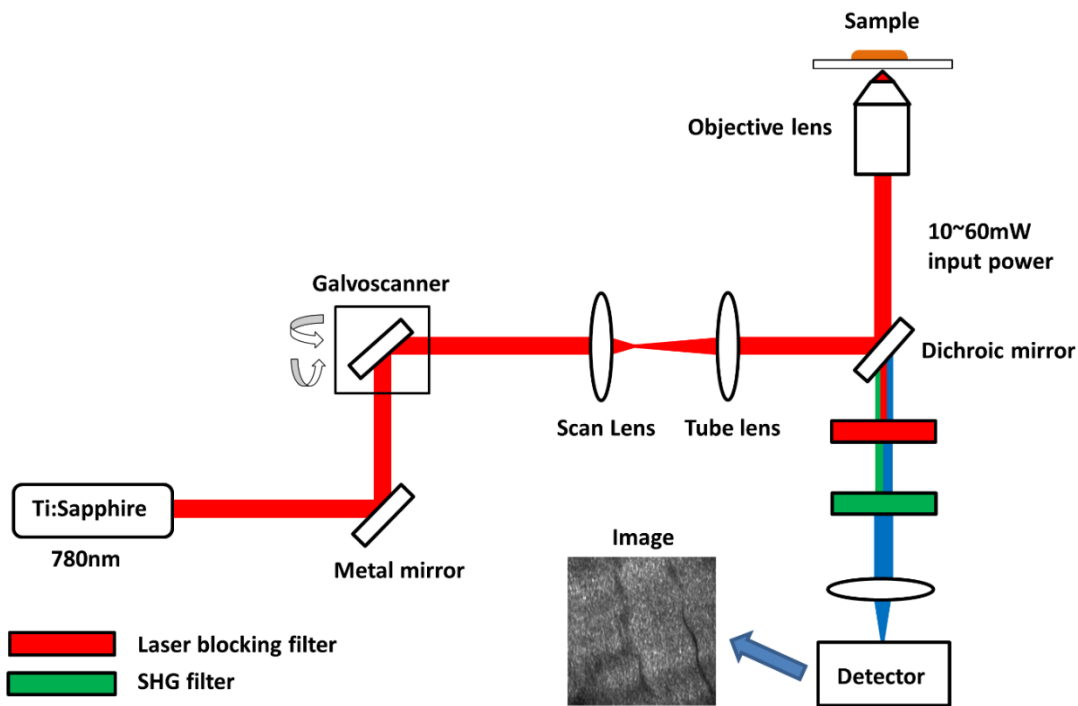


Figure 2.7: SHG optical setup. Adapted from [61].

2.4 Quantitative second-harmonic generation imaging

2.4.1 Introduction

By using the advantages of SHG microscopy, there have been a variety of studies on collagenous tissue from a biological specimen. Studies conducted on SHG microscopy identify the existence of collagen or do a characterization study and observe the structure. For instance, Han *et al.* [8] imaged collagen fibers at different locations of sclera, identifying the sharp bend in collagen fibrils. Also, Aptel *et al.* [7] imaged tendon tissue sectioned at different angles and displayed the differences in the SHG images. However, without any quantitation, images can be evaluated subjectively by the individual observer and in some cases, an optical illusion effect [62,63] could prevent accurate decisions. In Fig. 2.8(a) we see an example of such an effect, whereby a strictly qualitative assessment could lead to an inaccurate interpretation. Here, the vertical line in the left

image appears to be longer than the one in the right. In Fig. 2.8(b), the center circle diameter in the right image appears to look bigger than the one in the left. However, in fact for both sets of images, the diameter of the circle and the length of the vertical line are the same, and the surrounding features are generating an illusion effect. Therefore, for these examples, a quantitative measure of length and diameter of line and circle, respectively, would provide accurate morphological information.

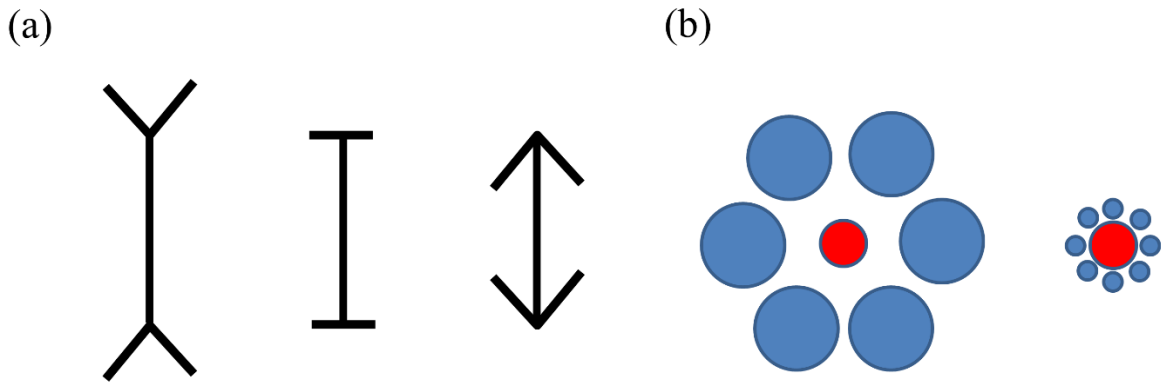


Figure 2.8: Optical illusion examples. (a) Muller-Lyer illusion and (b) Ebbinghaus illusion.

2.4.2 Previous studies on quantitative SHG

There have been a couple of approaches to extract quantitative parameters from fibrous microstructural images. Initial approaches primarily measure the SHG signal intensity, which includes the forward to backward propagating signal ratio [10,11]. Measuring the forward to backward ratio is a commonly used parameter due to its simple procedure to measure and its connection to useful features of the sample such as fiber packing, diameter, and orientation randomness. The relationship between the sample features and the SHG direction is discussed in Section 2.1.6. LaComb *et al.* measured the forward to backward ratio on mouse tissue to differentiate normal verses osteogenesis imperfecta [64]. Also, researchers have implemented

methods to combine the SHG intensity with other imaging techniques such as autofluorescence (AF). Puschmann *et al.* measured the SHG to AF on skin and was able to distinguish between different age groups of tissue [65]. There have also been studies using the morphological features such as fiber diameter [14], orientation [15] and collagen area fraction [16] measured using image processing tools such as ImageJ by manually selecting single fibers in a region of interest or CT-Fire, which implements an automated algorithm using the Curvelet transform. Provenzano *et al.* developed a parameter called tumor-associated collagen signatures (TACS), which basically measures the fiber orientation in breast tissue which is stretched around a tumor boundary [66]. The angle of collagen fibers relative to a line tangential to the tumor boundary was measured by imageJ.

Notwithstanding the significance of these studies, there are still problems to be solved in terms of connecting the actual biological function or fiber properties to the measured SHG parameters. For instance, collagen fibers along with elastin fibers contribute significantly to the mechanical strength of the overall tissue [17,18]. However, as of for now there are limited studies that link the parameters captured from the SHG images to the mechanical measurements and also very few research quantifying mechanically significant features such as cross-linking or crimp within fibers. Also, medical diagnosis such as cancer detection still relies on human (pathologist) judgment on thin-cut hematoxylin and eosin (H&E) stained tissue, which is not only time consuming but also a non-quantitative process. Although there have been some approaches looking for biomarkers on malignant tissue [66], this is only a fraction of the various stages and types of diseases that are qualitatively assessed by pathologists. Lastly, most quantitative studies are limited to 2D analysis, which can provide misleading results. The importance of 3D analysis will be explained in Chapter 2.5.

2.4.3 Fourier transform SHG

FT-SHG is a quantitative SHG imaging technique which applied FT to SHG images and computes the fiber orientation information. FT converts an image from image domain to the spatial-frequency domain. Images can be basically decomposed into a superposition of harmonic functions [67,68] and are identified in the spatial-frequency domain. Specifically, the decomposed harmonic functions are the variation of intensity in the image per unit distance [69,70]. In the spatial-frequency domain, lower frequencies are close to the origin, whereas high frequencies are far apart from the origin. By analyzing the intensity distribution in the spatial-frequency domain, our group was able to extract the preferred fiber orientation by quantifying the high amplitude spatial-frequency components.

Our group applied FT-SHG to horse tendon images to quantitatively differential normal versus injured tendon tissue [19]. Also, FT-SHG has been used on cortical bone images to assess the collagen fiber orientation and extract age-related variations [5]. Different pathological stages of breast biopsies have also been utilized for FT-SHG to distinguish malignant tissue from normal tissue [20]. Moreover, our group has introduced how to use FT-SHG to obtain the 3D fiber orientation from SHG image stacks and successfully observed in-plane and out-of-plane fibers in rat cervix [22].

2.5 Two-dimensional versus three-dimensional quantitative imaging

One aspect to consider for quantitative imaging is the dimension of the image. 2D images such as drawings and photographs are generally considered as a form of visual expression and communication. After the discovery of photography and microscopy, it was soon realized that quantitative measurements could be made on objects in the image. However, 2D images have a

number of difficulties which come from the fact that the 3D objects are projected down onto a 2D image, thus the depth information is lost and generates ambiguity [71]. For instance, a dice has different numbers on each side, and when projecting the dice on a 2D image, there is only one side seen showing a single number. Thus observers have to guess what numbers on the other sides. In microscopy, a 3D image is composed of multiple 2D images as a stack. Therefore a single 2D image only carries a fraction of the 3D image. For visualization or entertainment purposes, 2D images may be sufficient. However, for quantitative imaging, 3D imaging contains more accurate information.

Even though 3D imaging has various advantages, there is a limited amount of research conducted on 3D quantitative microscopy. This is because there are only a few techniques that have high axial resolution to generate high-resolution 3D images. This is due to the low axial resolution of focused light, incident beam penetration limit, and the interference of the out-of-focus light coming from other planes. In addition, 2D imaging has been the gold standard for measurements in many areas, and so the platform to obtain and subsequently analyze the 3D images are not well developed. That is why many studies use 3D-SHG images as a visual observation tool of the sample [72,73] rather than a quantitative data set, although SHG has a high axial resolution. Lastly, 3D-image analysis is computationally expensive.

This thesis circumvents these difficulties by using SHG microscopy, which has a high axial resolution and thus permits 3D optical imaging. We use simple methodologies such as the fast Fourier transform to analyze 3D images and develop 3D parameters that prove to be useful to determine fiber growth and quantify spatially heterogeneous tissue. Details are explained in Chapter 5-7.

CHAPTER 3. APPLICATION OF QUANTITATIVE SECOND-HARMONIC GENERATION IMAGING TO FIBER CRIMP ASSESSMENT IN POSTERIOR CRUCIATE LIGAMENT

3.1 Introduction

A ligament tissue which links bone to bone is composed of collagen fiber bundles. Its passively controls joint motion in response to muscle forces and also transmits force between the bones [74–76]. Studies show that daily activities apply repetitive and sustained loads up to a quarter of the maximum strength of ligament in knee [77,78], and for special cases such as car accidents or sports activities can exceed the limit of the maximum strength of ligament [77], resulting in severe damage and injury [79]. Hence, accurate mechanical property measurement of ligaments is important for establishing appropriate injury prevention strategies and for enhancing surgical treatment. The complex wavy crimp pattern in the collagen structural architecture of ligament strongly affects the non-linear mechanical property of ligament [80–83], thus it is critical to use proper imaging modalities to investigate the crimp pattern.

Polarized light (PL) microscopy is one imaging method researchers have used to analyze the crimp patterns in ligaments [84–88]. PL microscopy utilizes the birefringence of the sample by placing the sample between a pair of crossed linear polarizers. The imaging signal becomes highest when the fibers in the sample are 45° with respect to the crossed linear polarizers [89]. In a PL microscope image of collagen fibers, crimping pattern is shown to have extinction bands. Spenser *et al.* have been able to combine PL microscopy with tensile test and measure quantitative parameters such as fiber orientation under different loading conditions and crimp angle [86,87,90]. Scanning and transmission electron microscopes are other methods researchers used to image

This work was previously published in W. Lee, H. Rahman, M. E. Kersh, and K. C. Toussaint, Jr. [23], and is adapted here with permission

collagen fibers in ligament. Helical patterns of the collagen fibers are revealed and called ‘fibrillar crimp’, which indicates fiber undulation in different planes [91–93] [94,95]. Quantitative metrics such as the number of crimps, fibril diameter, and fiber arrangement are measured compared on the periphery and core region of ligament [94,95]. Notwithstanding the significance of these studies, PL microscopy and electron microscopy have low axial resolution, and the sample has to go through an invasive sample preparation protocol including fixation, dehydration, and coating with conductive medium [96,97]. On the other hand, SHG microscopy has a high axial resolution allowing 3D quantitative analysis of collagen fibers and also does not require sample preparation methods that can affect the sample. There have been studies using SHG imaging on ligament to measure fiber density and orientation to correlate to computed mechanical properties and evaluated the effects of smoking [98], laser damage [99] and chemicals [100].

In this chapter, we analyze the 3D spatial arrangements of collagen fibers in posterior cruciate ligament (PCL) using FT-SHG. Previously, Vidal & Mello have applied FT analysis on tendon to capture the crimp pattern variability [101,102], however the work in this study is to the best of our knowledge, a novel approach to apply FT-SHG to examine the 3D crimp pattern in ligament. Using this modality, we are able to define three distinct types of crimp behavior. We believe that our crimp pattern analysis could be a key component connecting the structural information to the mechanical properties and could aim to predict damage or injury in PCL.

3.2 Methods

3.2.1 Sample preparation

We cut five porcine knee PCL specimens (of age six months) into thirds along the proximal-distal ligament direction and embedded them in optimal cutting temperature compound [Figure 3.1] for

cryo-sectioning. The middle region between the proximal and distal portions was sectioned at 100- μ m thickness by a cryostat (CM3050S, Leica) cut along the collagen fibers. We collected the thin sections from between the anterior-posterior regions neglecting the sheath. Next, the tissue sections were placed on glass microscope slides before mounting a #1.5 coverslip on top with aqueous mounting media. We used tweezers to gently lower the coverslip on the microscope slide to avoid any air bubbles forming. After the samples dried, we applied nail polish on the corners to seal the samples. All ligaments were provided from the Meat Science Laboratory of the University of Illinois at Urbana-Champaign. This study is exempt from the Illinois Institutional Animal Care and Use Committee (IACUC).

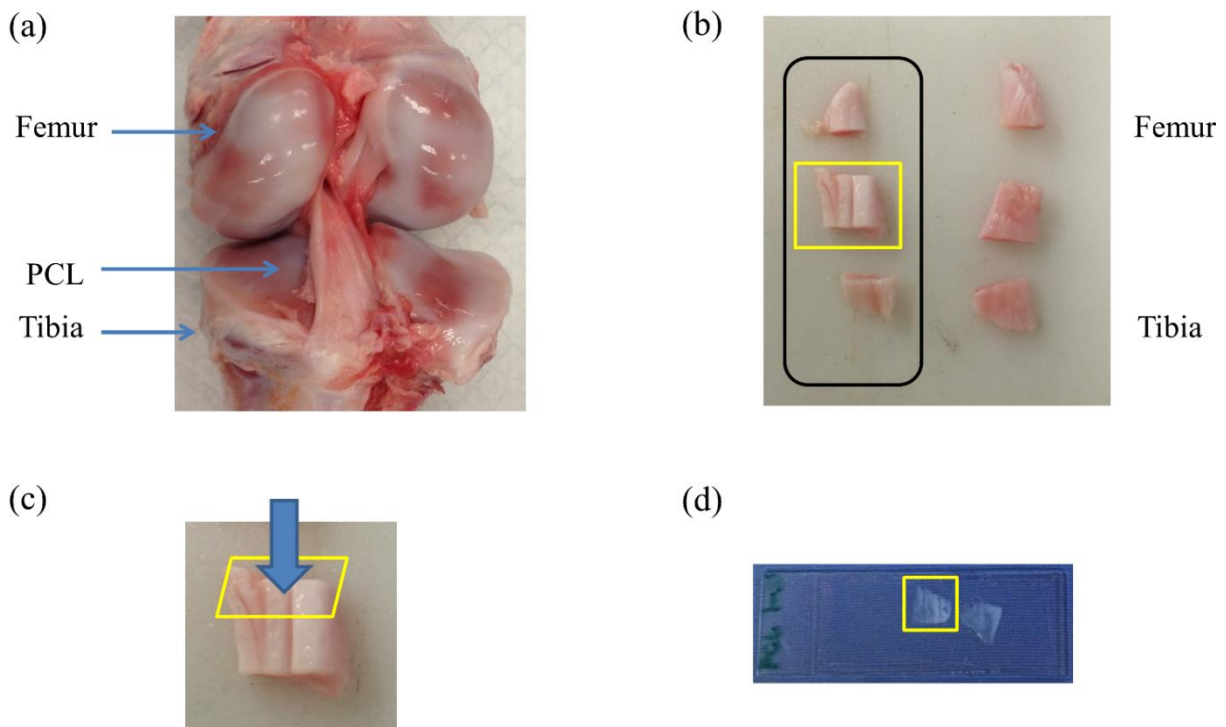


Figure 3.1: (a) Digital image showing PCL anatomy. (b) Cutting of PCL into thirds along the proximal-distal direction, and (c) sectioning of the middle piece into 100- μ m thick slices. (d) Mounting of thin sections on microscope slides with coverslips placed on top for sealing the sample. Adapted from [23].

3.2.2 Experimental setup

Selected fibrous regions were imaged by SHG microscope (IX81, Olympus). We used a tunable Ti:Sapphire laser producing 100-fs duration pulses spectrally centered at 780-nm to illuminate the sample. A 40X 0.65 NA objective lens (PLAN N, Olympus) focused down the input beam on the sample and the same objective collected the backward SHG. A 390-nm bandpass filter was placed at the collection beam path to separate the SHG signal from any generated autofluorescence. To generate an image, the beam was raster scanned by an *x-y* galvanometer scanner at ~ 1.1 mm/s and the epi-directed-SHG signal was collected by a photomultiplier tube (H10721-110, Hamamatsu). The focus drive attached on the objective moves in a step size of 500-nm along the *z*-axis shifting the focus plane to generate the 3D stack. For any single plane, four images were stitched together to form a wider area. The size of the obtained SHG 3D-image stacks were $200 \times 200 \times 30$ μm in the *x-y-z* dimension and the average power of the laser on the sample plane was ~ 10 mW.

3.2.3 Image analysis

The obtained 2D-SHG images were analyzed using a customized MATLAB code to label the crimp patterns in each region. The type discerning algorithm [Figure 3.2] first calculated the percentage of the dark pixels in the entire image. Those possessing a lower intensity than the dark threshold were defined as dark pixels. The dark threshold was a single value applied on the entire image segmenting the background to the SHG signal [97]. If the number of dark pixels was less than 10% of the entire image, the image was assigned as category A (CAT A) or category B (CAT B); conversely, when the number of dark pixels was more than 10% of the region, the image was identified as category C (CAT C). Next, spatial FT analysis was applied to the image, generating

a spatial-frequency domain image, and the corresponding 2D magnitude spectrum was integrated radially from 0° to 360° with a step size of 1° . Radial integration values lower than 30% of the maximum value were considered as noise, while those above this threshold were plotted in a polar angular plot. If the plotted curve fits strongly with a Gaussian distribution [103,104] ($r^2 > 0.95$) it was defined as CAT A. The image was defined as CAT B when the correlation was weak ($r^2 < 0.95$). For CAT C, the identical radial integration process was applied. In the range of 0° to 180° , the polar plot with two distinct peaks was further classified as CAT C-2 whereas a single peak plot was CAT C-1. The two peaks were defined by fitting a wrapped two-term Gaussian distribution and observing the distance of the two means of each peak. The difference of the peak means for CAT C-1 was narrower than 35° and wider than 70° for CAT C-2. This classification process was applied to all SHG images in the 3D stack. Once the images had a clear tendency towards one type of crimping throughout the whole stack, the entire region was assigned that corresponding type. A polar plot that represents the 3D stack can be generated by adding all the data points from each slice.

In order to look at the effect of helicity in CAT C-2 images, the crimp angle was obtained by measuring the fiber orientation differences of the two neighboring SHG bands. Initially, each bright band was isolated, and then FT-SHG was applied to the isolated images to calculate the orientation. This process was repeated on each band and the corresponding angle was recorded.

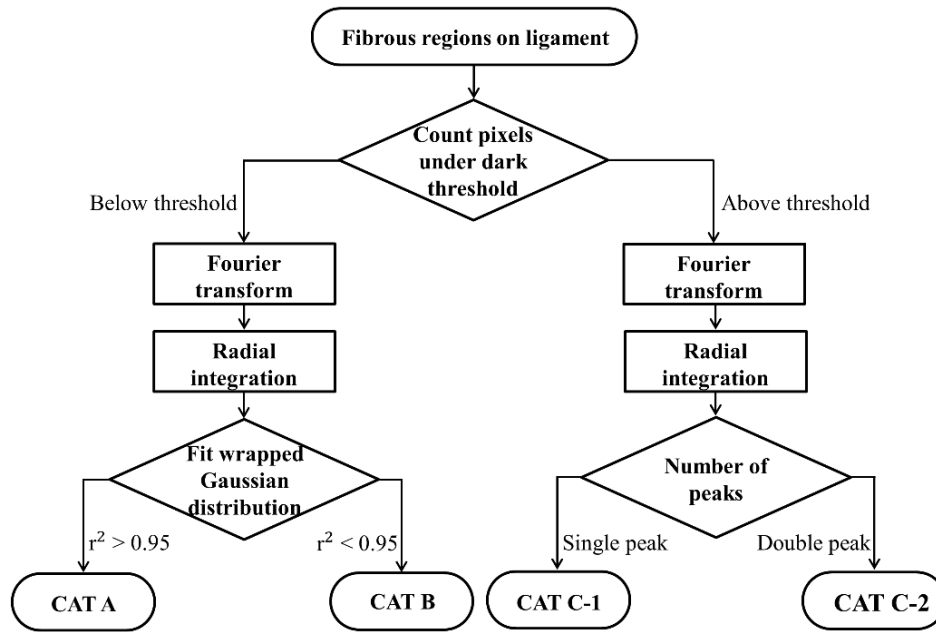


Figure 3.2: Decision process of the image analysis for differentiating each crimp type. Adapted from [23].

3.3 Results and discussion

Based on observation, the SHG images are categorized into CAT A, B, or C, as shown in Fig. 3.3. CAT A is characterized as images with little or no crimps in the fibers. Crimps that are limited to in-plane are defined as CAT B. CAT C is images having crimps that are out-of-plane, along the third spatial dimension. The fibrous features on the SHG images are considered as ‘fibers’ due to the diameter coinciding with previous studies [105] and the probability of each crimp type to be detected in the fibrous regions of PCL is comparable. Conventional sample preparation stages such as dissection and cutting tissue into slices could alter the original, natural fiber structure of ligament. However, we note that structure analysis performed on *ex vivo* condition is a common methodology conducted by many researchers that have been shown to be of value [84,87,94,95,99] and the primary focus of this study is to employ SHG imaging to quantify collagen fiber crimping of ligament under *ex vivo* conditions.

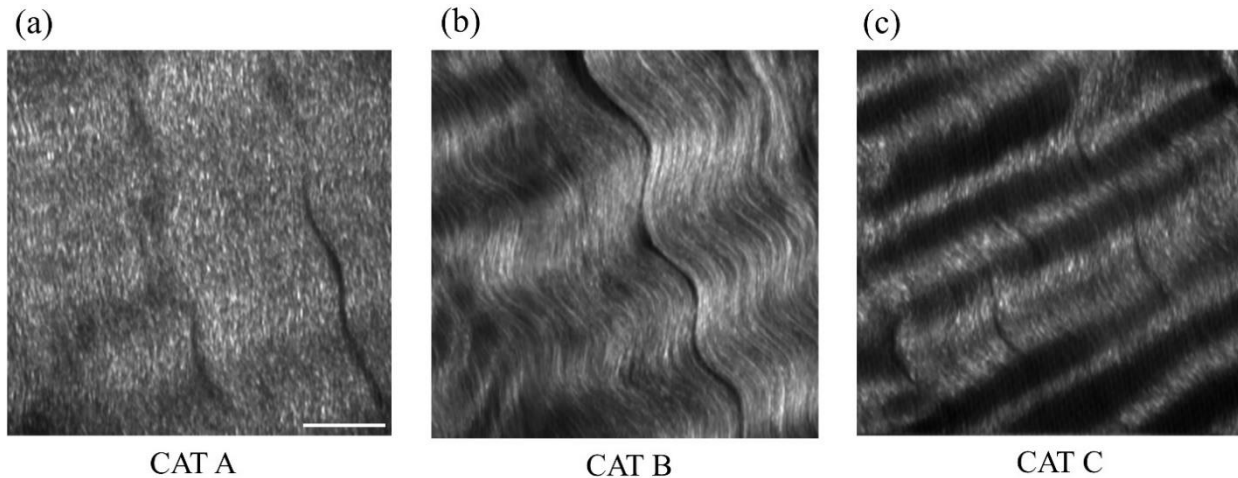


Figure 3.3: Three types of collagen fiber crimping in PCL. (a) CAT A has almost no waviness of fibers, and the majority of them are in a single orientation. (b) CAT B has in-plane crimps broadening the range of possible fiber orientations. (c) CAT C has repeating dark and bright bands orthogonal to the fiber direction, illustrating crimps out-of-plane. Scale bar is 20- μ m and applies to all images. Adapted from [23].

Figure 3.4 summarizes the results of our FT-SHG analysis on representative crimp patterns for CAT A, B, and C. In Fig. 3.4(a) we observe the representative SHG images for each type. We confirm that CAT A visually appears to have little to no crimps, while CAT B has an in-plane crimp pattern. We observe in Fig. 3.4(a) that CAT C images also have crimp patterns, but with significantly more dark (low SHG signal) areas compared to CAT A and B. The dark areas represent the out-of-plane crimps and this is due to the fact that the SHG intensity reduces once the fibers go out of the image plane and the signal drops significantly when the fibers are perpendicular with the image plane [106,107]. For further analysis, CAT C is divided into C-1 and C-2, which is based on irregular and regular crimp patterns, respectively.

The spatial-frequency maps (on a log scale) for the aforementioned crimp patterns are shown in Fig. 3.4(b). The insets highlight the low spatial-frequency components in the center of the spectrum. For CAT A and CAT B, the preferred fiber orientations observed in Fig. 3.4(a) images are readily picked up in the spectral data. In CAT C-1, we observe more spatial isotropy regarding

collagen fiber preferred orientation and crimp direction. On the other hand, the spatial-frequency patterns for CAT C-2 reveal the preferred orientation of the collagen fibers (similar to the cases of CAT A and CAT B) as well as the approximately orthogonal dark bands observed in the CAT C-2 SHG image. The low spatial-frequency components in CAT C-2 are due to the dark bands.

Figure 3.4(c) displays the radial integration polar plots, which are the sum of the radial integration (obtained from the spatial-frequency data) from each 2D slice within the volume of images per crimp category. Note that the actual summed intensities values for the stack are not shown in Fig. 3.4(c). The straight fibers in CAT A are characteristic of a single orientation which corresponds to a wrapped Gaussian distribution [103,104] in the polar plot (red curve) with $r^2 > 0.95$. Most of the fibers in CAT A are oriented along $\sim 95^\circ$ [observed in Fig. 3.4(a)] as confirmed by the peak of the corresponding plot in Fig. 3.4(c) being marginally over 90° . On the contrary, fibers in CAT B are curled in-plane. In this case, the in-plane crimping add neighboring angles to the primary fiber orientation and result in a broader peak in the polar plot. As a result, the radial integration distribution regarding CAT B deviates from a wrapped Gaussian distribution and has a lower correlation coefficient with $r^2 < 0.95$. In CAT C, the circular plot from 0° to 180° has two peaks for CAT C-2. One of the peaks represents the orientation of the fibers in the CAT C-2 SHG image, which is along $\sim 110^\circ$ angle. The other peak corresponds to the direction of the regular out-of-plane crimp pattern and appears almost orthogonal from the fiber orientation. The distance between the peaks is calculated by fitting a wrapped two-term Gaussian distribution and measuring the difference between the means of each term. In terms of CAT C-1, the out-of-plane crimps are not clear enough to appear as a peak on the circular plot so there is usually a broad single peak. The irregularity of the dark bands in CAT C-1 could be because of the disorder of the crimps [94,108] and an oblique cut from a regular crimp pattern.

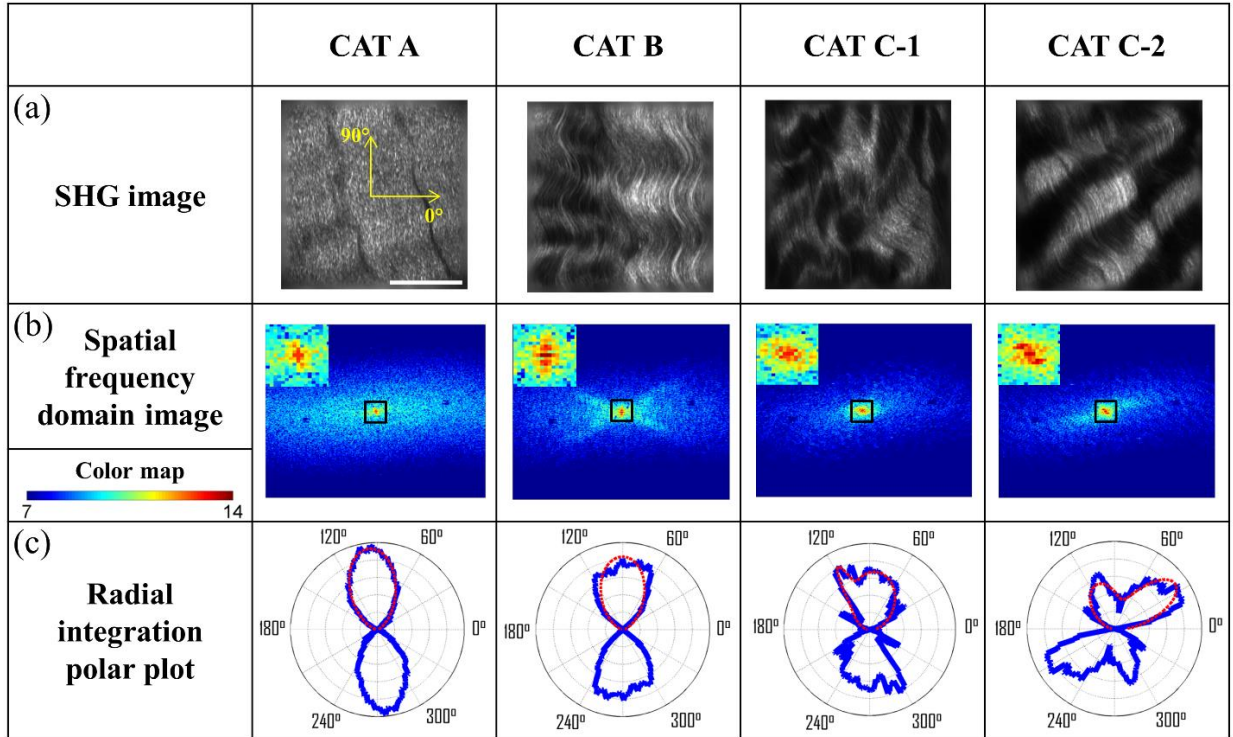


Figure 3.4: Representative (a) SHG images and the corresponding (b) FT images for each crimp type (CAT A, B, C-1, C-2). The insets in the upper left represent a magnified view of low spatial-frequency components (center pixels in the black box). These images are integrated radially across different angles and (c) the resulting integrated values (blue) are plotted in a polar plot format. CAT A and B are fitted with a wrapped Gaussian distribution (red), and the correlation coefficient is calculated. CAT C-1 and C-2 are fitted with a two-term wrapped Gaussian distribution (red), and the number of peaks is detected by measuring the distance between the means of the two peaks. For visualization purposes, the FT images are converted to log scale. The scale bar is 40- μm . Adapted from [23].

The samples are also imaged by other linear imaging techniques such as bright-field [Fig. 3.5(a)] and PL microscopy [Fig. 3.5(b)]. The low contrast in Fig. 3.5(a) results from the unstained biological samples having inherently little contrast [109]. These instruments are used for the purpose of mapping and selecting areas for subsequent SHG imaging and are described elsewhere [61] in more detail. Due to the large tissue size (1.2 \times 1.2 cm), approximately 450 images are stitched to generate images with larger fields-of-view. We choose three fibrous regions per sample on the bright-field image and collect SHG images on the selected regions. As shown in Fig. 3.5(c),

SHG images illustrate the collagen fiber structure variation along the depth (z -plane) and the corresponding assigned type. This structure variation also differs by region. For example, in Fig. 3.5(d) region 2 has irregular out-of-plane crimps on slice 1 (CAT C-1) but 12.5- μm below the plane the pattern appears to be more organized and is categorized as type CAT C-2. 25- μm below slice one the out-of-plane crimps disappear, and the plane is classified as CAT B. Other regions have less feature variance and the assigned type does not change along the z -axis.

It is important to note that the optical sectioning capability of SHG imaging [2,21,110] allows us to capture the overall 3D structural variations in ligament. SHG imaging can also be applied to thick samples by collecting the back-scattered SHG signal [58,111]. There have been studies using PL microscopy quantifying crimp organization by measuring the linear birefringence [112], however low axial resolution diminishes its ability to observe the 3D structural variation. This study focuses on the aforementioned advantages of SHG microscopy, which is suitable for revealing collagen fiber structural information.

Figure 3.6 shows a comparison of ligament SHG images in comparison to bright-field and PL microscope images on each region. We note that the relative image locations are not identical because of the use of different imaging platforms. However, the regions are chosen where clear image fiducials are present, which facilitates co-registration. As a result, each region taken by one of the image modalities could be off by less than 150- μm . Bright-field images normally show fibrous areas while PL images are all showing out-of-plane crimps (CAT C). For the SHG images, a single image per region from the stack was chosen, and the image features vary by region.

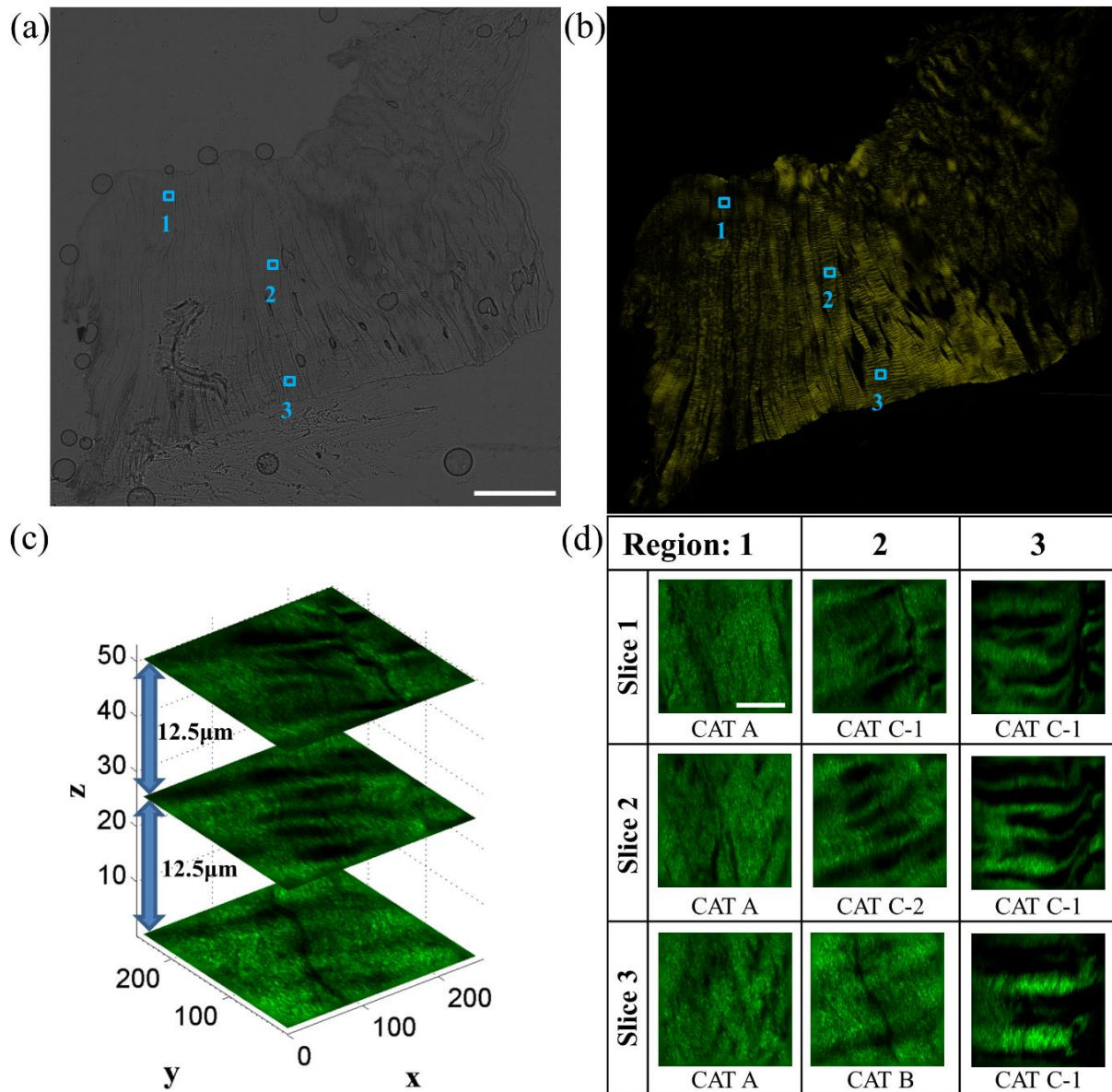


Figure 3.5: Images of the entire ligament sample using (a) bright-field and (b) PL microscopy. Selected fibrous regions on each sample are imaged with SHG in 3D stacks with the step size of 500-nm. There is (c) a structure variation along the z-axis shown by SHG images. All slices in each stack are distinguished by the flow chart shown in Fig. 3.2 and (d) assigned a crimp type. Scale bar is 2-mm and 40-μm, respectively. Adapted from [23].

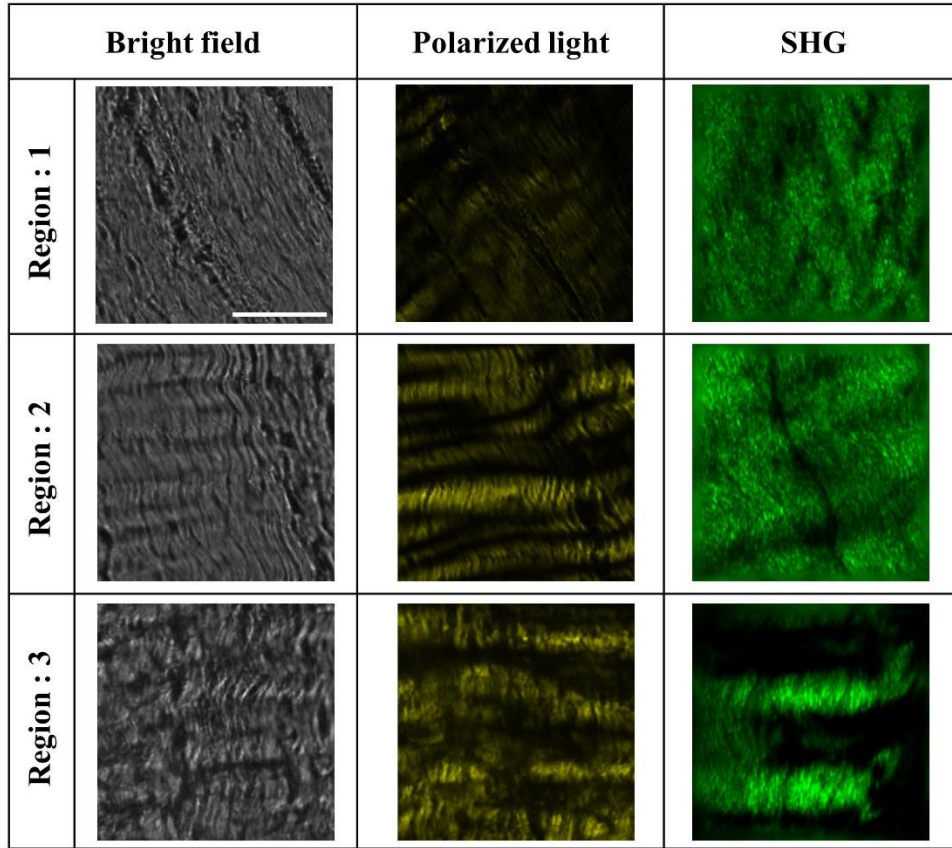


Figure 3.6: Comparison of different imaging modalities on the selected fibrous regions in PCL. For the SHG images, a single image is selected as a representative from the entire 3D stack. The scale bar is 40 μm . Adapted from [23].

In the CAT C-2 images, we observe a repetitive pattern of alternating fiber orientations [Fig. 3.7(a)-(b)]. Specifically, the fiber bands in the SHG images have a similar orientation in every other band. For example, in Fig. 3.7(a)-(b), the first green arrow from the top along with the third and fifth arrows are pointing to comparable directions. This also applies to the second, fourth, and sixth arrows. This trend suggests that the fibers are not only out-of-plane crimped but are also in a helical crimp pattern [Fig. 3.7(c)]. This is because helical crimps naturally have an out-of-plane region once the fibers twist and change directions. The direction shift is repetitive, which leads to dark bands and bright bands alternating orientation for CAT C-2 crimps. We indicate these dark

and bright regions as blue and yellow boxes, respectively, in Fig. 3.7(a)-(b). Since the low-SHG-signal areas are relatively large, it can be thought that the twist areas have a planar crimp that makes the out-of-plane area extended. We utilize a solder wire to replicate the crimp pattern in Fig. 3.7(c). Fig. 3.7(c) also illustrates each individual crimped fiber aligned next to each other forming bundles. These bundles of fibers are stacked in layers maintaining its structure. In the SHG images, this is shown as no particular change in the crimp pattern throughout the z -stack. The observed features in CAT C-2 such as the bright and dark areas and fiber directions remained constant even though the depth of focus changes for roughly 20- μm .

The crimp angle is defined as the angle of the crimp with respect to the horizontal axis [Fig. 3.7(d)], and thus intuitively crimp angle in our case is equivalent to one half of the angle differences between each band. The measured crimp angle ($10^\circ\sim 20^\circ$) falls into the range with previously published data [95,113,114].

A direct comparison was conducted on CAT C-2 SHG images using low (0.65) versus high (1.4) NA objective lens. Low NA SHG images have a bigger intensity difference between bright and dark bands than the high NA images, as shown in Fig. 3.8. This is because high NA objective lens focuses the laser more inclined, resulting in stronger z -axis components illuminating the sample. Thus, the fibers along the z -axis emit a stronger signal compared to the low NA images. This result agrees with our hypothesis stating CAT C-2 is a helical structure, since the helical structure naturally has an out-of-plane region once the fibers twist.

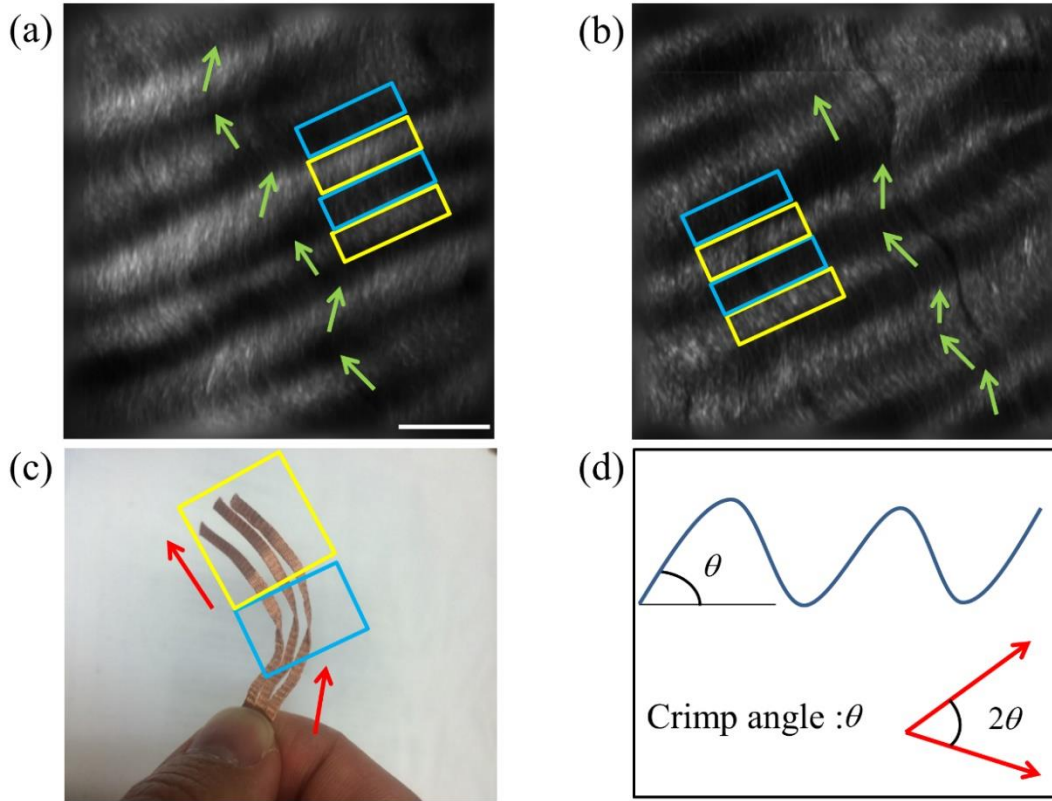


Figure 3.7: Helical crimp pattern in CAT C-2. In (a)-(b) CAT C-2 images, fiber orientation shifts in a repetitive pattern. Fibers have a similar orientation in every other bright band. Regions in the yellow rectangle have a high SHG intensity indicating the fibers are parallel with the image plane. Regions in the blue rectangle have a low intensity suggesting that the fibers are oblique or perpendicular with the image plane. (c) Solder wires are used to describe the helical crimp pattern with an out-of-plane crimp. (d) Schematic demonstrating how the crimp angle is calculated. The scale bar is 20- μm . Adapted from [23].

Previous studies conducted using electron microscopy [91–93] and PL microscopy [89,112,116] also identify the helical crimp patterns of collagen fibers. Electron microscopes revealed the twisted fibers directly from highly magnified images, and PL microscopy showed the helicity of fibers by measuring densitometric features from the birefringence intensity. From the helical structure, researchers have suggested they act like a buffer system absorbing load to prevent damage that could occur in fibers during elongation [95]. The helical structure has also been applied to simulation models [113] and analyzed for applications such as grafts [92,93]. Our results

from SHG microscopy brings another modality for imaging the helicity of ligament fibers and demonstrates the potential to provide quantitative image data for 3D computational simulations of fiber-based anisotropic materials.

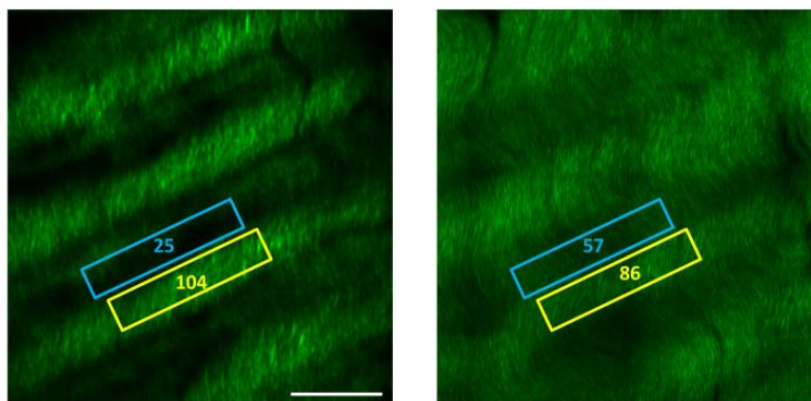


Figure 3.8: Comparison of CAT C-2 region with low versus high *NA* objective lens. Scale bar is 25 μm . Adapted from [115].

3.4 Conclusion

In conclusion, 2D FT-SHG was applied for the first time on PCL to quantitatively assess collagen fiber crimp patterns. The results of our work could be summarized in three major points: First, we were able to identify three types of crimping patterns (CAT A, B, and C) in PCL samples. Along with FT analysis, a customized code was used to distinguish each type quantitatively. Second, we demonstrated the 3D variation of crimp structure using SHG imaging by applying the 2D image analysis on each image along the 3D stack. Third, we verified the helical crimp pattern of collagen fibers in ligament previously revealed by electron and PL microscopes. Our work takes advantage of the label-free, high-contrast, and optical sectioning capabilities of SHG microscopy and could potentially be used to link the fibrous structural information in PCL with its underlying mechanical properties.

CHAPTER 4. ASSESSMENT OF ELECTRON-BEAM IRRADIATION ON COLLAGENOUS TISSUES USING QUANTITATIVE SECOND-HARMONIC GENERATION IMAGING

4.1 Introduction

In scanning electron microscopy (SEM) a raster-scanned e-beam irradiates the sample and the resulting secondary and backscattered electrons are detected to form an image of the sample with nanometer resolution [117,118]. The high spatial resolution and fast imaging speed (~1000 megapixels per second) have been applied to a broad range of applications from material science to biology [117] to obtain the structural information and precise measurements of the sample in nanometer scale. However, the sample needs to be placed in a vacuum chamber in order to prevent air molecules from scattering the electrons reaching the sample. Thus, the standard procedure for SEM sample preparation usually involves initial dehydration followed by coating with an electrically conductive material, which makes it challenging to image biological samples in their natural state.

To mitigate this issue, the ESEM was invented to allow gas inside the sample chamber by using multiple pressure-limiting apertures, while permitting the e-beam to remain under high vacuum [119,120]. Images are formed by collecting cascaded secondary electrons which are electrons formed by the collision of secondary electrons ejected by the sample with gas molecules resulting in ionization. The sample chamber pressure and temperature are both adjustable, which result in a desired chamber humidity, thereby prohibiting sample drying. Also, the positive ions resulted from the gas ionization process reduce the charging effect, which usually occurs on non-conductive samples. Thus, ESEM becomes suitable for imaging fully hydrated and uncoated biological

This work was previously published in W. Lee and K. C. Toussaint, Jr. [24], and is adapted here with permission

samples, and multiple ESEM studies have reported on the morphological features of mammalian cells [121], bone [122], retina [123] and embryo [120]. ESEM imaging has also been applied to classify different cell, and tissue types in histological paraffin sections of rat tongue, and the results agreed with light microscopy analysis [124]. In addition, ESEM imaging has been able to evaluate microstructural damage on potato tubers while researchers have suggested the least destructive sample preparation method [125].

In general, researchers have found that ESEM produces less e-beam induced sample shrinkage and cracking, compared to SEM [121]. Some early attempts to understand the effects of the ESEM on biological function observed the continued plant growth [126] and movement of ants [119] after e-beam exposure. Other studies have assessed the morphological changes in specimens caused by ESEM imaging. In one example, the mean volume of yeast cells was shown to shrink from oval-shaped to a flattened pattern [121]. In another case, e-beam exposure melted down the wax surface layer in plants [127]. Notwithstanding the significance of these studies, damage assessment from ESEM has been mostly qualitative, with little work being done at all on the effect of e-beam exposure on biological tissues such as collagen.

In this chapter, we apply quantitative SHG microscopy to investigate the effects of ESEM on collagen fibers, which undergo various sample preparation conditions. Quantitative SHG imaging is used as a tool to compare nearly identical areas before and after e-beam exposure from an ESEM. Selected 2D quantitative parameters are extracted from the SHG images, which reveal the changes in unstained porcine tendon structure caused by ESEM, namely, fiber shrinkage, enhanced cross-linking, and structural damage. We also demonstrate that the higher spatial resolution afforded by ESEM, compared to SHG imaging, permits visualization of fine structural details, but the relatively lower collagen specificity makes it difficult to quantify collagen fiber orientation.

4.2 Methods

4.2.1 Sample preparation

Porcine feet were purchased from a local abattoir and stored in the freezer (-20°C). Subsequently, deep digital flexor tendon tissue was dissected after the samples being thawed overnight.

For fresh samples, tendon was embedded in optimal cutting temperature compound and cut into 25- μm thick slices by a cryostat (CM3050, Leica). Slices were mounted on glass slides and were frozen or treated by three different levels of drying procedures. Frozen samples were stored in the freezer and taken out before imaging. Air-dried samples were left dried in air for at least 24 hours. Dehydrated samples were damped in four incremental levels of ethanol (37%, 67%, 95%, 100% - three times) for 10 minutes each. Critical-point dried samples went through the aforementioned dehydration process before critical-point drying (Samdri-PTV-3D, Tousimis) and lastly were embedded in paraffin wax and cut by a microtome (CM3050, Leica) instead of a cryostat.

To fix samples, we placed the dissected tendon samples in paraformaldehyde for one hour in vacuum condition. Air-dried samples followed the same protocol as the fresh samples. The other fixed samples (dehydrated, critical-point dried) were conducted as explained previously and embedded in paraffin wax as the final step.

Wet samples remained fresh, without going through any fixation or drying process. To cut thin sections, the wet samples were embedded in optimal cutting temperature compound. All wet samples slices were cut to a 4 \times 4-mm dimension in order to fit on a custom made 6 \times 6-mm glass substrate. To prevent dehydration and decomposition, the samples were kept in a petri dish hydrated by placing buffer solution droplets on the sample and stored in a refrigerator until imaging.

4.2.2 SHG imaging

A tunable Ti:Sapphire laser (Mai Tai, Spectra-Physics) generating 100-fs duration pulses centered at 780-nm wavelength illuminates the sample. The 10-mW power beam was then focused on the sample by a 40X, 0.65 NA objective lens (PLAN N, Olympus) and the backward SHG coming from the sample was collected by a 390-nm bandpass filter (FF01-390/18-25, Semrock). Wet samples were placed on top of a standard microscope slide (25 × 75 mm) in order to be secured fixed on the microscope stage. On each sample, a targeted fibrous area with clear fiducials such as edges and wide gaps between fiber bundles was chosen for co-registering the SHG microscopy to ESEM. A motorized stage (max5000, Ludl) provided 100 nm resolution translational adjustments of the sample on the stage. All samples but the wet were imaged in 3D stacks of dimension 100 × 100 × 15 μm where the step size along the z-axis is 500 nm.

4.2.3 ESEM imaging

Fresh and fixed samples were imaged with the low-vacuum mode ESEM (Quanta FEG 450 ESEM, FEI) by attaching the microscope slide directly on the stud. We adjusted the pressure inside the chamber to be 0.98 Torr and the accelerating voltage to 5 kV. The distance between the sample and e-beam, working distance, was 9 mm. Initially, we used low magnification to identify the targeted area and further increased up to 1600X on the targeted area. For each ESEM image, the pixel dwell time was 10 μs; to assure the entire targeted area is exposed to the e-beam, we also probed the surrounding area, which took roughly 15 minutes in total. For wet-mode ESEM, we used double-sided black tape on the 6 × 6-mm glass to not only enhance the contrast but also mount the sample on the stud being placed on the Peltier stage. The target temperature was 4°C and the pressure was 6.1 Torr, which was selected to generate 100% humidity inside the chamber. A

(gaseous) secondary electron detector was implemented to generate the image. We used the identical settings for the magnification and working distance with the low-vacuum mode. Due to the low contrast caused by the water molecules inside the chamber, we increased the accelerating voltage to 20 kV.

4.3 Results and discussion

4.3.1 SHG imaging acquisition and parameter measurements

Near identical areas of porcine tendon, sample are imaged using SHG microscopy before and after ESEM imaging (low-vacuum and wet mode) by using clear fiducials such as a corner or edge of fiber bundles to find the similar regions. Wet-mode ESEM maintains the relative humidity up to 100% in the chamber, thereby preventing evaporation from occurring during imaging. Low-vacuum mode is intermediate between conventional SEM and wet mode where it does not require any metal coating on the sample and allows air inside the chamber at a pressure up to 1.0 Torr while imaging. The settings used on the ESEM are referenced from literature [120,121,123,124] and not aimed to destroy the sample deliberately. We also prepare the SHG image pair (before and after e-beam exposure) without any ESEM imaging for reference, and the sample is left undisturbed for approximately the same amount of time as the experiments carried out with ESEM imaging. In addition, to analyze the effects of different sample preparation methods, fresh and fixed samples are arranged and preserved either frozen or in different stages of dehydration, which includes air-dried, ethanol dehydrated, and critical-point dried. These samples are all imaged under low-vacuum mode, while wet samples without any treatment are imaged for wet-mode ESEM. Due to the optical sectioning capabilities of SHG microscopy, all SHG images are obtained in 3D stacks. Details of the experiment are listed in Section 4.2 Methods. The before and after SHG

images are compared by measuring selected quantitative parameters including density I_d , peak spectral intensity I_s , and ratio r by a customized MATLAB code. The amount of parameter change between the SHG image pairs is represented as mean \pm standard deviation. Groups are compared with the unpaired two-tailed Student's t-test for small sample sizes [128], and the significant p value is 0.05.

A representative SHG image 3D stack is shown in Fig. 4.1(a), with each 2D image in the stack comprising a grid of cells (16×16 pixels) and a field-of-view of $100 \times 100 \mu\text{m}$. In each cell, the area fraction referring to the number of pixels under the noise level divided by the total number of pixels is counted [16]. As a result, each cell will be given an area fraction value ranging from 0 to 1, where 0 indicates the entire cell has no SHG signal and 1 means all the pixels in the cell contains an SHG signal. The selected yellow boxed area is chosen where the majority of fibers are in a uniform orientation, and there are less dark areas. The color map in Fig. 4.1(b) illustrates each area fraction value, and the average value from the entire 2D-SHG image represents the parameter defined as density I_d of the image. The other two parameters, peak spectral intensity I_s and ratio r [129,130], are obtained in the spatial-frequency domain by applying FT on the selected region [Fig. 4.1(c)]. Radial amplitude strength versus angle is plotted [Fig. 4.1(d)] by radially integrating the intensity profile from 0° to 180° along each angle and the maximum value is defined as peak spectral intensity I_s . On the spatial-frequency domain image [Fig. 4.1(c)], we remove low-intensity pixels before intensity normalization and conversion to a binary image [Fig. 4.1(e)]. This image is fitted to an ellipse, and the ratio r is calculated, which is the length of the long axis α to the short axis β . All three parameters are measured throughout a z -stack, and the average value is acquired.

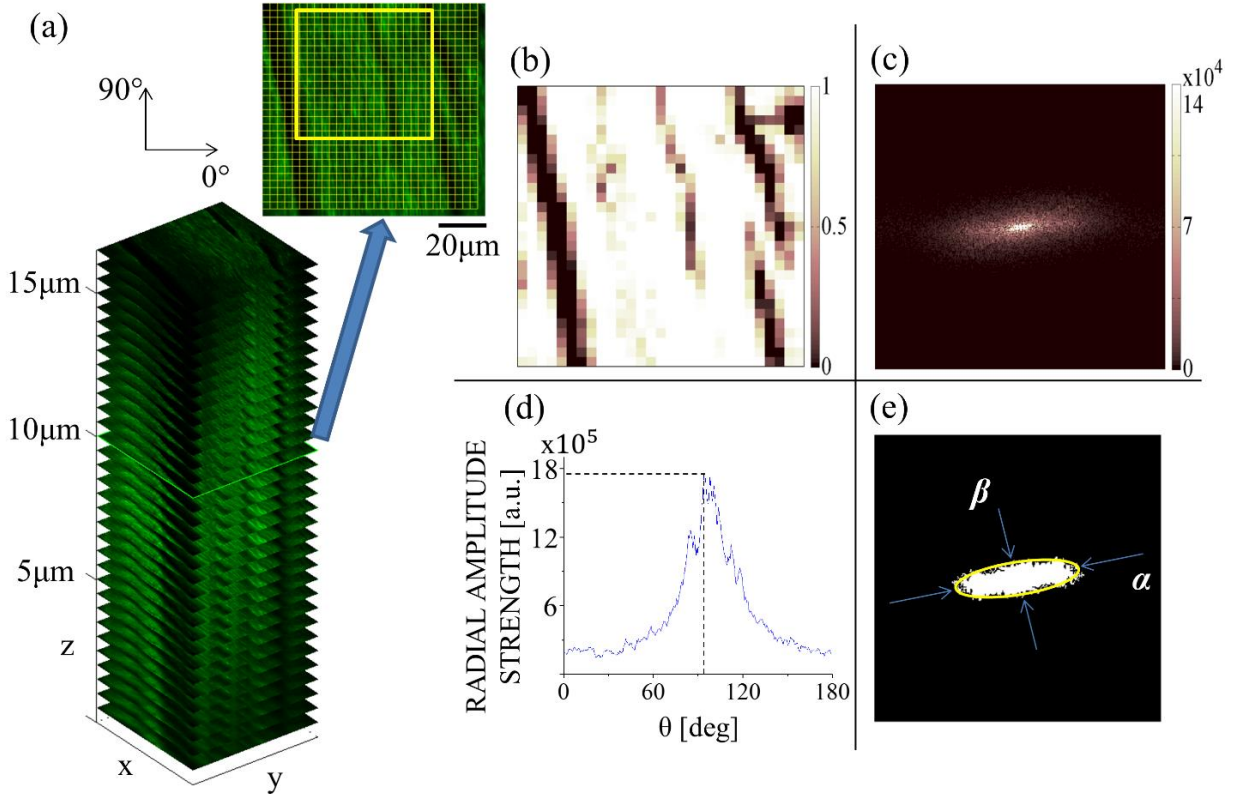


Figure 4.1: Process of extracting quantitative information from 2D-SHG images. (a) The obtained 3D-SHG stack and a 2D image ($100 \times 100 \mu\text{m}$) from a single plane. The yellow box indicates the selected region where peak spectral intensity I_s and ratio r is calculated. On the grid, a cell (16×16 pixels) shows the scale where the SHG area fraction is calculated. (b) A color map of the SHG area fraction of each cell. (c) The spatial-frequency domain image (magnitude spectrum) of the yellow boxed region. (d) The plot of the spatial-frequencies strength versus orientation angle and peak spectral intensity I_s . (e) The binarized Fourier domain and ratio r obtained by measuring the ratio of the long axis α to short axis β . Adapted from [24].

4.3.2 E-beam effects observed in SHG images

Figure 4.2(a)-(c) shows SHG images of the collagen fibers in fresh tendon samples that are frozen [Fig. 4.2(a)], air-dried [Fig. 4.2(b)], and dehydrated [Fig. 4.2(c)] before and after ESEM exposure in low-vacuum mode, as displayed in rows (i) and (ii), respectively. Based on the images taken before ESEM exposure, we observe under the ESEM row of Figs. 4.2(a)-(c) (i) punctate fiber structures, especially in the selected regions of interests shown by the yellow dotted line in each image. These dotted squares are the selected regions chosen for measuring I_s and r . In Figs. 4.2(a)-

(c) (ii), after ESEM exposure, fibers generally appear to have a more continuous fiber structure and higher SHG intensity. The punctuate feature in SHG images suggest to be an indicator of less cross-linked fibers and has previously been observed in immature collagen fibers [45,131] and fibers in late gestation stages [14]. This implies that the e-beam in ESEM potentially promotes cross-linking between collagen fibers. Enhancing cross-linking by e-beam irradiation is a well-understood method in manufacturing to improve the mechanical properties and chemical stability of polymers [132,133]. This cross-linking is generated as the irradiation induces polymer molecules to have an unpaired electron which leads to a covalent bond between free radicals [134,135]. Also, there are studies discussing the induced cross-linking on collagen caused by gamma and e-beam irradiation [136,137]. However, these studies analyze e-beam exposure on different samples, whereas we demonstrate the comparison of collagen fibers before and after the ESEM imaging on identical areas using SHG microscopy. Thus, our approach is the first to our knowledge to directly observe a potential causal relationship between e-beam irradiation and collagen fiber structure. The gaps between the fiber bundles also appear to widen [Figs. 4.2(a) (i), (ii)] due to shrinkage effects [138,139]. Both the induced fiber cross-linking and shrinkage constantly appear throughout the z -stack, thereby indicating that the observed change in collagen fibers is not an artifact of focusing on different planes in the sample. In the SHG image pair without any ESEM imaging, we do not observe any difference between initial SHG images taken ('before') and those taken one day later ('after') as shown on the No ESEM row in Figs. 4.2(iii)-(iv). Thus, the lapse of time, at the scale of a single day, does not play a role on the cross-linking effect.

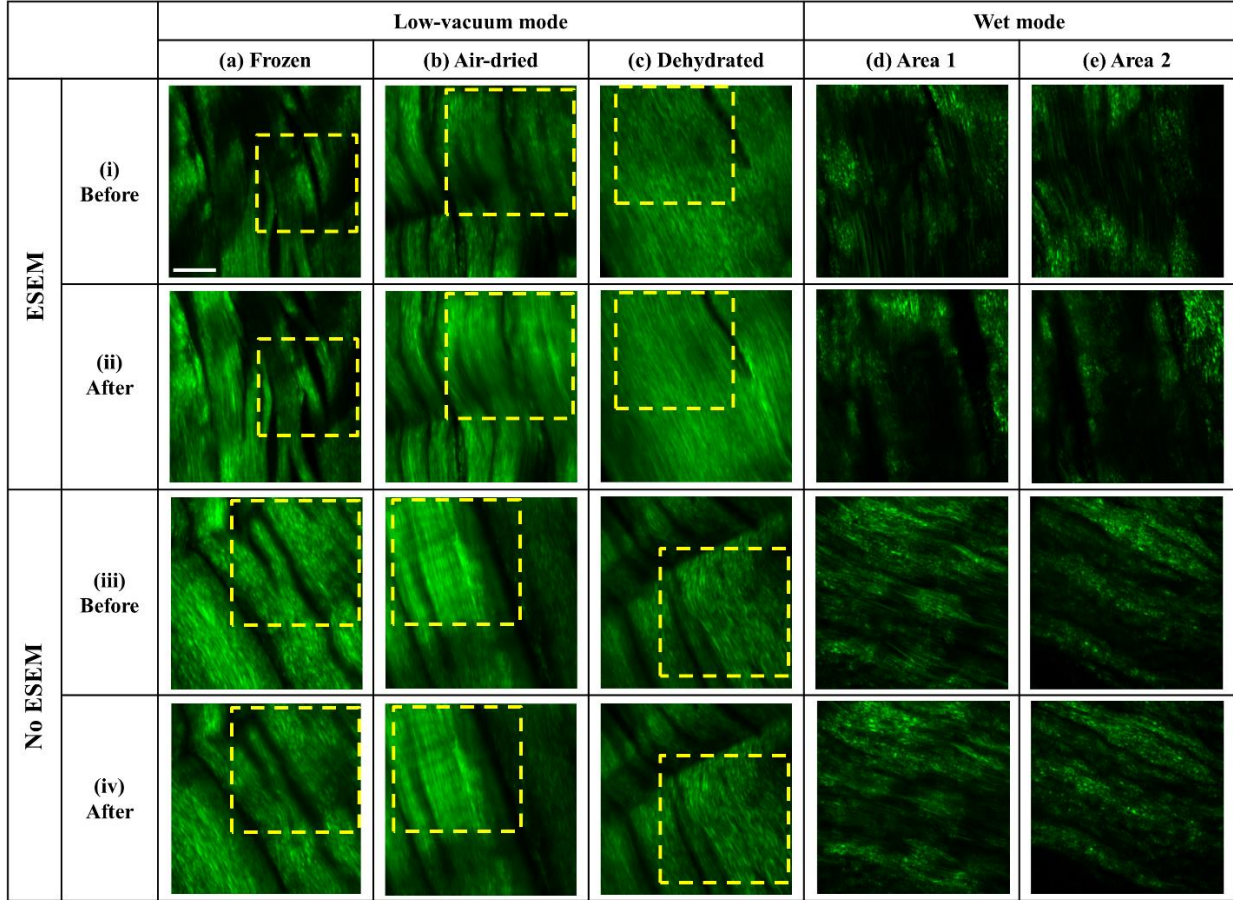


Figure 4.2: Comparison of the SHG images of tendon samples before and after ESEM exposure in low-vacuum and wet mode. (a) Frozen samples. (b) Air-dried samples. (c) Ethanol dehydrated samples. (d), (e) Hydrated samples. For ESEM exposure (i) and (ii) correspond to before and after exposure, respectively. (iii) and (iv) correspond to images taken with the same time interval but without ESEM exposure. All compared images are acquired from the identical spatial region. The yellow dotted line areas are selected regions for measuring I_s and r . Electron voltage for low-vacuum mode and wet mode is 5 kV and 20 kV, respectively. Scale bar is 20 μm and applies to all images. Adapted from [24].

Figure 4.2(d), (e) illustrates the comparison of SHG images of the collagen fibers before and after ESEM exposure in wet mode, as displayed in rows (i) and (ii), respectively. As shown in Figs. 4.2(d), (e) (i) and (ii), the overall structure alters, and more dark areas form. As a result, co-registration of the identical area, imaged before e-beam exposure, becomes extremely difficult. Consequently, we choose a wide fibrous area located close to a clear reference region where there is little to no irradiation of the e-beam and obtain two images [Figs. 4.2(d), (e)] on the selected

fibrous area. This reference region assists with locating the area after ESEM imaging and helps to verify that the SHG images observed after e-beam exposure are taken less than 200 μm apart compared to those taken before ESEM imaging. The reason for the total structural change could be due to the water molecules in the tissue, promoting ionization and chemical breakdown [140,141]. As a result, hydrated samples become more vulnerable to beam irradiation compared to dried samples. For example, researchers have verified the increase of beam damage on hydrated polypropylene [140]. Another reason for the collagen fiber samples being damaged could be the increased accelerating voltage (20 kV) used in wet-mode ESEM to compensate for the low contrast in ESEM imaging. The time interval between the before and after e-beam exposure of SHG images is approximately three hours. Conversely, the SHG image pair obtained with the same time interval, but without ESEM imaging, appears to nearly be identical [Figs. 4.2(d), (e) (iii) and (iv)]. This indicates that the drying occurring in three hours have a negligible effect on any observable collagen structure.

We further analyze the effects of the e-beam exposure by demonstrating the extreme case of e-beam-induced damage on the sample using high voltage and magnification, as shown in Fig. 4.3. Significant differences are observed for both SHG and ESEM images of the same regions taken before and after e-beam exposure, as shown in Figs 4.3(a) and Figs 4.3(b), respectively. The sample is intentionally left exposed under the e-beam for approximately one minute under high voltage (20 kV) and magnification ($> 1600\times$). The pixel dwell time is 10 μs , and the operating ESEM mode is low vacuum. The collagen content decreases, creating craters observed in both the SHG [Figs 4.3(a)] and ESEM images [Figs 4.3(b)]. The surrounding areas also change substantially, namely the gaps between collagen fibers widen and the SHG intensity in these same regions decrease. These results could be potentially attributed to the highly concentrated e-beam

bombardment of the sample, thereby generating bond scission and surface temperature increase [142,143].

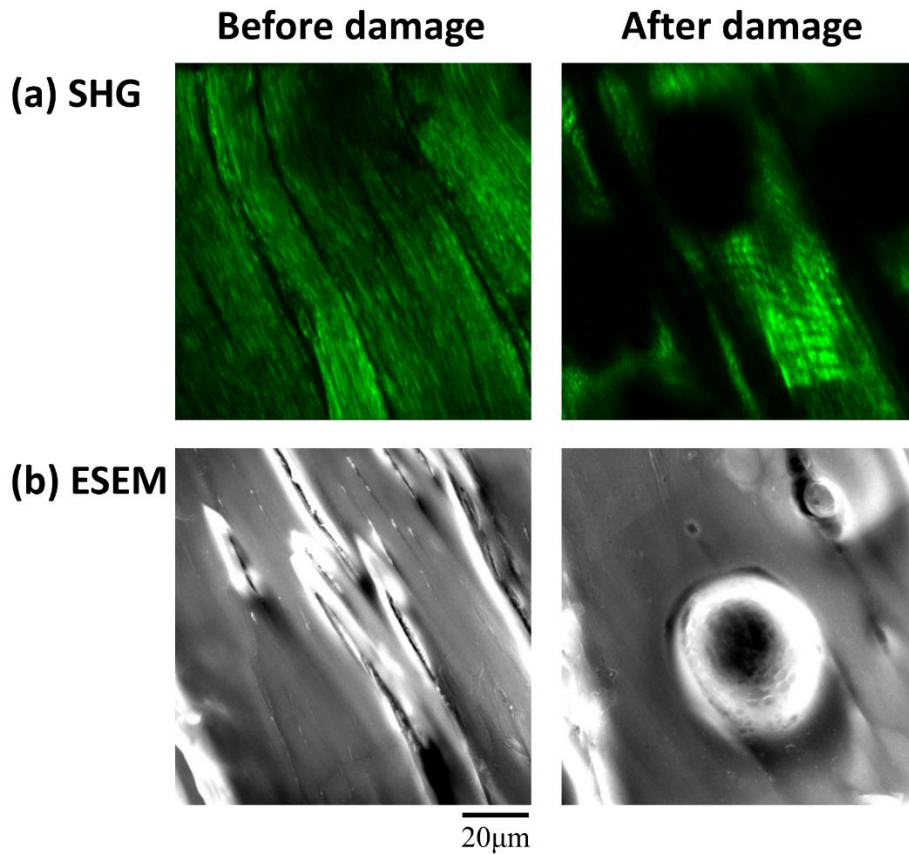


Figure 4.3: Tissue damage induced by the e-beam. (a) SHG images of a fibrous area before and after e-beam exposure. (b) ESEM images before and after e-beam exposure. The setting of the ESEM is 20 kV and 3200X for acceleration voltage and magnification, respectively, and the operating mode is low vacuum. For visualization purposes, the maximum SHG threshold is adjusted. Scale bar applies to all images. Adapted from [24].

4.3.3 Quantitative analysis of e-beam exposure on the SHG images

The parameters explained in Fig. 4.1 (I_d , I_s and r) are measured on the 2D-SHG image pair (before and after e-beam irradiation) and the amount of change in these parameters is plotted in Fig. 4.4.

The calculated parameters on each SHG image are averaged for the entire 3D stack and repeated

on frozen, air-dried and dehydrated samples. For the low-vacuum mode [Fig. 4.4(a)] ESEM group on fresh samples, I_d ($10.14 \pm 5.83\%$), I_s ($17.25 \pm 12.60\%$) and r ($17.41 \pm 5.06\%$) all increase more than 10%, whereas fibers analyzed without ESEM imaging (No ESEM group) have a change smaller than 4% : $-3.01 \pm 1.64\%$ for I_d , $-1.36 \pm 4.57\%$ for I_s and $0.28 \pm 2.30\%$ for r . The difference between the ESEM and No ESEM groups for I_d ($p = 0.020$) and r ($p = 0.006$) are shown to be statistically significant ($p < 0.05$). With respect to I_s a p value slightly greater than 0.05 ($p = 0.074$) was obtained. The reason for the increase in the parameters after ESEM exposure is likely due to the induced cross-linked fibers. Cross-linked fibers have less graininess in SHG images, which results in a stronger intensity along the preferred orientation in the spatial-frequency domain image. This results in a larger peak in the magnitude spectrum [Fig. 4.1(d)] and also increases the length of the major axis and shortens the minor axis in the binarized Fourier domain [Fig. 4.1(e)]. In addition, strongly cross-linked fibers appear to have a higher intensity in the SHG image compared to less cross-linked fibers. To summarize, the induced cross-linking effect is the cause of the change on all three parameters. The density value does not increase as much as the other two parameters because of the fiber shrinkage effect widening of the gaps between fiber bundles. However, we select areas where fibers occupy most of the image and therefore, the density value after e-beam exposure increases. On the other hand, for low-vacuum mode ESEM on fixed samples [Fig. 4.4(b)], the parameters change less than 5% both on the ESEM and No ESEM group indicating tissue fixation provides resistance of e-beam effect. This complies with previous studies conducted on neuronal cells, demonstrating the stability of the fixed samples during ESEM imaging [144].

Figure 4.4(c) shows the change of average-parameter values caused by wet-mode ESEM. The average values are obtained from two broad fibrous areas, each including two SHG images. This

is because, as previously mentioned, the e-beam damage of the sample makes it difficult to locate identical areas, and thus, broad fibrous areas are chosen. All parameters for the fibers that are exposed to the wet-mode ESEM decrease more than 16% ($I_d = -16.49 \pm 4.30\%$, $I_s = -46.65 \pm 15.59\%$, $r = -32.31 \pm 3.18\%$), whereas the No ESEM group parameters ($I_d = -3.36 \pm 6.62\%$, $I_s = 2.15 \pm 9.87\%$, $r = -2.30 \pm 2.07\%$) have minimal change less than 4%. The difference between ESEM and No ESEM groups for all parameters are shown to be statistically significant ($p < 0.05$): $p = 0.032$ for I_d , $p = 0.004$ for I_s and $p = 0.00002$ for r . The decrease of the density is a result of the increasing dark areas, and the other two parameters dropped reflecting the fiber orientation and overall structure becoming more diffuse and irregular in the SHG images. Overall, I_s and r could be used as a measure of the cross-linking occurring in fibers and also to detect damage happening on the sample.

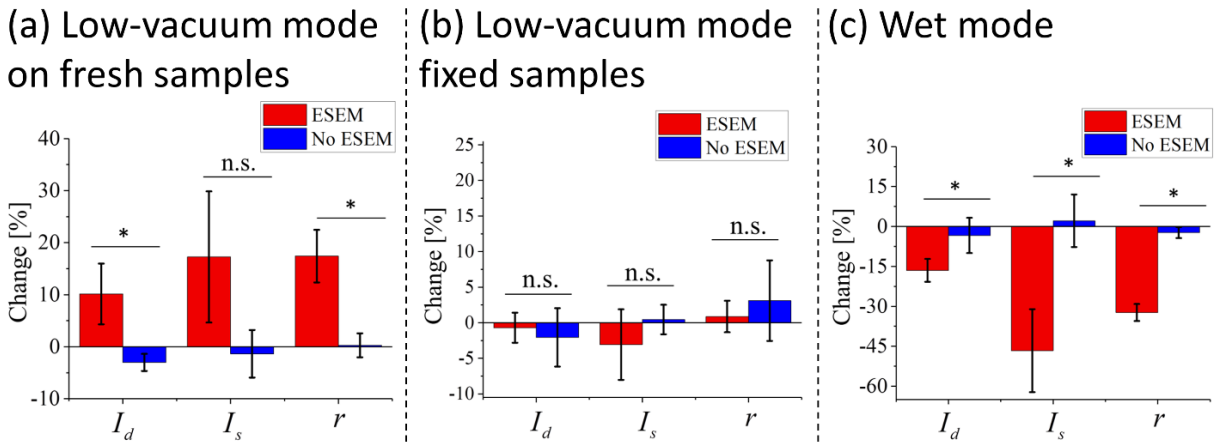


Figure 4.4: Parameter changes measured from SHG images as a function of ESEM mode and sample preparation method. The average changes of the parameters (density I_d , peak spectral intensity I_s and ratio r) resulting from (a) low-vacuum mode ESEM imaging (red; $n=3$) and with no ESEM imaging (blue; $n=3$) on fresh samples. The value is averaged for the frozen, air-dried, and dehydrated samples. Change measured by (b) the low-vacuum mode ESEM imaging (red; $n=3$) and with no ESEM imaging (blue; $n=3$) on fixed samples. Change caused by (c) the wet-mode ESEM imaging (red; $n=3$) and with no ESEM imaging (blue; $n=4$). The data shown are mean \pm standard deviation; n.s., not significant; $*p < 0.05$. Adapted from [24].

4.3.4 Advantages and limitations of ESEM on collagen fiber imaging

Figure 4.5 shows the result of preferred fiber orientation analysis using the image gradient method [22,145] applied on SHG and ESEM collagen fibers images. This analysis categorizes the predetermined gridded regions into anisotropic, isotropic, and dark regions and computes the preferred fiber orientation on the anisotropic regions. Representative SHG and ESEM images are shown in Fig. 4.5(a) and (b), respectively, and the associated fiber orientation results are in Fig. 4.5(c) and (d). For the SHG image, 98 cells are detected as anisotropic, and the measured preferred orientations match well with the actual fiber orientation. Two cells in the grid are identified as dark regions due to the low intensity. For the ESEM image, only eight cells in the grid are determined as anisotropic, while the remaining cells are considered isotropic and thus have no preferred orientation results. This demonstrates that the intrinsic specificity to fibrillar collagen afforded by SHG microscopy makes it a more suitable tool for quantifying individual fiber orientation in comparison to ESEM, where the spatial resolution is higher but with little specificity to collagen [5].

In spite of the fiber structure alteration and damage generated by the e-beam, there are unique features which highlight the advantages of ESEM, as shown in Fig. 4.5. The identified green boxed areas in Fig. 4.5(a) and (b) represent components on the sample surface, which are the remaining optimal cutting temperature compound used for embedding the sample, and tangled fibers on top of straight fibers, respectively. ESEM also becomes useful for observing features on the nanometer scale within the sample [146]. Figure 4.5(c) and (d) are images of interfascicular connective tissue [147], which are open spaces between collagen fiber bundles. Interfascicular connective tissues are composed of fibroblasts, and numerous blood tissues and studies have investigated age-related alterations in the interfascicular matrix [148] and their correlation with mechanical properties

[149] and muscle atrophy [150] in tendon. Overall, the aforementioned features are challenging to image using an SHG microscope due to the lower resolution and strong collagen type I specificity.

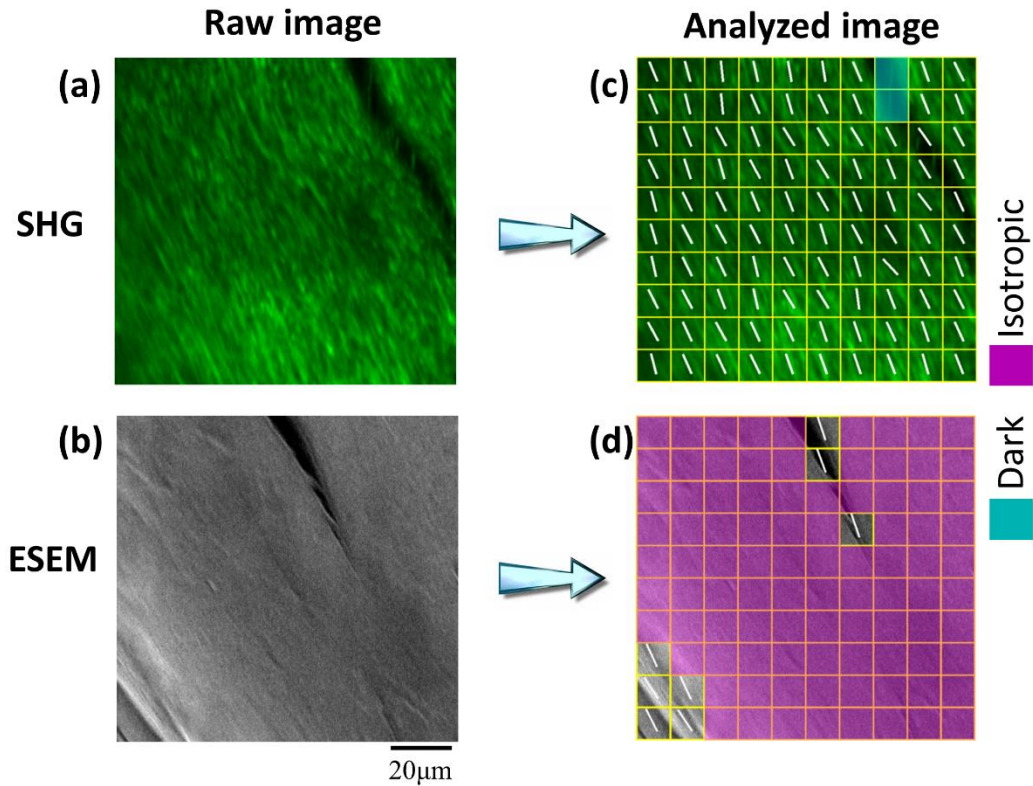


Figure 4.5: Comparison of the computed preferred collagen fiber orientation applied to SHG and ESEM images. Representative (a) SHG and (b) ESEM images of collagen fibers, and (c), (d) their respective calculated fiber orientations. Cyan highlights regions with little or no SHG signal, while purple highlights regions with spatially isotropic orientation of fibers. Refer to reference [22,145] for details. Scale bar applies to all images. Adapted from [24].

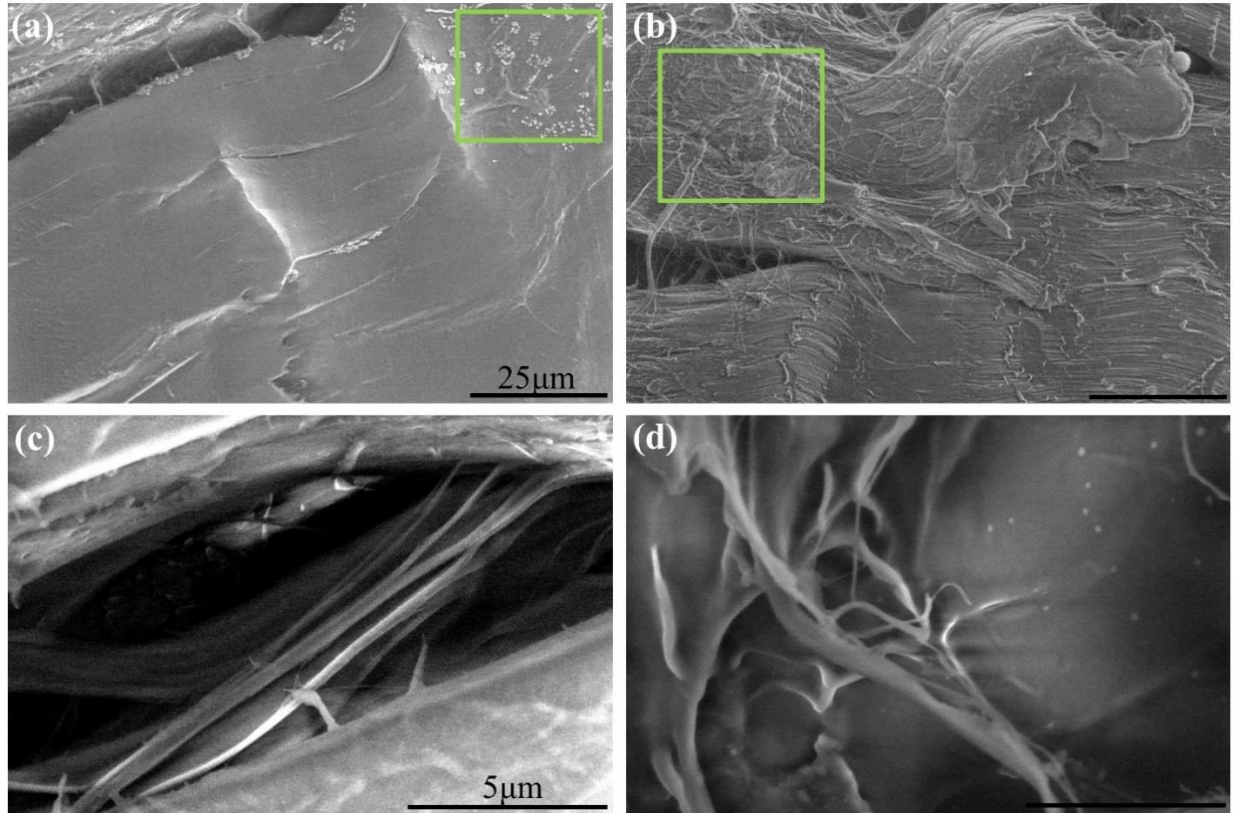


Figure 4.6: Fine features on collagen fiber samples observed in ESEM imaging. The green box illustrates (a) the remaining optimal cutting temperature compound and (b) tangled fibers on top of straight fibers. Scale bar is 25 μm for both images. (c), (d) Interfascicular connective tissue. Scale bar is 5 μm for both images. Adapted from [24].

4.4 Conclusion

In this chapter, the effects of ESEM imaging on collagen fibers were analyzed using quantitative 2D-SHG microscopy. We demonstrated that for frozen, air-dried and dehydrated samples, the e-beam for low-vacuum ESEM imaging promotes cross-linking between fibers, while fixed samples remain unaffected. The analysis was applied throughout the 3D stack showing consistent results. For wet samples imaged by wet-mode ESEM, we observed structure degradation. The change of structure was quantified by measuring parameters derived from the average 2D-SHG image intensity and corresponding spatial-frequency analysis. We observed that these parameters increased in low-vacuum mode and decreased in wet mode after ESEM imaging. Furthermore, we

confirmed that while ESEM provides higher spatial resolution than optical microscopy methods, the specificity to collagen fibers is relatively low. The aforementioned results suggest that to further extend ESEM to *in vitro* applications, thoroughly analyzing its effects on the sample will be critical, notwithstanding the advantages of ESEM such as the ability to analyze the non-collagenous regions of tissues with nanometer resolution.

CHAPTER 5. QUANTITATIVE CLASSIFICATION OF 3D COLLAGEN FIBER ORGANIZATION

5.1 Introduction

There are a handful of optical imaging techniques that are well-suited to non-invasively image fibrillar collagen structures. PL microscopy has been successful in providing 2D high-contrast images of these structures, where the intrinsic birefringence of collagen provides an endogenous contrast mechanism when viewed between two cross polarizers. This imaging technique helped to evaluate the molecular organization and alignment of collagen fibers in different anatomical regions and age in ligament and tendon [151–154]. While PL microscopy does not provide 3D imaging capabilities, polarization sensitive optical-coherence tomography (PS-OCT), a polarization-sensitive, interferometric approach based on the coherence-gating effect [155], has been routinely applied to image collagenous tissues in three-dimensions [156–160]. Specifically, PS-OCT has been used to obtain morphological information of human skin [159,160] and to facilitate detection of diseases including occlusal lesions [156], macular degeneration [157], and glaucoma [158]. SHG microscopy is another common technique used for imaging collagen fibers. Unlike PL microscopy and PS-OCT, SHG microscopy can generate sub-micrometer 3D images of collagen fibers non-invasively. By using these advantages, researchers have implemented quantitative SHG imaging to examine the spatial organization of collagen fibers [21–23,161,162], which is particularly useful for imaging spatially heterogeneous 3D tissues such as uterine cervix [22,162].

Various studies show that analyzing collagen organization in 3D is more effective than 2D analysis alone [163–165]. For example, researchers have shown that characterizing pathological changes caused by fibrosis progression through SHG density and qualitative features over all the

images in the 3D stack resulted in more accurate results compared to 2D analysis [163,164]. In another study, 3D collagen fiber data were found useful to detect malignancy qualitatively in ovarian tissue [165]. On top of these studies, researchers were able to develop methods to extract quantitative information directly from the 3D-image data. Liu *et al.* introduced the 3D orientation variance as a parameter to characterize articular cartilage and differentiate cancer breast tissue from normal tissue [161,166]. In addition, Lilledahl *et al.* measured 3D morphological features of collagen in cartilage for generalized biomechanical models [167]. Such models aim to predict the tissue mechanical behavior based on the structural arrangement of collagen and give the insight to understand collagen structure-function relationship [168–170]. In spite of these approaches using 3D analysis, to the best of our knowledge, no published methodology quantitatively assesses and classifies the 3D collagen fiber organization data from natural tissue structures intuitively, i.e., in a manner that is consistent with direct visualization of fiber organization. Quantitatively classified 3D collagen organizations from collagen-fiber images could enhance the accuracy of biomechanical models. Also, studies demonstrated that the mechanical properties of ECM, which exhibits a complex 3D architecture, has an effect on cellular activities [171,172] and this implies proper mechanical property estimations could aid diagnosing physical injuries and disease [19,173–176].

In this chapter, we demonstrate an algorithm that quantitatively and intuitively analyzes several tissue archetypes based on differing arrangements of 3D collagen fiber organization. Herein, we define five classifications of 3D collagen fiber organizations, namely, uniform, crimped, random, two-fiber family (TFF), and helical, based on their significance to tissue mechanical properties [19,66,85,93,106,168,176–184]. We first analyze the preferred 3D fiber orientations on simulated volumetric images generated for each classification. Next, we separate 3D-image stacks into

volume elements and compute the preferred fiber orientation in each volume element. Subsequently, we implement a decision that differentiates each classification by extracting quantitative features such as the number of preferred fiber orientations detected in a volume element, the 3D spread of preferred orientations, and the type of distribution in the 2D polar plot. To validate our results, we apply our decision process to experimentally obtained SHG images of porcine tendon cut in three different orientations with respect to the collagen fiber bundles and find our results to agree with the physical fiber organization.

5.2 Methods

5.2.1 3D collagen fiber classification

We classify 3D collagen fiber organization into five different types identified from common fiber arrangements found in biological tissues, as shown in Table 5.1. We define the “uniform” classification as fiber organizations that have relatively straight fibers, having a deviation of less than 20% relative to the aligned orientation. Tendon, which transmits tensile load and also experiences rotational forces, is primarily composed of uniform fibers [19,177,181]. The “crimped” classification indicates collagen fibers that have a crimp pattern with more than 20% modulation in amplitude with respect to the preferred fiber orientation and is not restricted to a single plane. In terms of the mechanical function, crimped fibers help absorb shock and are responsible for the low stress, non-linear stress-strain behavior in the so-called toe region that is associated with un-crimping [85,176,178,179]. Ligament, tendon and the tumor-stromal interface are example tissues that contain crimped fibers [66,85,176,178,179]. The “random” classification includes fibers with no particular preferred orientation, as observed in healing skin, tumors and the middle zone of cartilage, as examples [66,106,183]. Tissues with random fiber organization

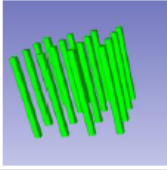
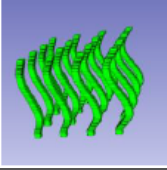
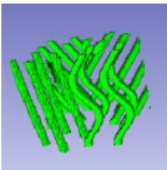
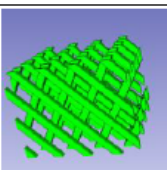
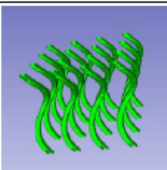
usually have a lower stiffness compared to those with uniformly aligned fibers measured along the preferred fiber direction and show isotropic mechanical behavior, i.e. have similar mechanical properties in all orientations. The “TFF” classification encompasses tissues with two distinct families of fibers that align in two preferred directions. TFF organization is found in arterial wall tissue, for example [168,184]. The TFF organization leads to anisotropic mechanical behavior of the tissue, with larger stiffness along the two major fiber directions compared to other directions. Lastly, “helical” classification includes fibers that, as fiber bundles, are aligned in a helical fashion in 3D. This fiber organization resists multidirectional forces. The anterior cruciate ligament and coronary arterial media [93,182] are both tissues that would be classified as having a helical fiber organization.

5.2.2 3D orientation analysis

We implement a custom MATLAB code that reads multiple images from 3D stacks in order to measure the preferred fiber orientation within a volume. A preconditioning step employs Canny edge detection algorithm [185] and detects the boundary of the fibers in the image. Next, the filter bank method [186] which applies multiple 3D filters in the Fourier domain, calculates the preferred 3D orientation of fibers in predetermined localized volume elements. A more detailed description of the basic code can be found elsewhere [21]. The designated volume elements are grouped into the following features: dark, anisotropic, 2-directional, or isotropic. Dark volume elements have an average intensity in the volume that is below 12% of the maximum intensity, whereas anisotropic, 2-directional, and isotropic have one, two or no detected preferred fiber orientation in the volume element, respectively. The preferred fiber orientation is calculated only when the

volume elements are anisotropic or 2-directional and saves a single orientation or two preferred fiber orientations, respectively.

Table 5.1: 3D collagen fiber classification

| Types | Representative image | Notes | Example tissue | Reference |
|------------------------|---|---|--|---------------------------------|
| Uniform |  | <ul style="list-style-type: none"> • Closely packed groups of uniform parallel collagen fibers • Transmits tensile load • Stores and returns elastic energy during locomotion in tendon | <ul style="list-style-type: none"> • Tendon • Lamella (bone) | [19], [172], [175], [176] |
| Crimped |  | <ul style="list-style-type: none"> • Sequence of waves within the collagen fibers • Helps absorb shock • Crimped fibers gradually extend and form a toe region during tensile loading | <ul style="list-style-type: none"> • Ligament • Tendon • Tumor-stromal interface | [63], [80], [171], [173], [174] |
| Random |  | <ul style="list-style-type: none"> • Randomly oriented fibers without a preferred orientation • Similar mechanical properties in all orientations • Smaller stiffness compared to uniformly aligned fibers | <ul style="list-style-type: none"> • Healing skin • Tumor • Cartilage • Cornea (Bowman's membrane) • Crown dentin | [63], [101], [178] |
| Two fiber family (TFF) |  | <ul style="list-style-type: none"> • Two helically arranged families of fibers • Leads to anisotropic mechanical behavior of tissue with larger stiffness along the preferred fiber orientations | <ul style="list-style-type: none"> • Arterial wall (adventitia) | [163], [179] |
| Helical |  | <ul style="list-style-type: none"> • Fibers with helical waveform in three dimensional space • Resist multidirectional forces | <ul style="list-style-type: none"> • Anterior cruciate ligament • Coronary arterial media | [88], [177] |

The code saves the preferred orientation information as two sets of angles (θ , ϕ), referring to the respective in-plane (x - y) and out-of-plane (z) preferred orientations, and the corresponding 3D vector. To visualize how the fibers are aligned in the volume of interest collectively, we plot the preferred 3D orientation data as a 3D histogram, which consists of vector distributions represented as 3D arrows [187] in an x - y - z coordinate reference frame. The direction of an arrow indicates the

preferred orientation in 3D space, whereas its length represents the number of volume elements (magnitude) within the volumetric image with the corresponding 3D orientation. This format provides an intuitive visualization of the preferred orientation of fibers and their overall spread in a fixed volume in a manner that is consistent with observed image data.

To quantitatively measure the spread of the fiber direction (the arrows) in 3D space, we employ the spherical variance (SV) parameter [161,188] defined as

$$SV = \frac{n - R}{n}, \quad 0 \leq R \leq n, \quad 0 \leq SV \leq 1 \quad (5.1)$$

where the length of the resultant R is given by

$$R = \left\{ \left(\sum_{i=1}^n l_i \right)^2 + \left(\sum_{i=1}^n m_i \right)^2 + \left(\sum_{i=1}^n n_i \right)^2 \right\}^{1/2} \quad (5.2)$$

$i=1, \dots, n,$

representing the magnitude of the vector (l_i, m_i, n_i) sum. The vector components l_i, m_i, n_i are the fiber orientation and n is the number of volume elements, excluding dark and isotropic volume elements. The SV ranges from 0 to 1, where 0 corresponds to no spread of the 3D orientations, and 1 corresponds to completely random organization.

To represent the preferred 3D orientations in a 2D format, we plot θ and ϕ in a polar histogram. On the polar histogram, each bin has a value on the corresponding angular and radial axes. The radial axis value represents the number of volume elements that have the preferred orientation equal to the corresponding angular axis value. We identify peaks in the θ polar plot based on the radial axis values. A peak is defined by initially identifying the radial axis values for each angular value and subsequently choosing eight radial axis values that are highest, namely local maxima.

We choose eight local maxima because in each z -layer we assumed there would be at most two peaks and total four z -layers are analyzed. Next, we calculate the average radial axis value of the four neighboring bins, two on each side, for each of the eight local maxima. A local maximum is identified as a peak if the average value from the neighboring bins is less than one third of the corresponding local maximum value. Supplementary information from the polar plots can be determined, such as the mean θ and ϕ angle, peaks in the polar plot being parallel or non-parallel, as well as their value and location.

5.2.3 Process of distinguishing 3d collagen fiber classifications

To organize steps that quantitatively distinguish different the five classifications, we apply the 3D orientation analysis to 25 different simulated images of each classification. The 25 cases are generated by randomly changing the key features of each classification, such as aligned orientation, crimp pattern amplitude, and radius of the helix within the defined range. Subsequently, we construct a stack of images for each classification that applies the features chosen. Based on the information from the 3D orientation analysis on the simulated images, we extract quantitative metrics including the volume element labels (anisotropic, 2-directional, isotropic), SV , and the number of peaks in the θ polar plot.

5.2.4 Experimental setup

From a local abattoir, we purchased frozen porcine feet and kept them frozen (-20°C) for less than 24 hours. Then the porcine feet were thawed, and deep digital flexor tendon was dissected. We prepared three types of samples by cutting the tendon at angles of 0° , 45° , and 90° with respect to the orientation of the collagen fiber bundles with a razor blade. We chose to use the

digital flexor tendon due to the dense collagen fibers resulting in a strong backward-SHG signal [57,58,189] and also because the mechanical properties of tendon are highly related to its function [149,177,190]. All three samples were cut from the same tendon with a thickness of ~5 mm each. The final step was to embed the samples in optimal cutting temperature compound and cut 5- μm thin sections along the surface of the samples to smoothen the surface.

For SHG imaging, we used a tunable Ti:Sapphire laser (Mai Tai, Spectra-Physics) producing 100-fs duration pulses and centered at 780-nm wavelength. The 15-mW input power beam focused on the sample with a 60X magnification and a 1.0 NA water immersion objective lens (U M PLAN FLN, Olympus). The backward SHG signal emitted by the sample traveled through the same objective, and a 390-nm bandpass filter (FF01-390/18-25, Semrock) blocked any potential autofluorescence from reaching the photomultiplier tube (H10721-110, Hamamatsu). The tissue samples were placed in a No. 1.5 cover glass bottom dish (P35G-1.5-20-C, MatTek) and the side to be imaged faced the bottom. We imaged all samples in 3D stacks of dimension $80 \times 80 \times 26 \mu\text{m}$, where the step size along the z -axis (axial direction) was 300 nm. To prevent the sample from drying while imaging, the sample was partially submerged in phosphate-buffered saline, which was collected in the petri dish before imaging.

5.3 Results and discussion

5.3.1 3D orientation analysis of simulated images for each classification

Figure 5.1 illustrates the volumetric spatial analysis on the simulated images from the five classifications of fiber organizations discussed in Table 5.1. Column (a) through (e) show the uniform, crimped, random, TFF, and helical classifications, respectively. Each image consists of $6 \times 6 \times 4$ volume elements that are $\sim 14 \times 14 \times 14 \mu\text{m}$. Figure 5.1 row (i) shows the calculated

preferred 3D orientation for each classification. Here, we use 3D slicer (4.9.0, BSD-style license) [191] to visualize the five simulated fiber organizations; the calculated preferred fiber orientations are plotted as arrows overlaid on half of the volumetric image. The yellow arrows indicate the case of two dominant preferred fiber orientations in a single volume element. The uniform fiber organization shows similar arrow directions throughout the volume compared to the other classifications. The arrows in the crimped fiber organization show the crimp pattern while for the random fiber organization, there is no identifiable trend in the preferred orientation. The TFF organization shows yellow arrows in most of the volume elements, whereas the helical fiber organization shows a helical arrangement of arrows. The region labels in Fig. 5.1 row (ii) show the result of grouping each volume element into either anisotropic, 2-directional, or isotropic. There are no volume elements labeled as dark since our simulated images are intended to have dense fibers throughout the volume.

In Fig. 5.1, the MATLAB code identifies some of the volume elements on the edge of the 3D images as 2-directional or isotropic where they should be anisotropic and 2-directional, respectively. This mislabeled result came from the sharp contrast between the background and fibers at the edge of the volume of interest. Sharp contrast requires an infinite summation of spatial harmonic waves to synthesize the edges, but instead, the MATLAB code employed in the analysis approximates to a finite number of spatial frequencies [192]. This approximation causes the aforementioned erroneous labels; however, the percentage of these inaccurate labels is negligible (less than 3% of the entire volume).

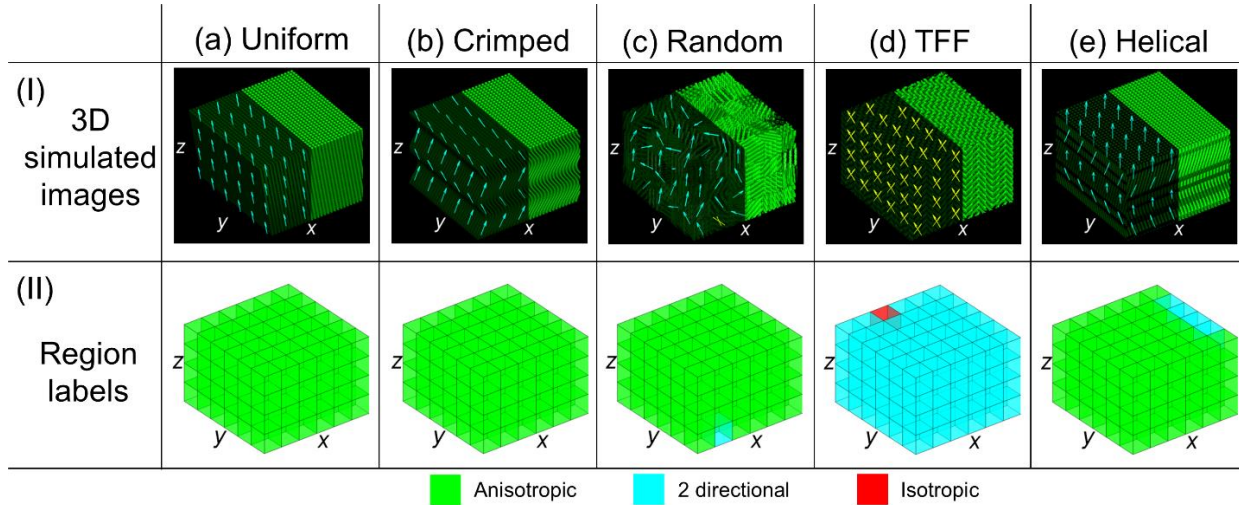


Figure 5.1: Volumetric spatial analysis of simulated 3D fibers. (i) 5 classifications of simulated 3D fiber organization, where (a)-(e) refers to uniform, crimped, random, two-fiber family (TFF), and helical, respectively. For each simulated image, half the volume shows the rendered fiber organization and half shows the calculated preferred 3D fiber orientation. The arrows represent local preferred fiber orientations, where the yellow arrows specifically indicate the presence of two dominant preferred fiber orientations. (ii) Label of each classification of fiber organization per volume element as either anisotropic (green), 2-directional (cyan), or isotropic (red). All images have the same view angle.

Figure 5.2 shows the further analyzed preferred 3D orientation data of the simulated images for each classification illustrated in rows (a) through (e). The 3D orientation histograms are in the first column of Figure 5.2, and the projections in the x - y , y - z , and x - z planes are in the same column immediately to the right. The colors for each arrow represent their relative magnitude within the image, where the colors are blue, cyan, yellow, and red in the ascending order of the relative magnitude (see the scale in the lower right corner of Fig. 5.2). The polar plots for θ and ϕ are in the second column. The range of each angle ($0^\circ < \theta < 360^\circ$, $0^\circ < \phi < 90^\circ$) is defined to include the cases for $z > 0$, and the angular resolution of each polar plot is 10° .

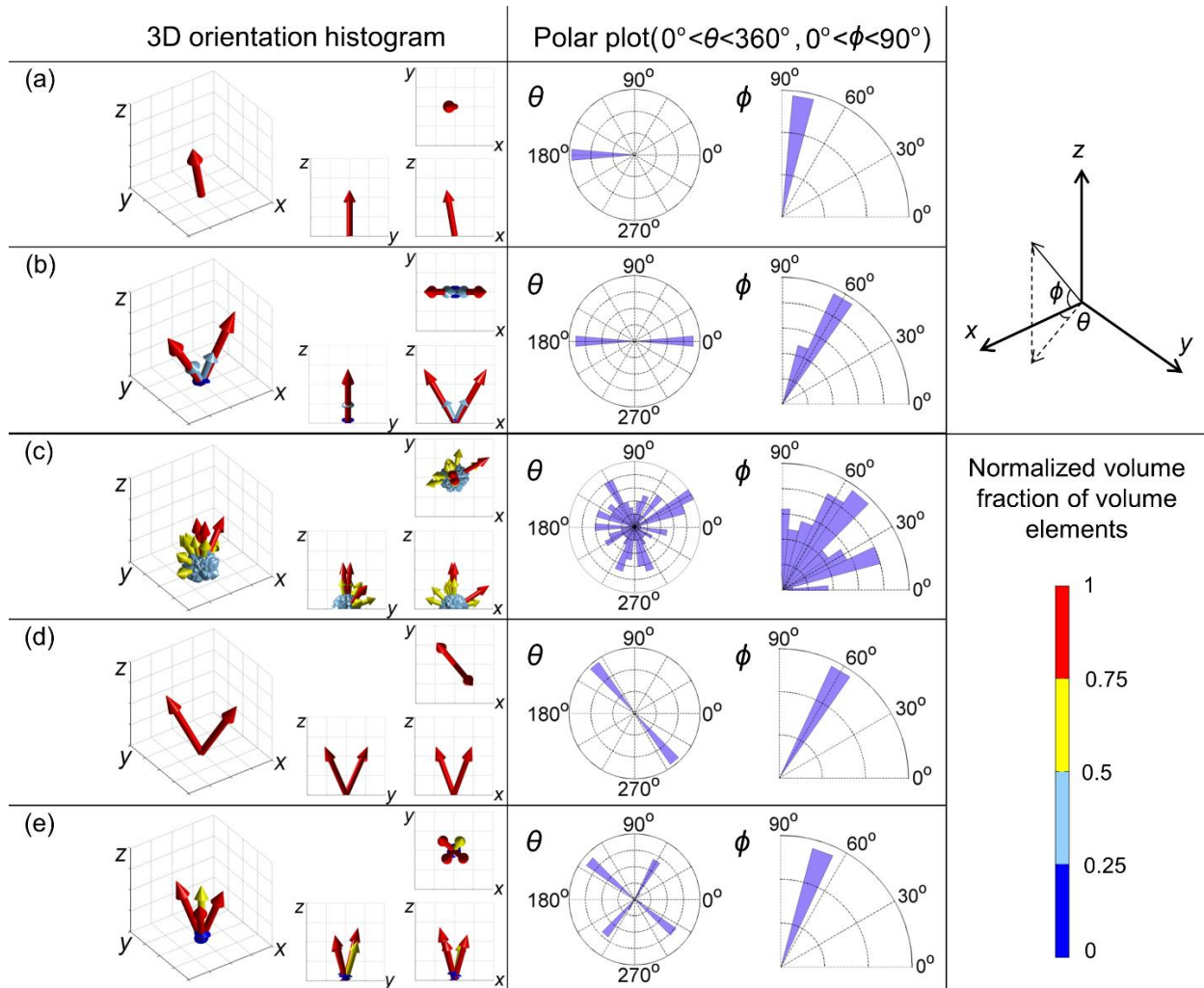


Figure 5.2: Quantitative 3D orientation analysis on each simulated collagen fiber classification. (a)-(e) represent uniform, crimped, random, TFF, and helical classification, respectively. The 3D orientation histogram in the first column is the computed preferred 3D fiber orientations for each classification (first column in Fig. 5.1), and the view angle is the same as Fig. 5.1. The corresponding x - y , y - z , and x - z projections are adjacent. The color scale in the bottom right indicates the relative contribution to a particular preferred orientation. The polar plots in the second column indicate the θ and ϕ angles ($0^\circ < \theta < 360^\circ$, $0^\circ < \phi < 90^\circ$) for the corresponding 3D orientation histogram in the first column. A coordinate reference shows the angles θ and ϕ relative to the x , y , and z -axes in the top right.

The uniform classification [Fig. 5.2(a)] has a single arrow in the 3D orientation histogram, representing the only one fiber direction. The fiber direction according to the corresponding polar plots is $\theta = 180^\circ$ and $\phi = 80^\circ$. The 3D orientation histogram for the crimped classification [Fig.

5.2(b)] has two major arrows, which correspond to the crimping directions of a band of fibers. The θ polar plot shows that the crimped pattern occurs in a single 2D plane since the θ polar plot has two peaks that are 180° apart. The ϕ polar plot for the crimped fiber organization, which reflects the out-of-plane angles of the arrows in the 3D orientation histogram, has an angular range from 55° to 75° . In the random classification [Fig. 5.2(c)], arrows point various directions in the 3D orientation histogram and, as a result, there is no particular fiber direction in the θ polar plot. This distribution trend is also evident in the ϕ polar plot. The 3D orientation histogram for the TFF classification [Fig. 5.2(d)] shows the fiber orientations of the 2-directional grouped volume elements (yellow arrows in Fig. 5.1). There are two peaks in the θ polar plot and one angular bin in the ϕ polar plot which result from the simulated TFF example having the same two fiber directions in all the volume elements analyzed. The helical classification [Fig. 5.2(e)] has four dominant arrows in the 3D orientation histogram representing the helical pattern for each z -layer. Four peaks are in the θ polar plot, and each peak corresponds to one z -layer of volume elements. The peaks in the θ polar plot rotate either clockwise or counter-clockwise as the z -layer increases. This characteristic distinguishes the helical from the crimped classification where the peaks in the θ polar plot do not rotate along the z -layer. The ϕ polar plot has a single bin since the range of the out-of-plane angles among the arrows in the 3D orientation histogram is less than 10° .

We employ a normalized spherical variance SV_N , which is defined by normalizing the SV to 0.4 and for the representative classifications is 0, 0.2973, 0.8138, 0.3350, and 0.1508 for uniform, crimped, random, TFF, and helical, respectively. 0.4 is the maximum SV from our 3D orientation analysis. In the analysis, we limit the volume of the 3D orientation histogram to the upper four quadrants in the x - y - z coordinate reference frame ($z > 0$) so the range of the θ , ϕ angles are $0^\circ < \theta < 360^\circ$, $0^\circ < \phi < 90^\circ$. Thus, no arrows are pointing along the $-z$ direction. Also, we do not

consider cases for which the mean ϕ angle is less than 40° because fibers in this range of angles can be considered as a 2D organization and also can substantially increase the SV when the 3D volume is limited to the upper four quadrants. As a result, the maximum SV is ~ 0.4 , which is when the mean ϕ angle is 40° and the θ angles are evenly distributed.

Figure 5.3(a) shows the averaged volume fraction of each region label (2-directional, isotropic, anisotropic) for 25 cases for each classification. The average volume elements labeled as anisotropic are more than 85% for all the cases except for TFF classification. The TFF classification has more than 85% of 2-directional volume elements. Figure 5.3(b) shows the average SV_N for each classification. The uniform classification has the minimum value, close to 0, and the random classification has the maximum value, greater than 0.8. The SV_N of crimped, TFF, and helical classification have a similar SV_N , which is greater than for the uniform classification and less than the random ranging from 0.21 to 0.32.

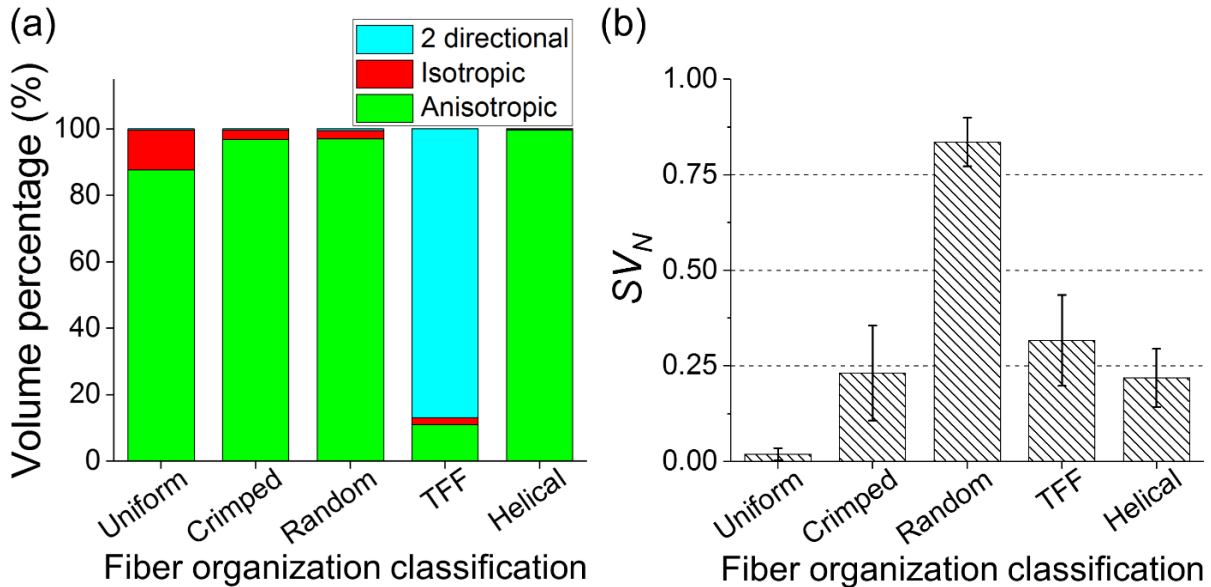


Figure 5.3: Quantitative metrics from the 3D orientation analysis for 25 simulated images per classification. (a) The average volume composition of volume elements and (b) the average SV_N for each classification, presented as mean \pm standard deviation.

5.3.2 Quantitative classification

Figure 5.4 depicts the quantitative classification process. First, a volumetric image, which has one of the already defined five classifications, is input to the classification process and, as a result, divided into one of three cases depending on the labeled volume elements (anisotropic, 2-directional, isotropic). When the volume elements are mostly ($> 80\%$) isotropic, it indicates that there is no preferred fiber orientation within each volume element. If the volume elements are mostly ($> 80\%$) 2-directional, then the 3D image is classified as TFF. The 3D images that primarily have anisotropic volume elements are divided into two groups based on the SV_N . 3D images with small SV_N (< 0.075) are identified as uniform. The SV_N threshold we adopt, 0.075, is calibrated based on our simulation data and for applying the analysis to experimentally obtained images from a range of different fibrous tissues, the value may need recalibration from the 3D orientation analysis. However, the general trend, which is small SV_N representing uniform fiber organization and large SV_N representing crimped, helical, and random fiber organization would still be valid. 3D images that have a SV_N greater than 0.075 require further analysis, starting with the θ polar plot. When there are no peaks in θ polar plot, the 3D-image classification is random. For the cases that have peaks, we analyze the corresponding z -layer for each peak. As previously mentioned, when the peaks have an order rotating clockwise or counter-clockwise in the ascending z -layer, the 3D-image classification is helical. The 3D images that do have peaks in the θ polar plot, but do not rotate in the ascending z -layer, are classified as crimped, as do those with a θ polar plot with a single peak. Lastly, we note that although in the simulated random classification data the SV_N is greater than all other classifications, we choose not to use SV_N alone to separate it from the others. This is because of the simulated image data used in Fig. 5.3 only considers random cases when the preferred fiber orientation in each volume element is uniformly distributed. However, there are a

variety of random fiber organizations resulting in a wide range of SV_N , thus relying only on SV_N to distinguish random classifications from others could be misleading.

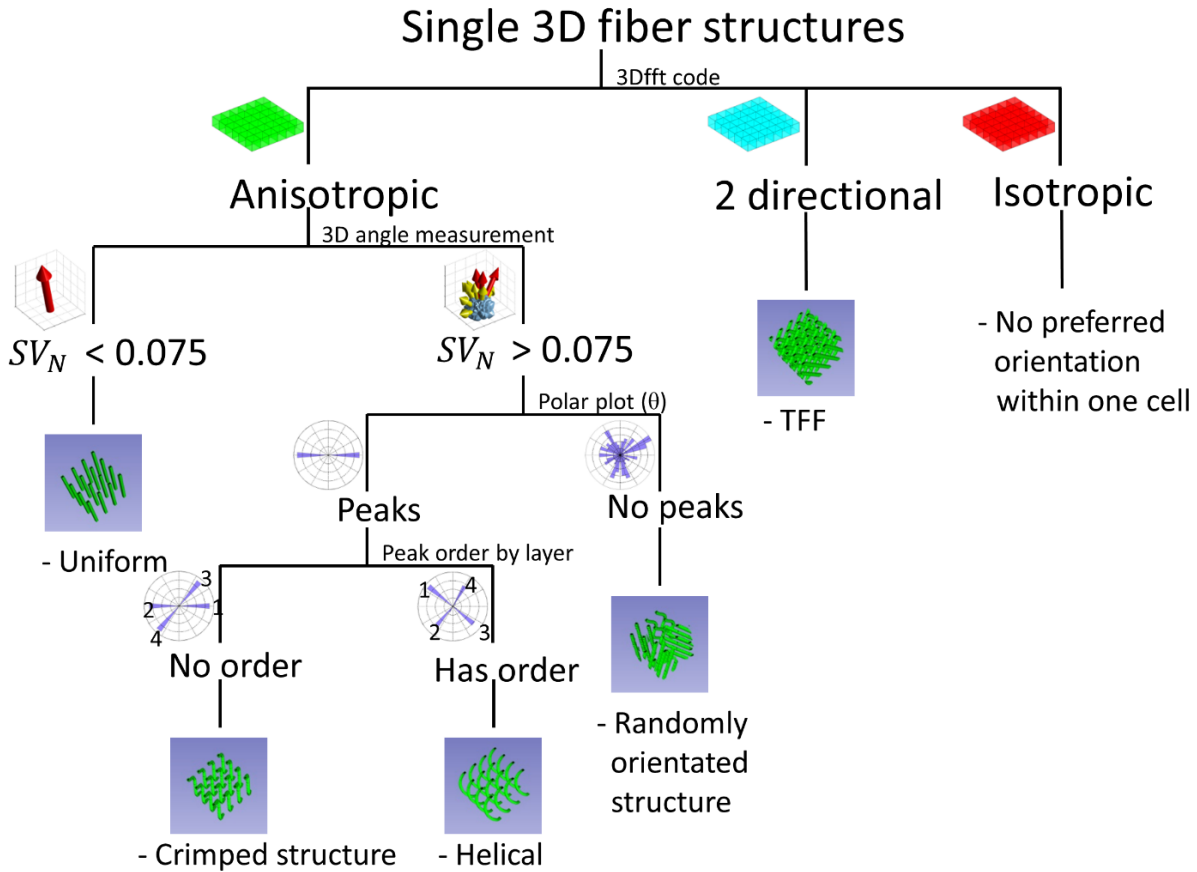


Figure 5.4: Decision process for identifying 3D fiber classifications. A volumetric image is assumed to have one of the already defined classifications. The image is subsequently sorted into one of the three labels, anisotropic, 2-directional, and isotropic. Anisotropic volumes are then separated based on their computed SV_N , where those with $SV_N < 0.075$ are identified as uniform, and otherwise a volume is classified as crimped, helical, and randomly oriented fibers by further analyzing the θ polar plot. 2-directional volumes are classified as TFF.

5.3.3 3D orientation analysis and quantitative classification applied to 3D-SHG images of tendon

Figure 5.5 illustrates the volumetric spatial results of the 3D orientation analysis for the 0° (parallel), 45° , and 90° (perpendicular) cut samples, respectively [Fig. 5.5(a)-(c)]. Figure 5.5 row (i) shows a representative SHG image from the 3D-image stacks, and the 3D rendered images

in Fig. 5.5 row (ii) combine multiple 2D images. The preferred 3D orientation arrows overlaid on the rendered image show the fiber organization, where the calculated mean ϕ angles are 8.26° , 49.14° , and 66.13° for the 0° , 45° , and 90° cut samples, respectively. The mean ϕ angle values match well with the physically cut angle, where the 2D-SHG images in the first row give a sense of the dominant fiber direction through general features, e.g., the length of the discernable fibers are longest in Fig. 5.5(a) and shortest in Fig. 5.5(c). The potential angle offset is due to sample heterogeneity and fiber misalignment while cutting the sample. Fig. 5.5 row (iii) shows the region labels of each sample, where most of the volume elements are anisotropic, and a few are dark and isotropic. The considerable amount of dark and isotropic volume elements compared to the simulated images in Fig. 5.1 is because of the irregular fibers within the sample and the lower contrast in the SHG images. In addition, an inherent artifact caused by the sharp contrast in the simulated images mentioned above plays a role in the appreciable amount of non-anisotropic volume elements on the edge. There are no volume elements that are labeled as 2-directional in all three samples.

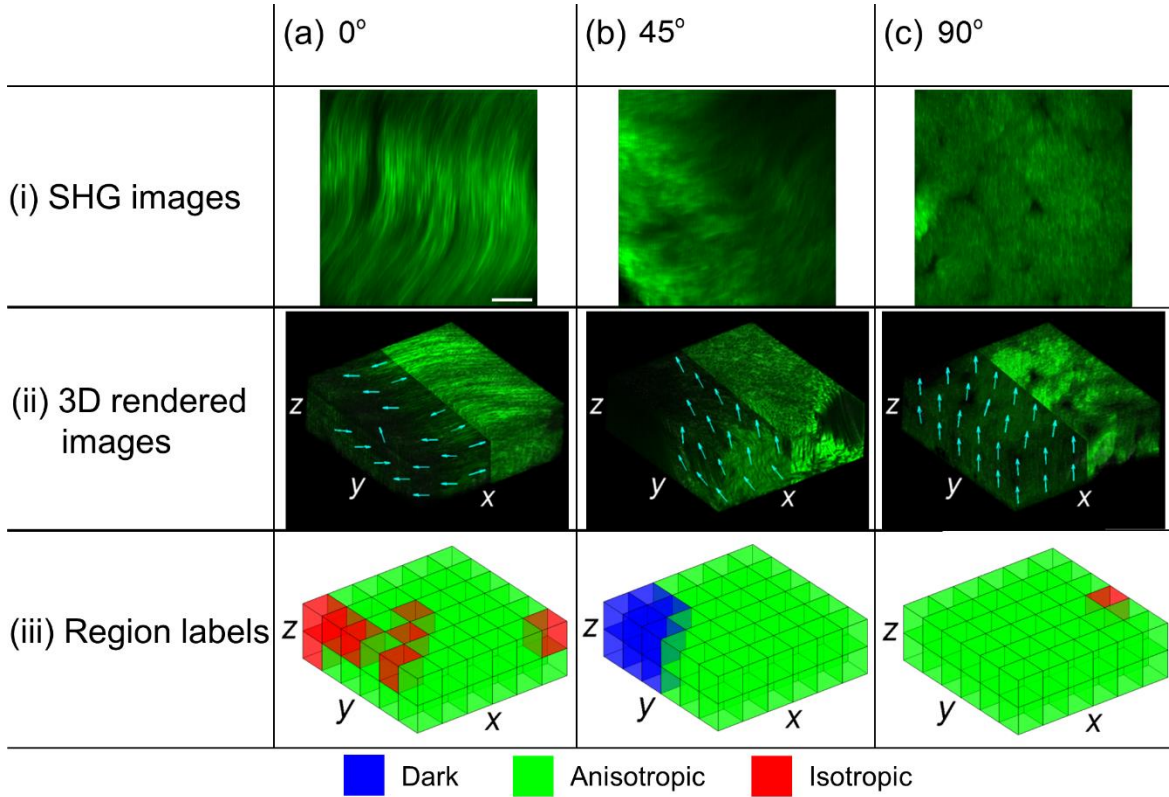


Figure 5.5: Volumetric spatial analysis of SHG images of porcine tendon. Fresh tendon samples cut at (a) 0°(parallel), (b) 45°, and (c) 90°(perpendicular) with respect to the collagen fiber bundles. (i) A representative 2D-SHG image from the stack and (ii) the 3D rendered image where the computed preferred 3D fiber orientations are plotted on half of the volume. (iii) Label of each classification of fiber organization per volume element as either dark (blue), anisotropic (green), and isotropic (red). All images are in the same view angle. Scale bar is 20 μm .

Results from 3D orientation analysis from the tendon SHG images are in Fig. 5.6, where Fig. 5.6(a)-(c) refers to the 0°, 45°, and 90° cut samples, respectively. The 3D orientation histogram is in the first column to the left of Fig. 5.6 and the projections in x - y , y - z , and x - z planes are immediately to the right in the same column. The arrow colors (blue, cyan, yellow, and red) represent their relative magnitude, and the scale is located on the right in Fig. 5.6. For all three cases, the arrows mainly have a small deviation ($\leq 40^\circ$ for both θ and ϕ) with respect to their main preferred orientation shown as a red arrow in the 3D orientation histogram. For the 0° cut sample [Fig. 5.6(a)], the range of θ and ϕ angles is $-90^\circ < \theta < 90^\circ$, $-90^\circ < \phi < 90^\circ$. This is because the mean

ϕ angle is smaller than 40° . When $\phi < 40^\circ$, the upper four quadrant range ($z > 0$) will erroneously increase the SV calculation and by converting θ, ϕ to $\theta \pm 180^\circ, -\phi$ and changing the angle ranges ($-90^\circ < \theta < 90^\circ, -90^\circ < \phi < 90^\circ$) the new SV decreases substantially. The polar plots for θ and ϕ in the second column have an angular resolution of 10° and are plotted based on the θ and ϕ range for each sample. The θ polar plots for all samples have a peak at $-20^\circ, 110^\circ$, and 60° in Fig. 5.6(a)-(c), respectively. The ϕ polar plots have a narrow angular range, which reflects the small deviation of arrows in the 3D orientation histogram.

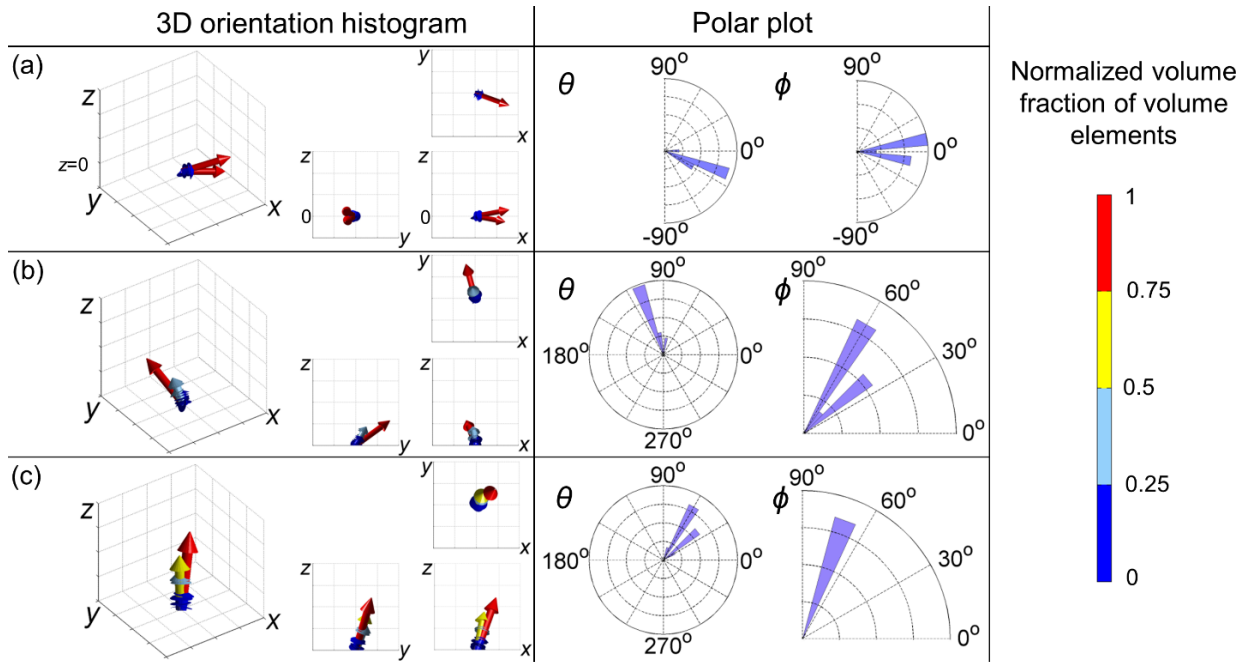


Figure 5.6: Quantitative 3D orientation analysis applied to SHG images of porcine tendon cut at (a) 0° , (b) 45° , and (c) 90° relative to the collagen fiber bundles. The 3D orientation histogram in the first column indicates the computed preferred 3D fiber orientation for each sample, and the view angle is the same as in Fig. 5.5. The corresponding x - y , y - z , and x - z projections are on the right. The relative contribution to a particular preferred orientation direction is indicated by the color bar in the right panel. The polar plots in the second column indicate the θ and ϕ angles for the corresponding 3D orientation histogram in the first column. The range of the angles are $0^\circ < \theta < 360^\circ$ and $0^\circ < \phi < 90^\circ$ except for (a) 0° cut case where it is $-90^\circ < \theta < 90^\circ$ and $-90^\circ < \phi < 90^\circ$ due to the low mean ϕ angle.

Figure 5.7 illustrates the volume fraction of each region label (dark, isotropic, anisotropic) and SV_N value for the SHG images of tendon cut at 0° , 45° , and 90° . In Fig. 5.7(a), the majority of the volume elements ($> 85\%$) are determined as anisotropic for all three samples. In Figure 5.7(b), the SV_N value is 0.0875, 0.0853, and 0.0130 for the 0° , 45° , and 90° cut samples, respectively. Based on the classification procedure shown in Fig. 5.4, the 0° and 45° cut samples are classified as crimped whereas the 90° cut sample is classified as uniform. This result is because SV_N for the former two cases is greater than 0.075 and has a single peak in the θ polar plot, whereas the SV_N for the latter case is less than 0.075 while still having a single peak in the θ polar plot. Studies have shown that tendon collagen fiber organization varies with spatial location [94,193,194], which explains our results classifying the porcine tendon sample on different locations as uniform or crimped. The actual crimping pattern in the SHG images can be found in Fig. 5.5 row (ii)-(a), (b), where the preferred 3D orientation arrows change direction throughout the volume.

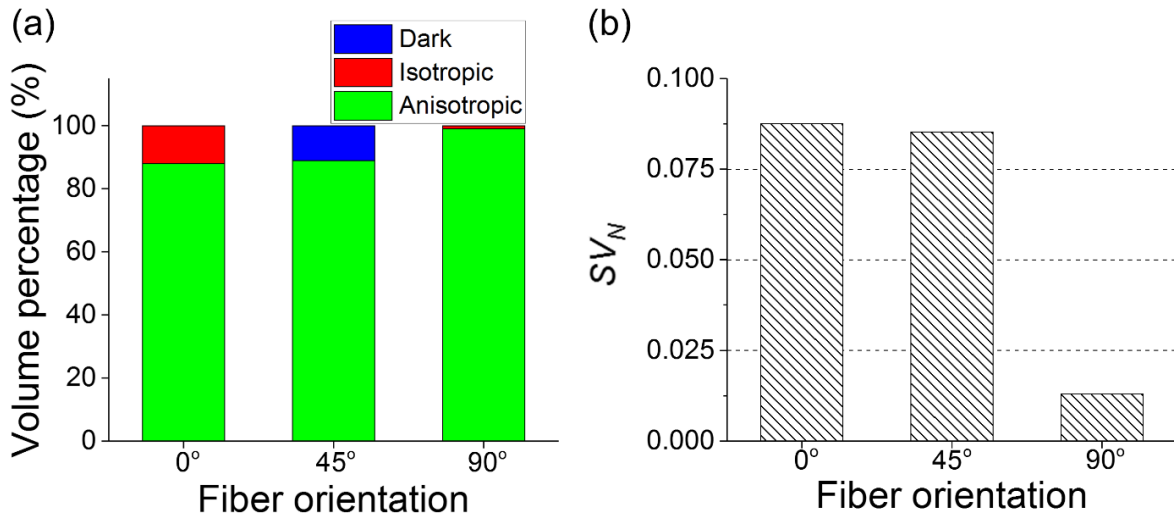


Figure 5.7: Quantitative metrics from the 3D orientation analysis for the SHG images cut at 0° , 45° , 90° with respect to the collagen fiber bundles. (a) The volume composition and (b) the SV_N for each sample.

5.4 Conclusion

In this chapter, we proposed an algorithm to quantitatively classify 3D collagen fiber organization directly from volumetric images into uniform, crimped, random, TFF, and helical classifications. We demonstrated a method that calculated the preferred 3D fiber orientation on simulated images for each classification and subsequently labeled the volume elements into dark, anisotropic, 2-directional, or isotropic. With regards to the results of the 3D orientation analysis, we implemented a decision process that distinguished the 3D collagen fiber classifications based on quantitative metrics derived from features such as SV and preferred 3D fiber orientation. Subsequently, we applied the 3D orientation analysis to 3D-SHG images of porcine tendon for three samples, each cut with a different orientation relative to the long axis of the tendon. Two samples were classified as crimped, and the third were classified as uniform. In Chapter 6 & 7, we apply the quantitative classifications on different types of 3D complex collagen organizations.

CHAPTER 6. 3D COLLAGEN FIBER ORGANIZATION ANALYSIS APPLIED ON MOUSE EXTRAHEPATIC BILE DUCTS

6.1 Introduction

The extrahepatic bile ducts (EHBDs) are small tubes connecting to the intrahepatic bile duct network at the hilum of the liver and coalescing into a single duct outside the liver; they permit bile flow from the liver and gall bladder to the gut. EHBD comprises a layer of biliary epithelial cells (cholangiocytes) lining the lumen, and submucosa adjacent to the biliary epithelial cells. The submucosa contains collagen, blood vessels, interstitial fibroblasts, and peri-biliary glands. The epithelial cells form an impermeable barrier between the lumen and submucosa region. Bile, which is primarily composed of water with electrolytes and toxic bile salts, is made by hepatocytes in the liver but stored in the gall bladder and released when food is digested; it contributes to fat digestion. EHBD malfunction, preventing bile flow, can lead to liver damage due to the accumulation of bile in liver. EHBD diseases include biliary atresia is a disease of newborns that is the main cause of liver transplantation [195,196]. Other important EHBD diseases include primary sclerosing cholangitis and cystic fibrosis liver disease [197,198].

Recently, researchers have shown that the EHBD submucosa region consists of a complex collagen network surrounding large fluid and glycosaminoglycan-filled spaces [199], and this structure changes as a function of age [196]. Specifically, neonatal EHBDs have a small volume (less than 1% of the duct area) of scattered collagen fibers whereas, adult EHBDs have a network of collagen bundles contributing to more than 20% of the duct area. Understanding the development of this collagen network in EHBDs is important to understanding the development of diseases such as biliary atresia and establishing methods to cure them. However, there are very

few studies conducted on analyzing the growth mechanism of the complex structure of collagen fibers in EHBDs.

In this chapter, we aim to quantitatively investigate the growth of the 3D collagen fibers in mouse EHBDs cut near liver and gut in multiple age groups ranging from neonatal to 2-year-old mice. SHG volumetric images are collected on the longitudinal and radial plane of the EHBD, and we calculated the 3D structure parameters including, *dark*, ϕ , and *SV*. The parameters are found to gradually change with age and implied that fibers moderately take up space and form a crimp pattern when growing.

6.2 Methods

Mouse (BALB/c) EHBDs of eight age groups (day 2, 4, 5, 6, 7, 10, Adult, and 2-year-old) were cut at the liver and gut junction as shown as the red points in Fig. 6.1(a). Each age group had two to five samples except for the 2-year-old EHBD cut near liver ($n=1$). The isolated EHBDs were fixed in 4% formalin for 10 minutes and stored in buffer solution until SHG imaging. We obtained SHG images at the longitudinal \times radial plane of the cut near gut and near liver sample, respectively. Fig. 6.1(b) shows a schematic diagram of the EHBD while Fig. 6.1(c) illustrates an H&E stained cross-section of EHBD showing the locations of submucosa and epithelium. The SHG z -stacks images were collected by a commercial upright microscope (DM 6000, Leica) with a 25X 0.9 NA water immersion objective lens with a 4X zoom factor and the dimension for each image stack was $140 \times 140 \times 15 \mu\text{m}$. Both forward and backward scattered SHG images were collected. To observe the general organization of collagen fibers in mouse EHBD, we used the same objective lens with a 2X zoom factor, resulting in image stacks of a dimension that is $280 \times 280 \times 55 \mu\text{m}$. All work with mice was in accordance with protocols approved by the University of

Pennsylvania per the national institutes of health guide for the use and care of animals. All the sample preparation and imaging was conducted at the University of Pennsylvania by a collaborator Dr. Jessica Llewellyn.

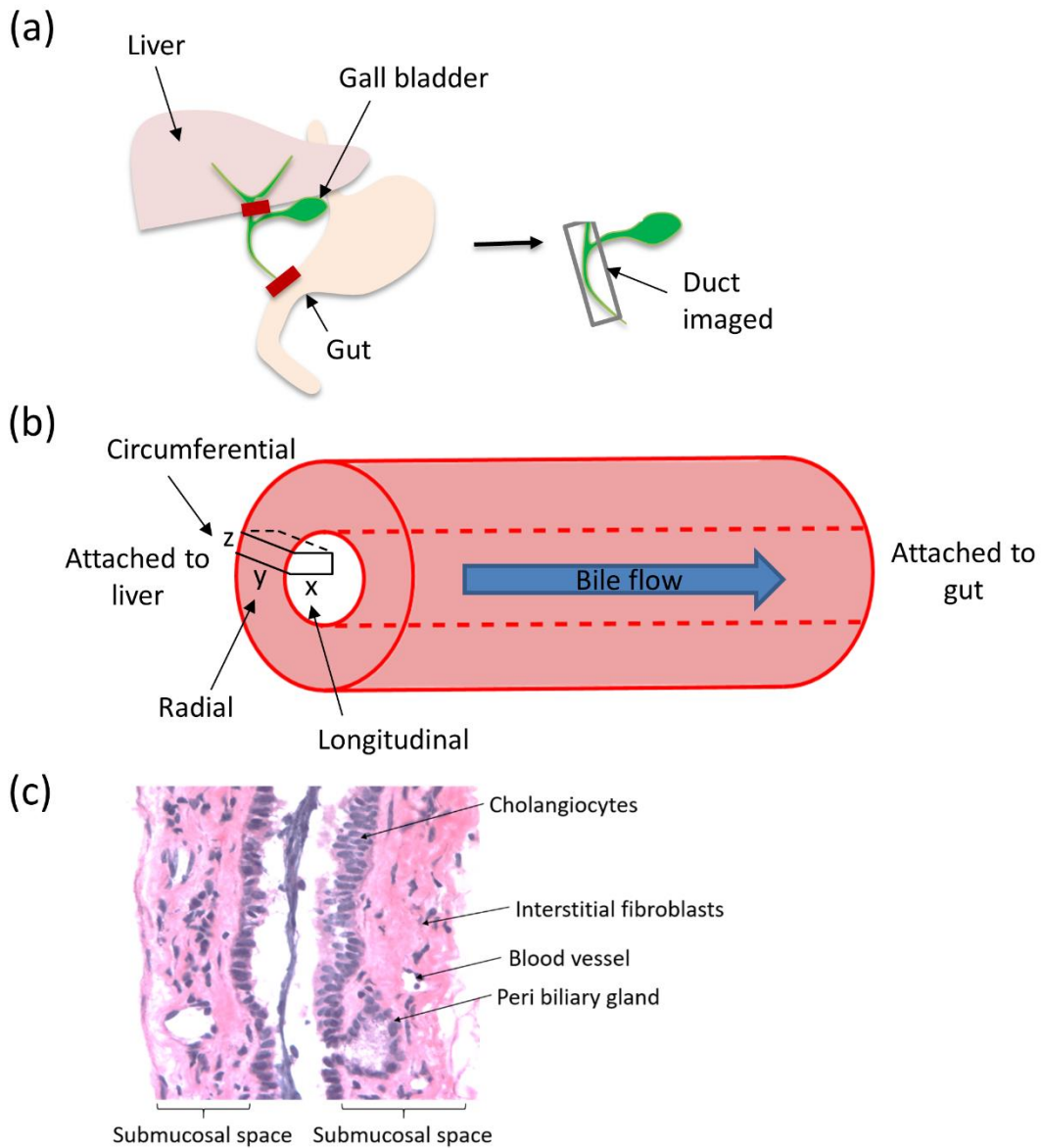


Figure 6.1: EHBD sample (a) removed from liver and gut and (b) imaged on the radial \times longitudinal plane. (c) A representative H&E image of EHBD.

Areas including the boundary and external area were cropped out, resulting in a volumetric image of solely the EHBD for the 3D-image analysis. The longitudinal, radial, and circumferential axis of the sample was the x , y , and z -axis of the image, respectively. 3D parameters such as $dark$, ϕ , and SV were measured, which indicates the non-collagenous volume, out-of-plane collagen fiber angle, and the 3D orientation spread, respectively. Details for measuring the parameters are in Chapter 5.

6.3 Results and discussion

Figure 6.2 illustrates the forward SHG images obtained on the longitudinal–radial plane of the EHBDs from each age group. The submucosal area contains collagen fibers mainly aligned along the longitudinal direction for all age groups, while the external area has no SHG intensity. The submucosal wall thickness increases from 45 to 70 μm with age. The SHG signal intensity is noticeably lower in the younger age group (day 2, 4) images as opposed to day 10 and adult group images. We use all SHG images from forward detection because backward SHG had low intensity in some samples where it could potentially cause misleading results.

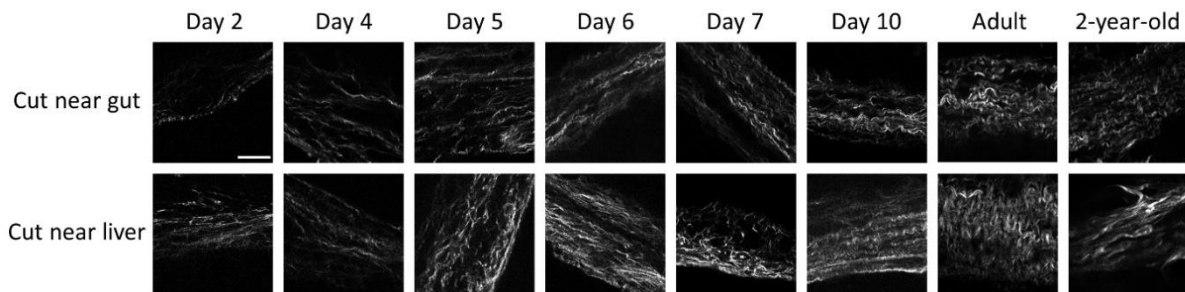


Figure 6.2: 2D-SHG images of each age group. Scale bar is 40 μm .

Figure 6.3 displays representative volumetric spatial results of the 3D orientation analysis for days 4, 5, 6, 7, and 10 samples cut near gut. The SHG images in Fig. 6.3 column (i) are the cropped out images excluding the external area with no SHG signal. Fig. 6.3 column (ii) displays the 3D rendered image for each group while Fig. 6.3 column (iii), (iv) are the SHG 3D-image analysis results showing the 3D orientation of collagen fibers as arrows and the region labels for each volume element. Note that the dark volume elements gradually decrease with age. Fig. 6.3 column (ii)-(iv) all have the same view angle. The size of the SHG image varies by age group since the size of the volume chosen to crop out is different in each image however, the volume elements used are all $6 \times 6 \times 6 \mu\text{m}$.

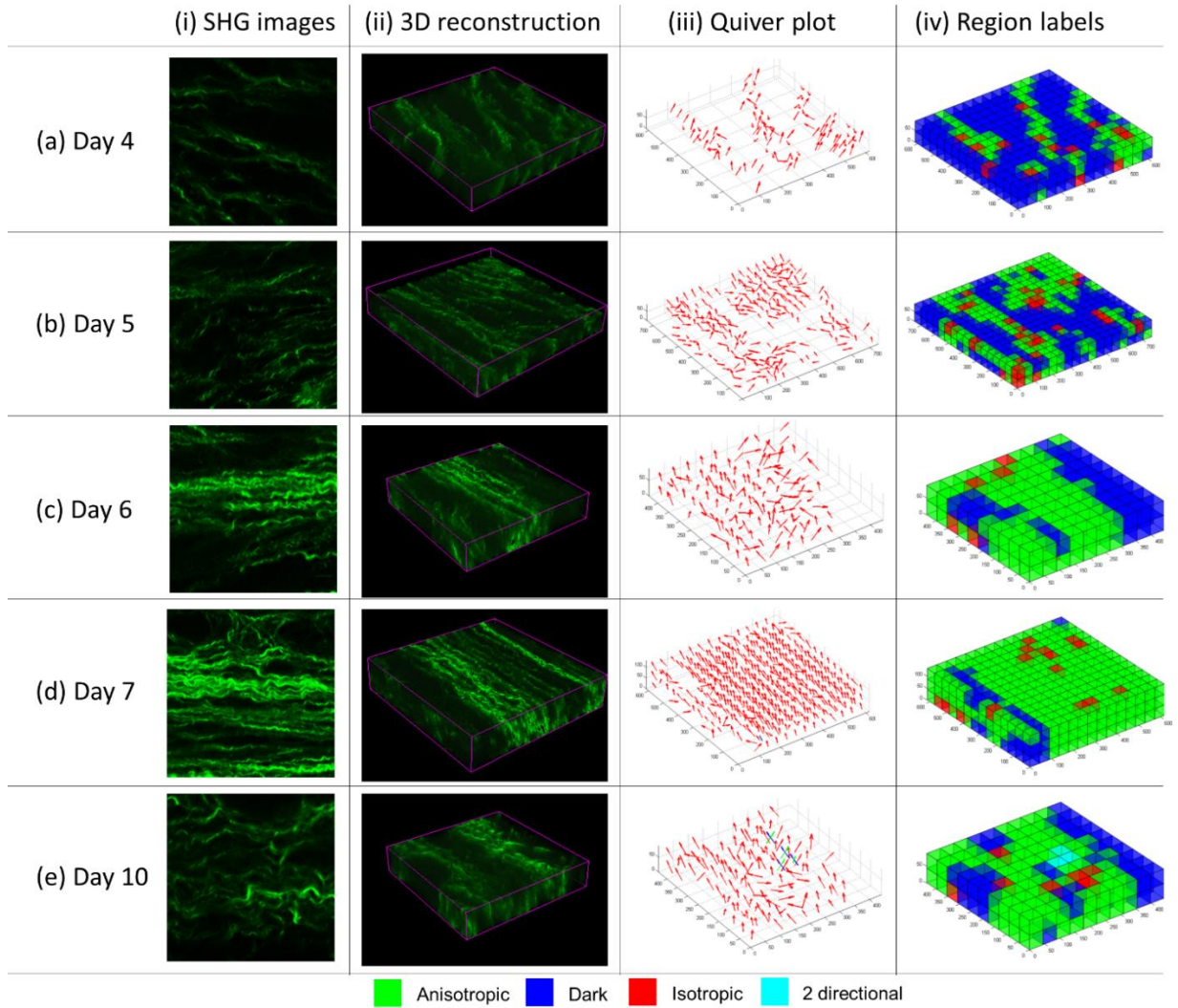


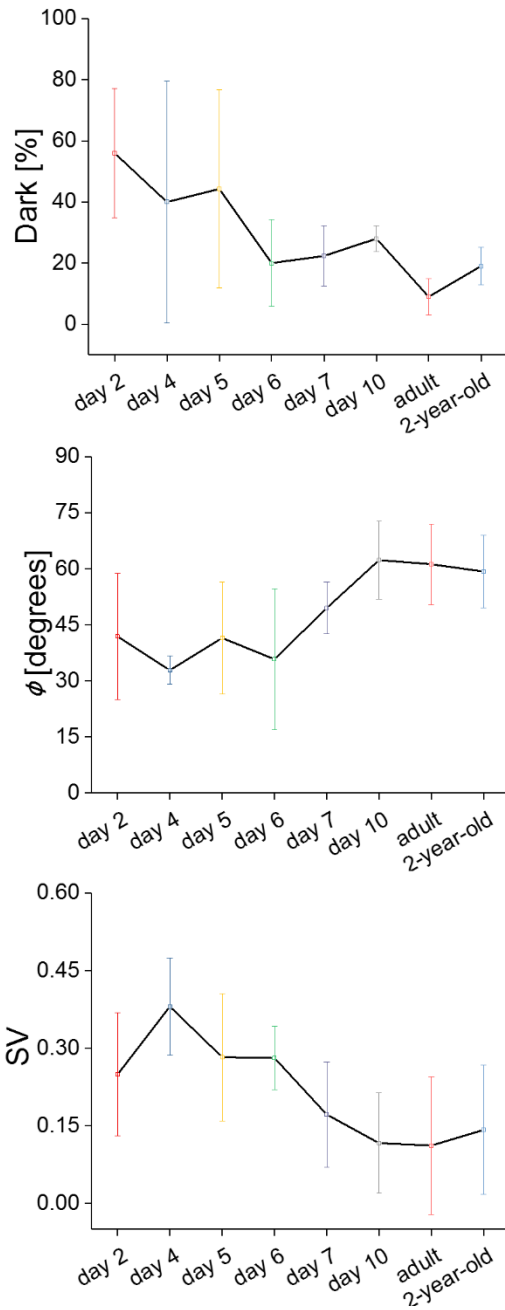
Figure 6.3: 3D-SHG fiber analysis in each age group. See text for details.

The measured *dark*, ϕ , and *SV* for each age group are shown in Fig. 6.4 as a scattered plot format. The error bars refer to the standard deviation. On the scatter plots of the cut near gut samples [Fig. 6.4(a)], *dark* and *SV* gradually decreases while ϕ increases with age. The parameter *dark* decreasing indicates that the non-collagenous volumes are decreasing, which is reasonable since as the collagen fibers grow, they are prone to fill in the empty space in the submucosal area. The error bars are wider for days 2, 4, and 5 compared to days 6, 7, and 10 samples, which means

the fiber growth rate varies more in the early stage. The ϕ increasing may indicate the fibers beginning to align in the circumferential direction but also could be the level of fiber crimping increasing as the fibers grow. Lastly, SV gradually decreasing may indicate the range of the fiber orientation is wider in the younger samples, and the older samples tend to have more aligned fibers. This trend could be because when the fibers initially start to grow, their orientation is more irregular but gradually align to the longitudinal direction with time. The average SV values for all the age groups are above 0.1, which indicates that the collagen fibers are not uniform, according to the calculation conducted on the simulated fibers in Chapter 5. The plots from the cut near liver samples [Fig. 6.4(b)] followed a similar but weaker trend with the cut near gut sample plots.

3D rendered images from the SHG images of a wider field of view of representative images are illustrated in Fig. 6.5. It is clearly observable that the fibers mainly align along the longitudinal direction regardless of their age. On the other hand, the amount of crimping becomes more pronounced in the older groups compared to the day 2 sample. The crimping pattern is in the radial and circumferential direction, which affects the ϕ value to increase in the older sample groups, as shown in Fig. 6.4.

(a) Cut near gut



(b) Cut near liver

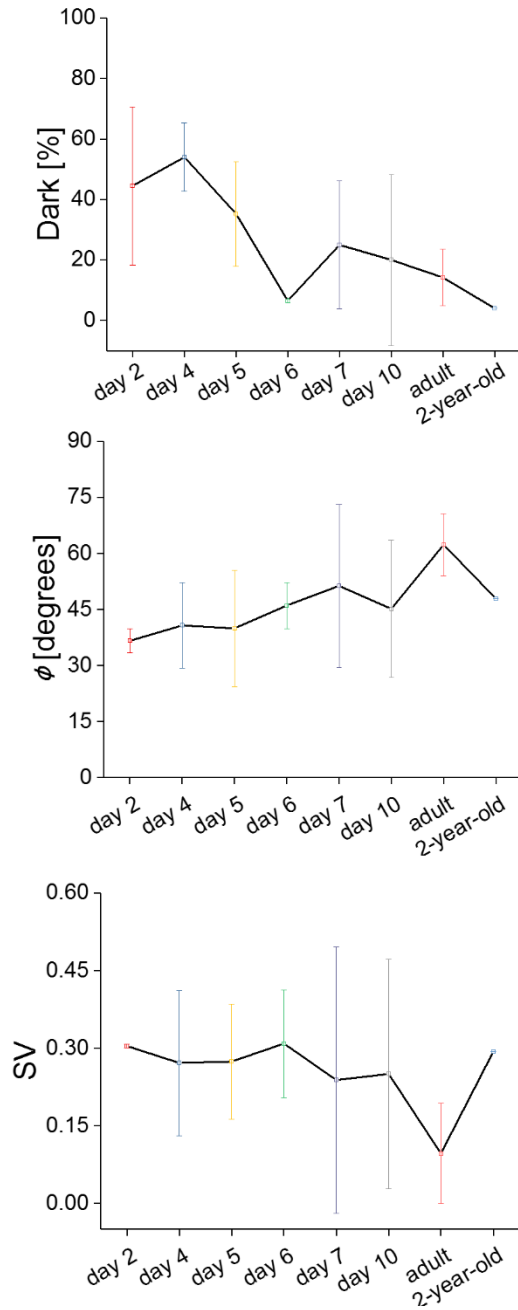


Figure 6.4: Scattered plot of the 3D parameters versus age group on (a) cut near gut and (b) cut near liver samples, respectively.

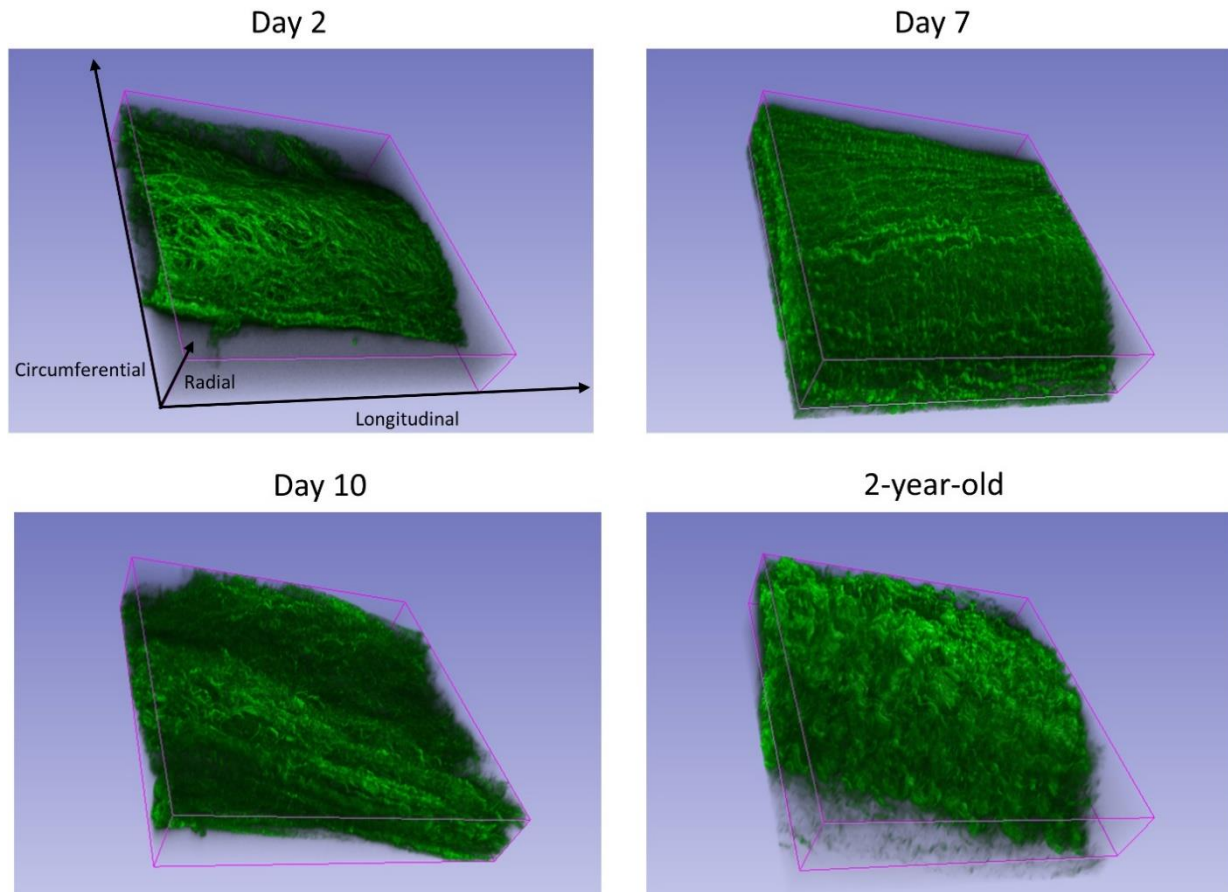


Figure 6.5: 3D rendered images of days 2, 7, 10, and 2-year-old EHBD.

There are a few possible reasons why the amount of crimping of collagen fibers increase with growth. First, it can be a natural phenomenon as the fibers grow, they become crimped to endure the applied external force to protect the EHBDs from failure. Studies have verified that the crimping pattern strongly affects the non-linear mechanical behavior of collagenous tissue via experiments and modeling [81,85,200–204]. Specifically, when tensile or cyclic load is applied, the fibers initially start to uncrimp, which is shown in the toe region of the stress-strain curve. Researchers have been able to quantitatively assess the amount of crimping by measuring parameters such as the crimp frequency and angle [81,85,200,201]. Another reason for the fiber crimping increasing with growth could be the cross-linking. There are quantitative methods to

measure the amount of cross-linked fibers using biochemical and nanoscale chromatography [205–207], and researchers have discovered the differentiation of bone cells affected by the collagen cross-linking [206]. For future directions, this chromatographic method could be applied to observe the cross-linking affecting the fiber crimping.

6.4 Conclusion

We applied the 3D collagen fiber analysis on SHG images of mouse EHBD samples cut near liver and gut. 3D parameters measured included *dark*, ϕ , and *SV*. We found these parameters to change with growth (age) gradually. The 3D parameters changing as a function of growth is more pronounced on the cut near gut sample compared to the cut near liver sample. The results suggested that the fibers grow from day 2 until adult, and as they grow the collagenous volume and the amount of 3D crimping increases while the fibers predominantly align along the longitudinal direction.

CHAPTER 7. 3D COLLAGEN FIBER ORGANIZATION ANALYSIS APPLIED ON NON-PREGNANT RAT CERVIX

7.1 Introduction

Cervix is the connective tissue between the uterus and vagina and has canals running throughout its entire length, which serves as the passage for delivery during childbirth [208]. The number of canals varies by animal, where humans have a single canal while rodents have two canals. The ECM of cervix is composed of collagen, glycosaminoglycans (GAGs), elastin, and water [208] where the collagen has a spatially heterogeneous 3D organization. This collagen network dramatically changes in microstructure during pregnancy [209], making the collagen organization not only a spatially but also a temporally heterogeneous structure. Collagen remodels during pregnancy, and in terms of the biomechanical function, the cervix tissue becomes soft [209]. Thus, investigating how the complex 3D collagen structure of cervix is related to stiffness will provide researchers information on the cervix tissue's structure-function relationship. Also, it will provide a guideline of how collagen remodels along different gestational stages, ultimately, leading to developing more accurate modalities to predict spontaneous preterm birth (PTB).

PTB is defined as birth before 37 weeks of gestation, and one out of ten babies born in the United States are diagnosed as PTB [22,208]. It is the second leading cause of infant mortality and the leading cause of infant mortality for African Americans [22]. Current diagnosing tools measure the cervical length macroscopically using clinical ultrasound [210] to predict PTB. However, the accuracy of measuring the cervical length is not high, only being useful for negative predictive value, and cannot be used to predict PTB in the earlier stage of pregnancy [210]. There is evidence that changes in tissue microstructure and function may occur before changing the cervical length

[209] suggesting that rather than macrostructure, microstructural changes will be more sensitive to signify quantitative information.

Ultrasound imaging measures the attenuation of the backscattered signal by the attenuation of the backscattered signal with depth. The attenuation decreases with increasing hydration, and since the hydration percentage changes along pregnancy stages, ultrasound imaging has been used frequently in cervix imaging. McFarlin *et al.* developed a technique referred to quantitative ultrasound (QUS), which uses the mean attenuation of the entire cervix; this provides information on the water content, collagen content and collagen disorganization as a function of gestational age [209,211]. However, ultrasound imaging does not provide 3D structural information of the collagen environment. Thus, researchers have applied optical coherence tomography (OCT) to measure the dispersion of the fiber bundles in 3D [212,213]. OCT images showed pregnant samples having more spatial dispersion than non-pregnant samples, and fibers close to the inner canal showed more dispersion than the fibers on the radial edges. However, the resolution of OCT is in the micrometer range not being able to resolve the collagen fiber microstructure, which makes SHG imaging an appropriate imaging tool providing high resolution both laterally and axially. Mahendroo *et al.* applied SHG imaging during different gestational stages of mouse cervix and was able to conduct quantitative measurements using measures such as the SHG signal intensity, number of pores (circular regions with no SHG signal), and pore fractional area [14]. In addition, researchers have developed endoscopes capable of carrying out SHG imaging and measured parameters such as fiber diameter, fractional area, and mean gray value on different pregnancy stages of mice [214]. A study carried out by Campagnola *et al.* used SHG imaging on human cervix tissue and calculated the fiber alignment using the curvelet transform and the maximum intensity [215]. Lastly, Myers *et al.* characterized the regional difference in the collagen structure

of human cervix using 2D-SHG images [216]. Notwithstanding the significance of these studies, cervix 3D microstructure has not yet been quantitatively assessed and correlated to its mechanical function.

In this study, we analyze non-pregnant rat cervix using quantitative SHG microscopy to characterize its 3D collagen organization in localized regions. We separately measure the localized indentation modulus and relate them to the 3D structural parameters obtained by SHG imaging. Previously, we measured the 3D collagen fiber orientation of cervix and identified the cervical ring surrounding the two canals having an in-plane orientation of collagen fibers where the center region adjacent to the canals has out-of-plane collagen fibers [22]. We expand this analysis by measuring the collagen fiber orientation value and variance in 3D. Using this quantitative approach, we find statistically significant difference on predetermined spatial regions of the cervix cross-section (*ring*, *near-septum*, and *septum*). We also develop a co-registration method to find the indented locations in the SHG image. As a result, we are able to introduce the *opto-mechanogram*, displaying both the structural properties through the SHG image and the mechanical data by nanoindentation.

7.2 Methods

Five 12-week-old non-pregnant rats (Sprague Dawley's) cervixes were harvested and stored in -80°C . For experimentation, the sample was kept at room temperature for 10 minutes before removing additional external tissue. Next, the tissue was embedded with wood blocks by optimal cutting temperature compound. With a cryostat, we cut the cervix 3 mm above the external orifice to generate a smooth surface of the cervix. Subsequently, the tissue was glued on a microscope slide along with the wood blocks to support the sample while imaging.

We used a nanoindenter (Piuma, Optics11) to indent two 25 μm apart parallel lines along the medial-lateral axis of the sample. The indentation lines were composed of points that were 25 μm apart. The sample was submerged in buffer solution during indentation. To co-register the indented regions of cervix with the SHG images that we later obtain, we took multiple bright-field images using the camera on the Piuma nanoindenter and stitched them using the ImageJ mosaic plugin. The final bright-field image included the entire sample and the adjacent two wood blocks, making it possible to locate the indentation lines on the sample. Subsequently, we imaged the sample using the SHG microscope and captured a bright-field image. As similar to the Piuma nanoindenter, we collected multiple bright-field images and stitched them to generate a single image containing the two wood blocks and the sample. This image was matched with the image collected from the nanoindenter, and the indented areas were marked subsequently. Next, we collected SHG images using the SHG microscope on the cervix cross-section, and the indented areas were marked on the SHG image. Finally, we obtained 3D-SHG images in the indented areas. The co-registration process is illustrated in Fig. 7.1(a) and cervix sample used for experiments is in Fig. 7.1(b).

A custom SHG microscope was used for imaging. The sample was illuminated by a Ti:Sapphire laser producing 100-fs duration pulses centered at 780 nm and the SHG signal was collected by a 10X 0.25 NA objective lens. 3D-image stacks were obtained on selected areas with a 60X 1.0 NA water immersion objective lens, and the image stacks have a 350-nm z step size. Volumetric image parameters including *dark*, ϕ , circular variance (*CV*), and *SV* were obtained. The parameter *dark* indicated the non-collagenous volumes of the region of interest and was obtained by the SHG intensity in the image stack. The parameter ϕ represents the angle of the collagen fibers with respect to the x - y image plane where 0° and 90° indicate totally in-plane and out-of-plane, respectively. The *dark* and ϕ parameter were measured by calculating the values on each volume

element ($15 \times 15 \times 15 \mu\text{m}$) and calculating the average of the entire volume ($90 \times 90 \times 30 \mu\text{m}$). Details for calculating the parameters are explained in Chapter 5. CV represents the spread of the θ angles of fibers and SV represents the spread of fiber orientations in 3D, considering both θ and ϕ . Both CV and SV consider the orientations of all the volume elements in the region of interest. The tissue samples were placed in a No. 1.5 cover glass bottom dish (P35G-1.5-20-C, MatTek) with buffer solution to keep the sample hydrated while collecting SHG images.

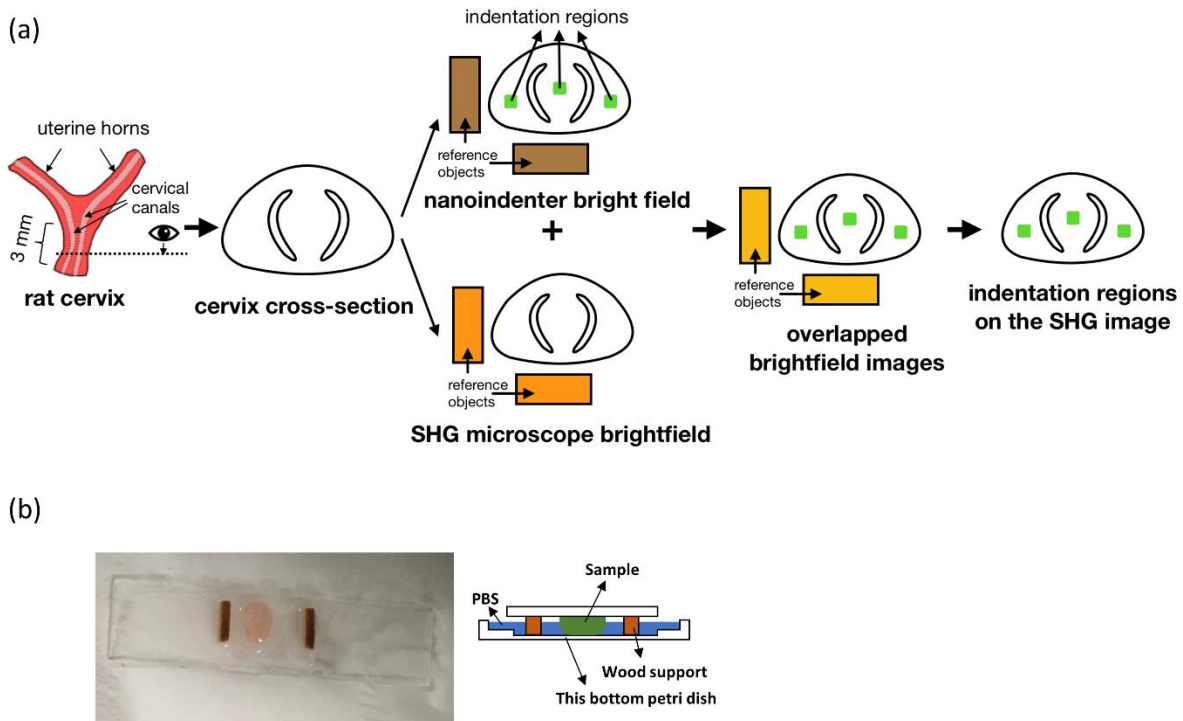


Figure 7.1: (a) Co-registration method for the nanoindenter and SHG microscope. (b) cervix sample and wood blocks prepared for experiments.

For statistical analysis, we used the paired t -test to compare the mean parameters between any two regions (*ring*, *near septum* and *septum*). To estimate the correlation of parameters between regions, we calculated the partial correlation coefficients adjusting for the sample effect.

7.3 Results and discussion

We separate the cervix into three distinct regions based on their structural features on the 2D-SHG image shown in Fig. 7.2(a). The *ring* region is defined as the circumferential region of collagen fibers surrounding the canals and is anisotropic in terms of fiber orientation, which we have previously confirmed using FT-SHG [19]. The *septum* region is located between the two canals and is also identified as anisotropic. The *near septum* region is located between the *septum* and canals and is identified as isotropic, indicating that there is no preferred fiber orientation. Fig. 7.2(b) illustrates the FT-SHG results of the corresponding SHG image in Fig. 7.2(a). The 3D-SHG image analysis is performed for all three regions.

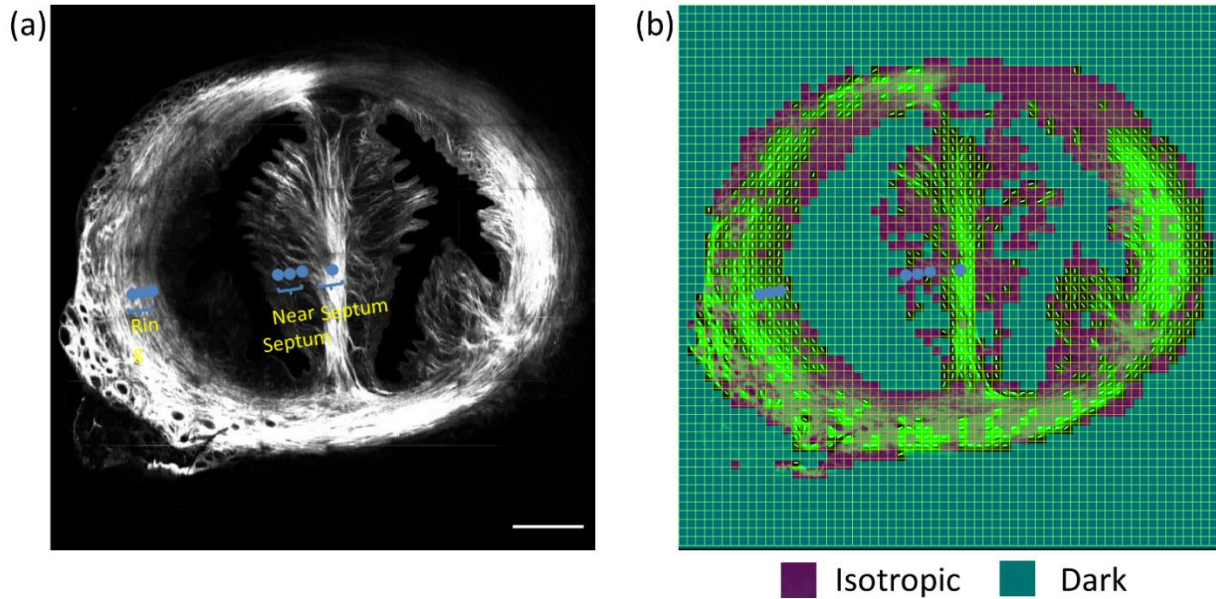


Figure 7.2: (a) 2D-SHG image of the cervix cross-section and (b) the corresponding FT-SHG result on the SHG image. Scale bar is 600 μm .

By overlaying the mechanical data on top of the SHG image at the corresponding locations, we are able to generate an *opto-mechanogram* [Fig. 7.3] showing both the structural properties

through SHG imaging and the mechanical data by nanoindentation. The *opto-mechanogram* demonstrates that the 2D collagen structure is correlated in the *ring*, *near septum* and *septum*, respectively. For further analysis, we analyze the mechanical data and the 3D structural data separately.

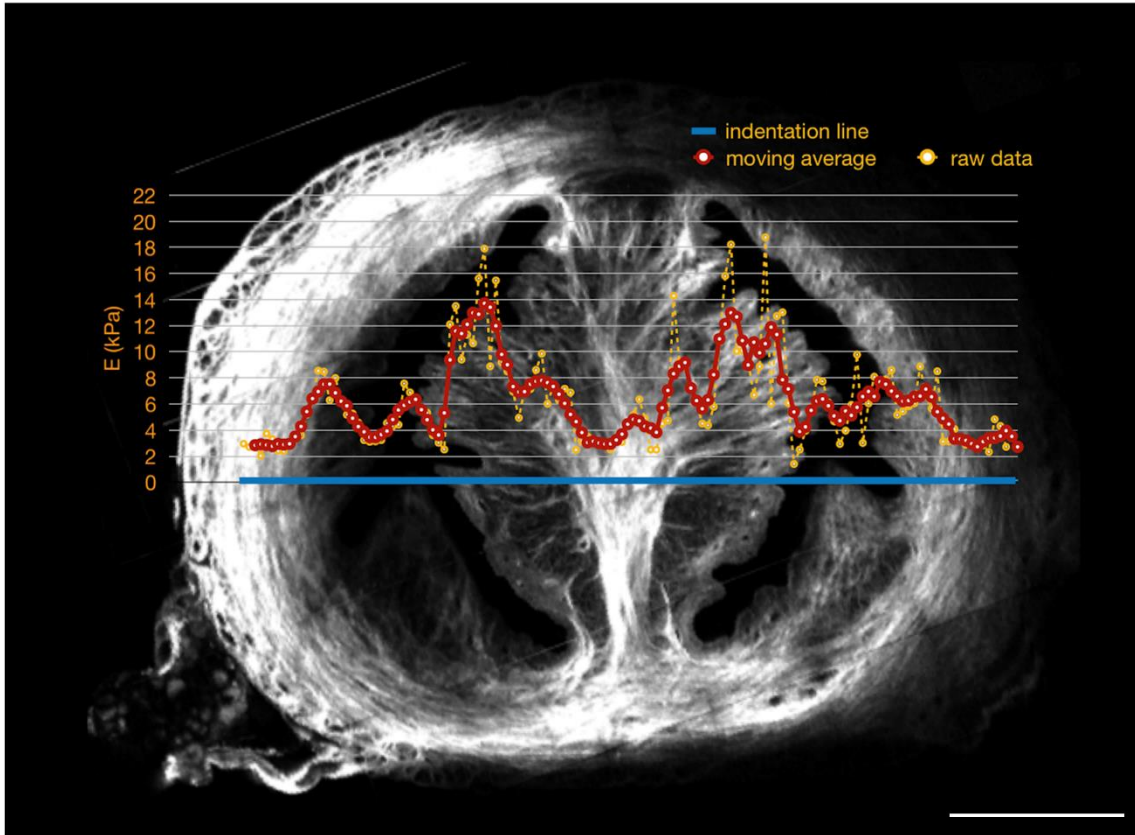


Figure 7.3: Opto-mechanogram. Scale bar is 1 mm

All five samples have a similar range of stiffness, as shown in Fig. 7.4(a), where the right curve on each sample is a curve fit of the data, and the bars on the left are the raw data. The indentation modulus on each region for all five samples are shown in Fig. 7.4(b) as a box plot. The *near septum* has a significantly higher stiffness compared to the *ring* and *near septum* where the *ring* and *septum* have similar stiffness.

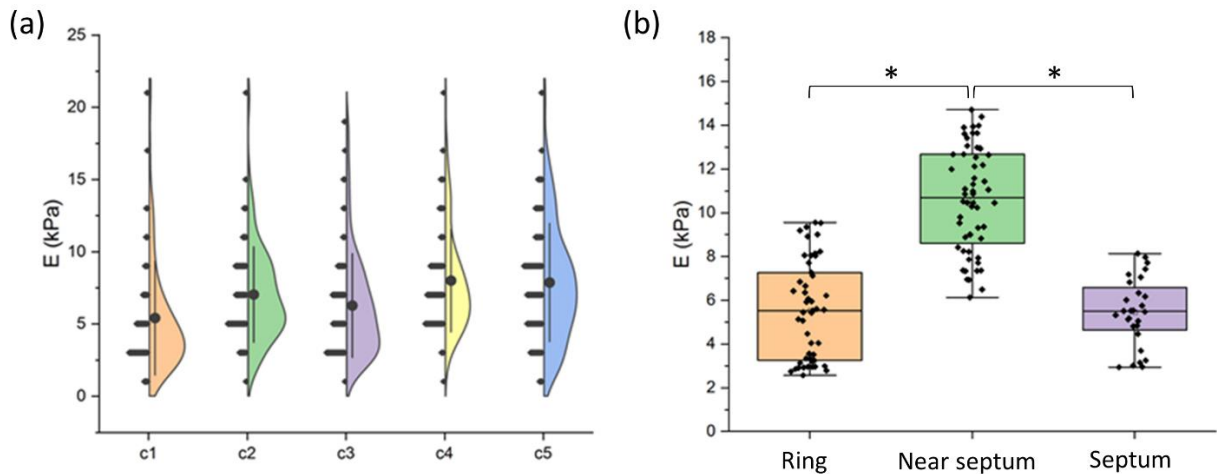


Figure 7.4: (a) Violin plot of the indentation modulus on five cervix tissues and (b) box plot on each spatial region. Asterisk indicates they are significantly different. The image was obtained courtesy of Amir Ostadi Moghaddam from Amy Wagoner Johnsons group.

Figure 7.5 visually shows representative results of the 3D-SHG analysis in the *ring*, *near septum* and *septum* region, respectively. The *ring* region [Fig. 7.5(a)] displays fiber-like structures on the 2D image and have in-plane fibers shown on the 3D rendered image indicated as arrows overlaid on half of the volume. The volume element results in column (iii) indicate that most of the volume elements are anisotropic in terms of fiber orientation. Conversely, the *near septum* region [Fig. 7.5(b)] illustrated on the SHG image does not have a fiber-like structure, and the overall SHG intensity is lower than the *ring* region. The 3D orientation of the fibers in *near septum* [Fig. 7.5(b) column (ii)] are mostly out-of-plane. As opposed to *ring*, *near septum* region has more dark and less anisotropic volume elements. The *septum* region [Fig. 7.5(c)] has similar results with the *ring* region, displaying a fiber-like structure on the 2D-SHG image, demonstrating in-plane fibers on the 3D rendered image, and composed of mainly anisotropic volume elements throughout the volume. The yellow arrows are the 2-directional fibers explained in Chapter 5.

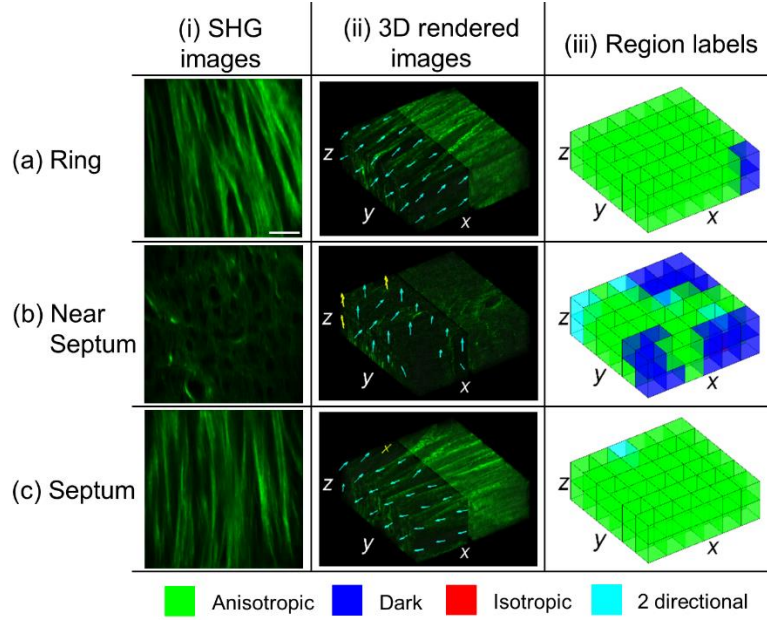


Figure 7.5: Volumetric spatial analysis of 3D-SHG images of the *ring*, *near septum* and *septum* region

Figure 7.6 displays the box plots of the 3D-SHG parameters. In Figure 7.6(a), the average *dark* value for *near septum* region is close to 60%, which is significantly different ($p < 0.05$) with the *ring* and *septum* region. This indicates that the *near septum* region has much less collagen and a higher percentage of other components such as glycosaminoglycans (GAGs). Also, the *near septum* region has a higher ϕ angle compared to the *ring* and *septum* region ($p < 0.05$) shown in Fig. 7.6(b), which is consistent with previous literature [22]. *CV* values also show the same trend in Fig. 6(c), where the *ring* and *near septum* region are significantly different ($p < 0.05$) but the *near septum* and *septum* region are not although having a small p value (0.07). The *SV* value is similar for all three regions, which indicates that the *ring*, *near septum* and *septum* region all have similar 3D fiber orientation spread regardless of their average out-of-plane orientation, ϕ .

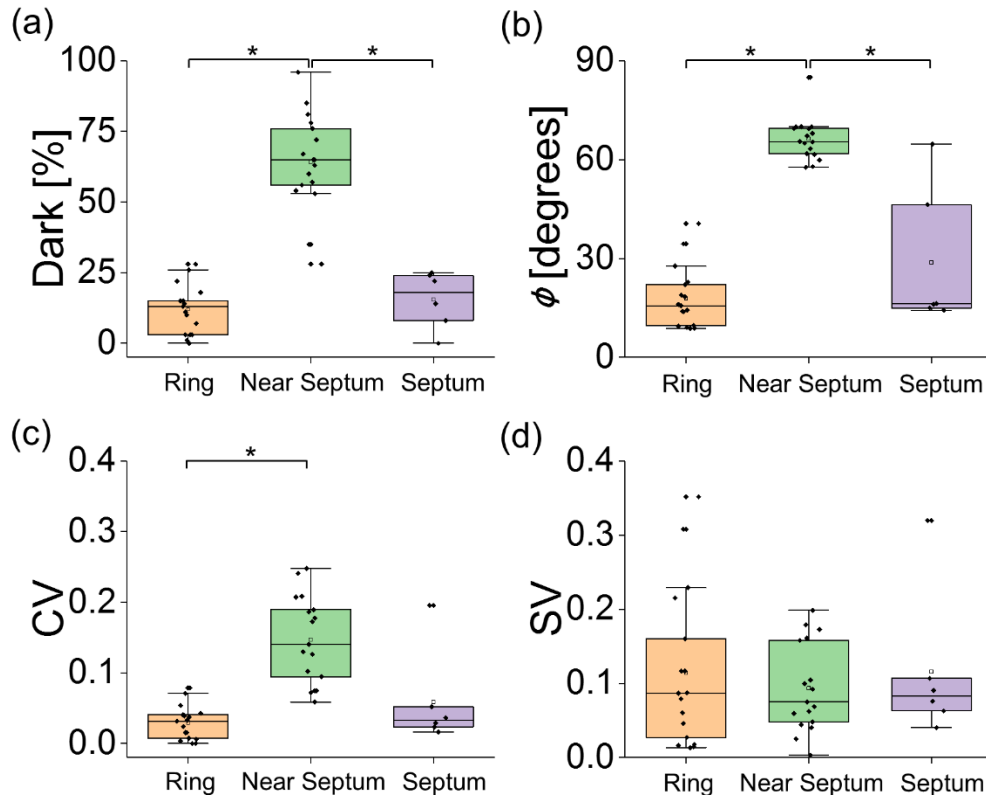


Figure 7.6: 3D-SHG parameter value box plots on each spatial region. Asterisk indicates they are significantly different.

The 3D structural data from SHG imaging and the mechanical data from nanoindentation have a strong correlation, as shown in Fig. 7.7. The indentation modulus has the highest partial correlation coefficient with *dark* (0.922808), followed by ϕ (0.769144) and *CV* (0.728513). This result indicates that the regions which have less collagen content and out-of-plane fibers have a higher stiffness. This could be explained as the interfiber network is strengthening the tissue since the *CV* is higher in *near septum* compared to the other regions, in other words, mean that the collagen fibers are more randomly orientated in the *x-y* plane. In addition, the out-of-plane fiber structure itself could be stronger than the in-plane fiber structure on compression. To test this hypothesis, we implemented the similar nature of the experiment on tendon tissue cut parallel and perpendicular with respect to the fiber bundles and observed the out-of-plane fibers being stiffer

than in-plane fibers. Lastly, the higher percentage of GAGs elements in the *near septum* region could have strengthened the collagen since GAGs act as a collagen organizer [208].

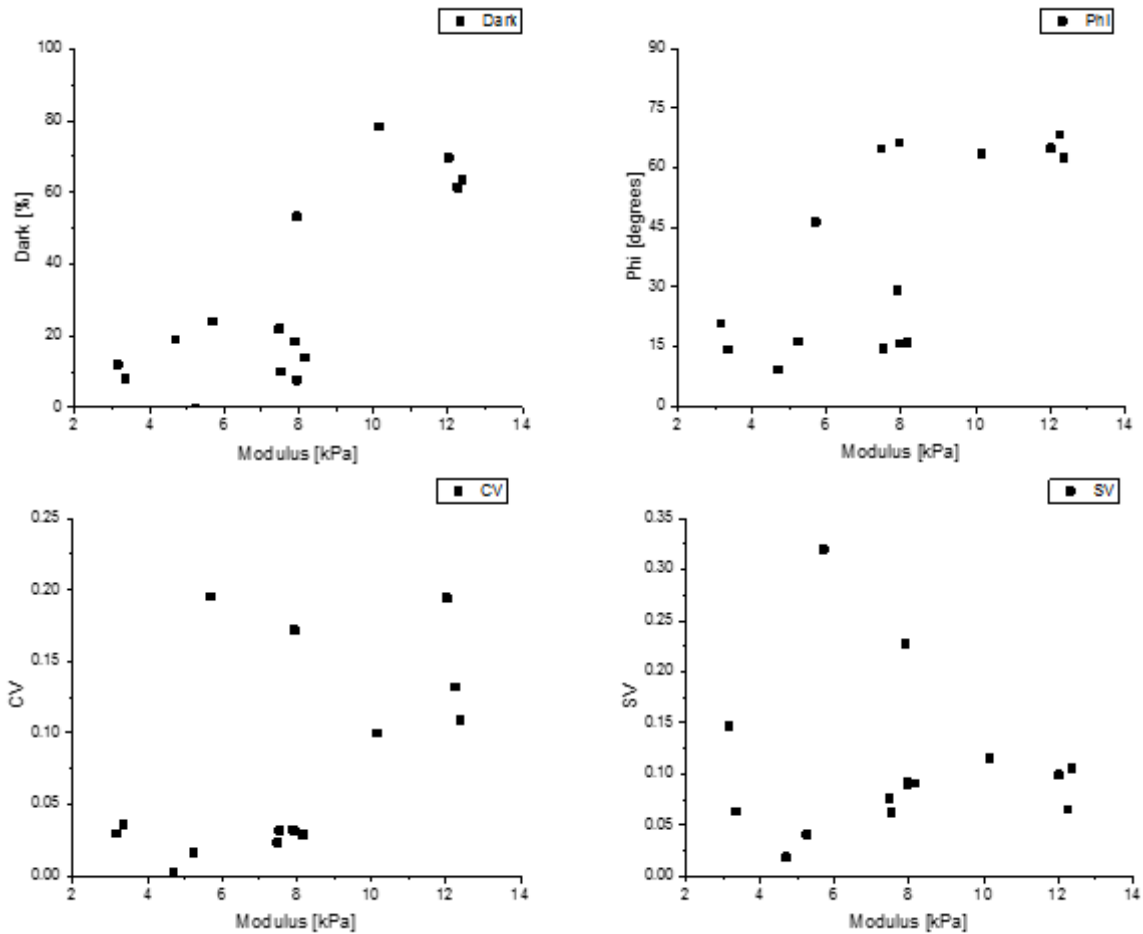


Figure 7.7: Correlation of the 3D-SHG structural parameter data with nanoindentation data.

The comparable properties of *ring* and *septum* region in 3D structure is reasonable since they both serve as the boundary tissue when the pups are delivered and thus undergo similar forms of stress. Collagen is the primary load bearing element [5,6] so the form of stress the tissue endures can strongly affect its structure. The strong correlation of the structure and mechanical function discussed in this study emphasizes the importance of locally measuring the properties of the 3D

structure and function and the significance of co-registering the two methods. Due to the similarity of the *ring* and *septum* region, we can consider the *septum* to be a part of the *ring*, and thus rat cervix could be divided into the circumferential ring and the endocervical tissue which are the key components on human cervix.

There are a few limitations in terms of experiments in this study, which we can further improve. First, there is a co-registration error between the SHG microscope and nanoindenter. The error is measured by using microscope slide-grids (1176A82, Thomas Scientific) and comparing the two bright-field images obtained by the nanoindenter and SHG microscope. The amount of mismatch between the two bright-field images is the error and is $\sim 50 \mu\text{m}$ for a $6 \times 6\text{-mm}$ dimension. This error is primarily generated due to the image stitching, which was conducted manually and can be reduced by using advanced commercialized software. In addition, the 3D-SHG images collected are a maximum three on each region per sample thus, for future experiments, more 3D-SHG images would be needed. Also, the Piuma nanoindenter we implemented on the experiment does not have the ability to measure visco and poro-elasticity of the sample, and these properties would be useful for more in-depth structure-function relationship studies.

7.4 Conclusion

To sum up, we conducted 3D-SHG imaging analysis on three spatially distant regions (*ring*, *near septum*, and *septum*) of non-pregnant rat cervix. We developed a co-registration method and obtained the mechanical properties via nanoindentation on the corresponding regions. There was a significant difference between the *ring*, *septum* versus *near septum* region in 3D structural parameters including *dark*, ϕ , and the indentation modulus. Also, the indentation modulus was strongly correlated with the 3D-SHG image parameters. This work gives an insight of how to

estimate the mechanical properties through the 3D collagen structure quantitatively and helps us to understand the structure-function relationship of collagen. Potentially, this work can lead to establishing more precise methods for diagnosing PTB.

CHAPTER 8. CONCLUSION AND FUTURE WORK

8.1 Summary

This dissertation addressed two methods for quantitative analysis of collagen fiber organization using 3D images obtained by SHG microscopy. The first method was to apply 2D image analysis individually on the images from the 3D-image stack by developing new parameters (metrics) and algorithms. The second method was to apply 3D-image analysis directly to the volumetric image by expanding the parameters in 3D. These quantitative methods were applied on various types of tissues to assess collagen fiber crimp pattern, evaluate fiber damage, quantify fiber growth, and to find potential correlation in 3D collagen organizational structure with intrinsic biomechanical properties.

A quantitative assessment of fiber crimping in ligament tissue was the subject of the initial study. A simple algorithm built based on FT-SHG was implemented to quantitatively distinguish the fiber crimp pattern into three distinct classifications: CAT A, B, and C. CAT A referred to fibers with little or no observed crimp, where CAT B is defined as fiber crimps confined in-plane. Crimps that are out-of-plane were designated as CAT C. The algorithm computed the non-collagen regions and the collagen fiber alignment by measuring the intensity in the spatial domain and the intensity distribution in the spatial-frequency domain, respectively in the 2D images of the 3D stack. This work also revealed the fiber structure variation along the z -axis and the presence of a helical crimp pattern. Fiber crimping strongly affects the mechanical behavior of the tissue; thus, the results of this study could help researchers estimate the mechanical behavior of the tissue without any direct (potentially invasive) mechanical testing.

In another study, quantitative SHG imaging was used to assess the impact of ESEM imaging on collagenous tissues. Tendon tissue samples were prepared under different types of processes (frozen, air-dried, dehydrated, wet, and fixed) and SHG images were collected before and after ESEM imaging. For this study the parameters introduced were density I_d , peak spectral intensity I_s , and ratio r , and were derived from the average SHG intensity and corresponding spatial-frequency analysis. The measurements were applied on the 2D-SHG images throughout the 3D stack. Our results suggested that e-beam irradiation from ESEM induced cross-linking on frozen, air-dried, and dehydrated collagenous fibers as well as structure degradation on wet samples. On the other hand, fixed samples remained unaffected. These structural alterations were quantitatively assessed, where the aforementioned parameters increased for the dehydrated samples and decreased for the wet samples. The higher spatial resolution of ESEM imaging compared to SHG imaging was also confirmed although the specificity to collagen fibers was relatively low. This work provided a guideline on how to prepare samples to minimize sample damage under e-beam irradiation (for ESEM) and also demonstrated how quantitative SHG imaging could be used to evaluate tissue damage.

Finally, the quantitative analysis was extended to three-dimensions to analyze the 3D collagen fiber organization. Initially an algorithm that interprets 3D collagen structure quantitatively was implemented in a manner that is consistent with direct observation. The five classifications of 3D collagen organization (uniform, crimped, random, TFF, and helical) were from natural collagen fiber structures and chosen based on their mechanical properties. From simulated images, the algorithm quantitatively distinguished each classification successfully by computing the 3D fiber orientation and spread. To confirm the analysis, SHG images of tendon tissue were tested and found to be in strong agreement between the results of the classification algorithm and the physical

fiber structure. This 3D fiber analysis was applied to mouse EHBD to assess fiber growth and to non-pregnant rat cervix tissue to find correlations of the 3D collagen structure with biomechanical properties. In EHBD, the 3D parameters applied, $dark$ and ϕ gradually decreased and increased, respectively as a function of fiber growth. This result implied that as fibers grow, the non-collagen volume decreased because the fibers occupied an increased amount of space, while fiber crimping increased, which was verified by the 3D rendered images. In non-pregnant cervix tissue, 3D-SHG analysis was applied to three spatially distinct regions (*ring*, *near septum*, *septum*). The indentation modulus was also acquired from the corresponding regions thanks to a co-registering method we developed. The *ring* and *septum* region were found to be significantly different with the *near septum* both in terms of the 3D structural parameters ($dark$, ϕ) and also with respect to the indentation modulus. The two types of data strongly correlated indicating that the regions with out-of-plane fibers and less collagen content has a higher indentation modulus. The results of this study stressed on the importance of localized quantitative 3D measurements of the structure and co-registering with their mechanical function. Potentially this work can help researchers analyze the collagen remodeling process during pregnancy and eventually help to improve current preterm birth prediction methods through an understanding of structure-function relationship in cervix.

The results of the work carried out in this study was used to generate a catalog of useful quantitative SHG metrics shown as table 8.1. The first column is the collagen features of interest, the next column is the SHG metrics that provides information on the features of interest, and the last column is the types of tissues that have been explored. The usefulness of the metrics is separated as intrinsic and extrinsic.

Table 8.1: Useful quantitative SHG metrics. The bold text indicates the work covered in this thesis.

| | Features of Interest | SHG Based Metrics Explored | Tissue |
|-------------------------|------------------------------|---|---|
| Intrinsic Factor | Collagen density | F/B ratio, Intensity | Artery, Bone, Breast, Cervix, Colon, Kidney, Liver, Ovary, Cervix, Bile duct |
| | Fiber crimping | Crimp patterns, Crimp angle | Ligament |
| | Fiber (fibril) diameter | F/B ratio, Fiber diameter | Cervix, Ovary |
| | Fiber orientation, Alignment | F/B ratio, (3D) Orientation, Spread | Bone, Breast, Colon, Ovary, Skin, Tendon, Bile duct, Cervix |
| | Pores | Pore distance, number, size, (3D) Porosity (<-> collagen fractional area) | Bone, Cervix, Kidney, Liver, Tendon |
| | Proportion of collagen | Intensity ratio | Lung, Skin |
| | χ^2 | Chirality, Ratio of χ^2 component | Breast, Ovary, Skin |
| Extrinsic Factor | Collagen density | Intensity | Cornea, Skin, Tendon |
| | Cross-linking | Peak spectral intensity, Ratio | Tendon |
| | Proportion of collagen | Intensity ratio | Skin |

8.2 Future directions

As a direct extension of the work on rat cervix explained in Chapter 6, we expect to apply the 3D-SHG analysis on different gestational stages of pregnant rat samples. As previously mentioned in Chapter 7, collagen structure in cervix tissue remodels during pregnancy, and it is unknown how the remodeling affects the tissue softening. By using our co-registering method of SHG imaging with nanoindentation, the structure-function relationship will be assessed quantitatively as a function of time. Also, the results can be compared to the recent discoveries of quantitative

ultrasound (QUS). QUS provides measurements of the cervical environment at the macroscale, which was found to have a strong positive correlation between the ultrasound signal attenuation and spontaneous preterm birth [209,211]. By combining 3D-SHG analysis with nanoindentation and QUS, researchers will have better insight on collagen remodeling during pregnancy, and the effects of this remodeling on intrinsic mechanical properties.

In addition, 3D-image analysis can be applied to other imaging modalities such as third-harmonic generation (THG) microscopy. Similar to SHG, THG is a non-linear process where the incident light of a specific wavelength excites the sample and emits light at exactly one-third of the incident wavelength [42]. The advantages of THG imaging include high lateral resolution and optical sectioning capability, which exceeds the performance of SHG microscopy due to the similar nature of the signal generation while having a longer excitation and shorter emission wavelength. Unlike SHG, THG requires structure inhomogeneity of the sample due to the destructive interference of the signal on the focal spot [42]. This makes THG imaging sensitive to interfaces of the sample, making it a more general imaging modality as opposed to SHG microscopy, which is sensitive to only non-centrosymmetric structures like collagen. There are a few studies on THG imaging applied to biological samples [217–219], however the quantitative analysis applied is very limited. Recently, we were able to demonstrate THG imaging of unstained breast tissue biopsies and quantitatively analyze lymphocytes adjacent to tumor cells. Further details of the THG imaging applied on breast tissue is explained in Appendix A.

APPENDIX A. THIRD-HARMONIC GENERATION IMAGING OF BREAST TISSUE BIOPSIES

A.1 Motivation

Breast tissue biopsy has been the gold standard for assessing breast tissue pathology and detecting breast cancer, which is one of the most prevalent diseases among women worldwide and also a major proponent of cancer-related deaths [220]. Typically in this process, breast tissue sections are obtained and prepared for subsequent examination by a pathologist using bright-field microscopy. Due to its optically transparent nature, formalin-fixed, processed and sectioned breast tissue requires exogenous staining for visualization. Even though this provides color contrast to the nucleus, cytoplasm, and surrounding tissue components, tissue staining can affect the integrity of the biological sample, is time-consuming, and creates various artifacts [221]. In this section, we introduce THG imaging as a potential label-free imaging technique to facilitate analysis of breast tumor tissue biopsies.

THG is a third-order non-linear process wherein incident light of a certain frequency is converted to scattered light at exactly three times the incident frequency. The third-harmonic signal is generated from a tightly focused short-pulsed laser beam and is a consequence of the third-order non-linear susceptibility χ^3 of the material. The first demonstration of which was carried out on gasses by New *et al.* [222]. Although all materials exhibit χ^3 , due to the destructive interference of the signal generated upon focusing [42], a structural inhomogeneity is required to produce a non-canceling third-harmonic signal in bulk materials. Similar to SHG, THG is generated only near the focal point, which leads to both high lateral resolution and optical

This work was previously published in W. Lee, M. M. Kabir, R. Emmadi, and K. C. Toussaint, Jr. [61], and is adapted here with permission

sectioning capabilities and facilitates the construction of 3D volumetric images [223]. For THG imaging, long excitation wavelengths can be utilized to increase depth penetration in tissues, while reducing the likelihood of any photodamage. THG imaging on biological structures was first demonstrated on live chara plant rhizoids in 1997 by Squier *et al.* [224]. Subsequent studies [217–219] have used THG to image lipid bodies in hepatocytes, blood vessels, and white-matter structures within the brain simultaneously as well as to identify differences in the granularity of leukocytes *in vivo*. This section introduces backward THG imaging microscopy to image unstained healthy and malignant breast biopsy tissue. In addition, as a comparison, we perform standard PL, phase contrast, and bright-field microscopy imaging on the same samples. Moreover, by applying a simple image analysis technique on the obtained THG images, we report the detection of tumor associated lymphocytes (TLs) in unstained malignant breast tissue sections.

A.2 Methods

A.2.1 Sample preparation

Breast tissue microarray (TMA) samples are purchased (T088bs, US Biomax). These comprise of 24 1.5-mm diameter cores of formalin-fixed, paraffin-embedded breast invasive ductal carcinoma with paired normal breast tissue samples, sectioned at 5- μm thickness and mounted on glass slides. Of the two adjacent TMA sections obtained, one is stained with H&E while the other is left unstained.

A.2.2 Third-harmonic generation microscopy

The experimental setup used for THG microscopy is similar to SHG microscopy. A microscope (IX-81, Olympus) is equipped with a tunable Ti: Sapphire laser source (Mai Tai, Spectra-Physics)

producing 100 fs pulses at a repetition rate of 80 MHz. The input beam has a wavelength of 945 nm and is reflected by a 680 nm short-pass dichroic beam splitter (FF670-SDi01, Semrock) onto the back aperture of an Olympus Plan N 40X 0.65 NA objective lens (PLAN N, Olympus). The same objective is used to focus the beam onto the sample and also collect the backward THG signal emitted from the sample. The input laser beam is focused on the interface between air and breast tissue to maximize the refractive index interface of the sample [218]. The output signal is filtered with a 680 nm short-pass laser blocking filter and a 315 nm band-pass THG filter (FF01-315/15-25, Semrock). A photomultiplier tube (H10721-110, Hamamatsu) records the THG signal, and an 8-bit image of $115 \times 115 \mu\text{m}$ is constructed with a pixel size of 580 nm. For all samples, the average power of the laser at the sample is $\sim 15 \text{ mW}$.

To image an entire tissue core, customized codes in Labview and MATLAB are used to tile and stitch together individual images. Approximately 200 individual images are needed to construct a complete core. In order to mitigate and remove the unwanted contribution of noise, we use a threshold above a predetermined noise floor.

A.2.3 Image analysis

A simple algorithm is developed to identify TLs in THG images of breast tissue. Briefly, TLs are approximated as spherical particles [225] with a core of high density of chromatin [226]. In addition, the intensity profile across its 2D cross-section is assumed to provide a Gaussian profile. Based on these two assumptions, a sample Gaussian profile is constructed by analyzing lymphocytes that have been marked by a pathologist in H&E images and compared to lymphocyte candidates in THG images to detect TLs.

A.3 Results and discussion

We apply THG microscopy to image unstained healthy and malignant breast tissue cores. To compare the contrast of THG microscopy on such samples to conventional imaging approaches used by researchers, images of these same structures are obtained using PL and phase contrast microscopy; the neighboring stained cores are imaged with bright-field microscopy. Figure A.1 summarizes the results, where A.1(a) are images of healthy breast tissue, and A.1(b) shows malignant tissue. To identify the internal structures, a smaller $125 \times 100 \mu\text{m}$ region is magnified for each image and shown in Figs. A.1(a) and (b) panels (v)-(viii). From Fig. A.1(a), (b), (i-iv), it is observed that THG provides a similar contrast for both healthy and malignant tissue when compared to PL microscopy and has a higher contrast when compared to phase contrast images. It is observed that a ‘halo effect’ [96,227], which is an artifact of the imaging technique, takes place on the boundaries surrounding different morphological features in the phase contrast images. Furthermore, unlike PL and phase contrast microscopy, THG is a non-linear three-photon imaging technique that can circumvent the restrictions of the Abbe limit [3]. As such THG exhibits a higher resolution than the other two methods. For the malignant breast tissue core in Fig. A.1(b) tumor nuclei and lymphocytes become apparent while the amount of stroma compared to normal tissue reduces significantly. The average THG intensity from malignant breast tissue is found to be almost two times larger than that obtained from the normal tissue.

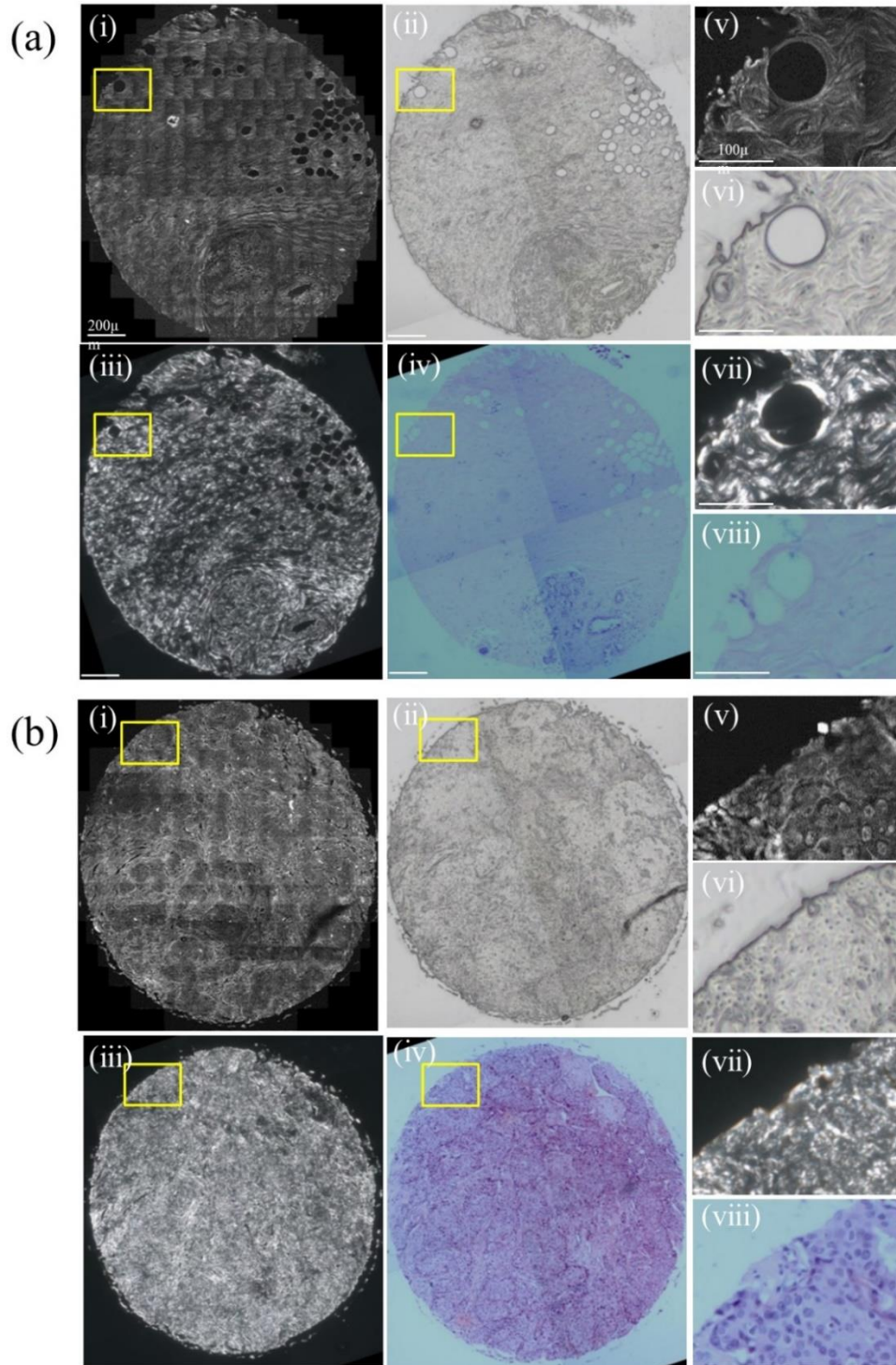


Figure A.1: Images of (a) normal and (b) grade three malignant unstained breast tissue using (i) THG microscopy, (ii) phase contrast microscopy and (iii) PL microscopy. (iv) A bright-field, H&E stained image of an adjacent section used in (i)-(iii). (v)-(viii) are zoomed-in to selected regions (yellow boxes) of (i)-(iv), respectively. Adapted from [61].

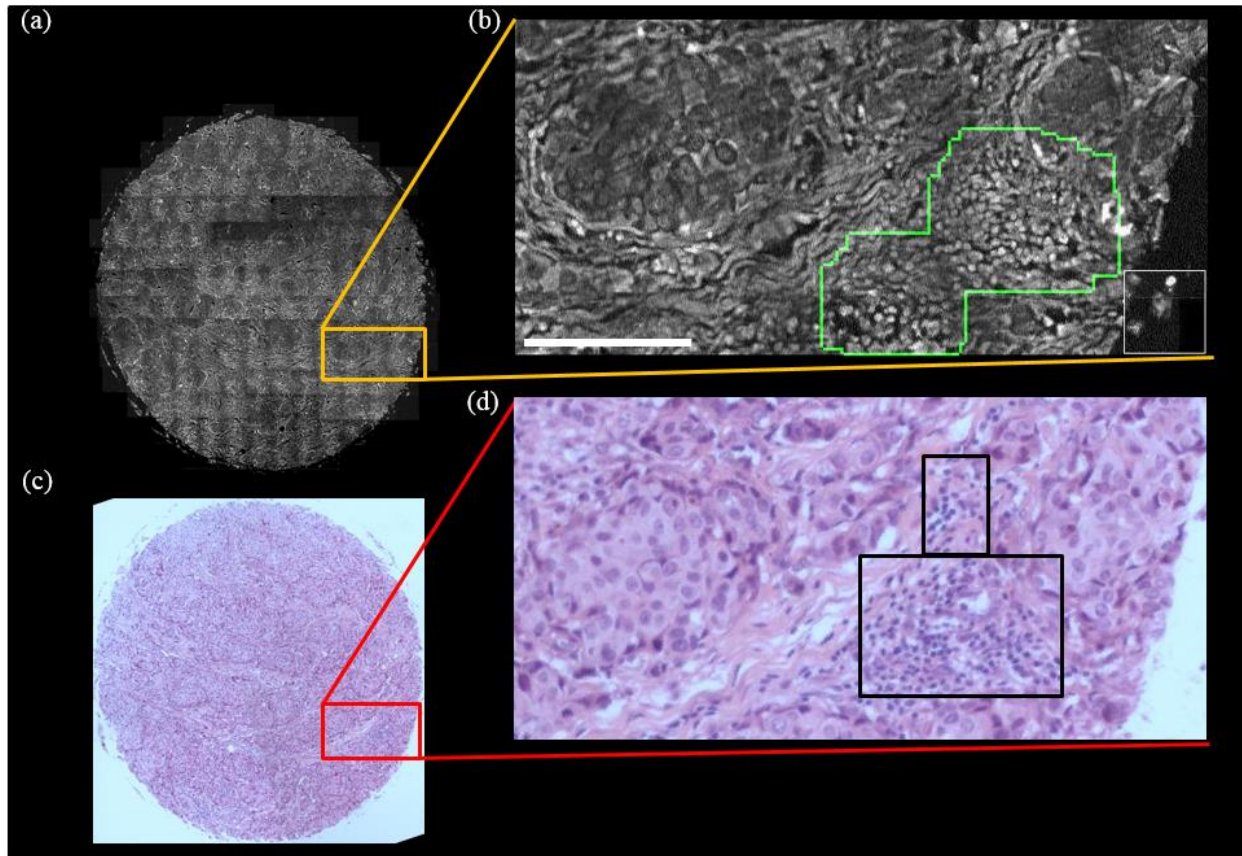


Figure A.2: Results of lymphocyte detection in a selected region of a malignant core. (a) THG image of a breast tissue core, out of which a $\sim 650 \times 300$ pixels region is chosen for analysis, as shown in (b). The region is scanned from the top left to the bottom right, with a window of 80×80 pixels shown by the white box. The lymphocyte-rich regions are marked in green. Lymphocytes detected by the pathologist on the (c) H&E stained slice is marked as the (d) black box. Scale bar is $100 \mu\text{m}$. Adapted from [61].

By using the information summarized in Fig. A.1, we focus on identifying structures within the breast tissue, such as TLs. To demonstrate the capability of the algorithm, a $\sim 650 \times 300$ -pixel region is scanned by an 80×80 -pixel scanning window to detect the ‘lymphocyte-rich regions’ as shown in Fig. A.2. If the number of detected lymphocytes within the scanning window exceed a predetermined threshold, they are considered as ‘lymphocyte-rich regions’. This procedure is applied to part of a malignant breast tissue core [Fig. A.2(a)] and the results are shown in Fig. A.2(b). The detected lymphocyte-rich region is marked with a green boundary. Further, to compare

the accuracy of the analysis technique, the results are compared to the lymphocyte-rich region marked by a pathologist on the adjacent H&E stained breast tissue core [Fig. A.2(c)], the results of which are shown in Fig. A.2(d).

We find that the THG intensity profile from lymphocytes is that of a Gaussian distribution. The reason for this could be explained by the refractive index inhomogeneity. THG comes from an interface in the refractive index or susceptibility [228]. Thus the focal point of the objective is placed on the surface between air and the tissue for maximum signal. The nucleus of a lymphocyte is composed of uniform, compact chromatin [3]. Due to a relatively higher refractive index of chromatin ($n=1.39-1.45$) [229], the THG signal emanating from the lymphocyte-air boundary reaches the highest value at the center and decreases towards the edge of a lymphocyte. As the size of the lymphocyte-air interface is in the micrometer scale, the signal is appreciable.

We apply our algorithm to the entire core of malignant breast tissue to identify lymphocyte-rich regions. These regions are then compared to those identified by a pathologist on a neighboring H&E stained core, and the percentage of area overlap between both results are displayed as shown in Fig. A.3. The same procedure is repeated for three complete malignant cores on the TMA, and the average area of overlap is calculated. 62% of the area identified by the pathologist on a corresponding stained breast biopsy core matches with the area identified by our algorithm.

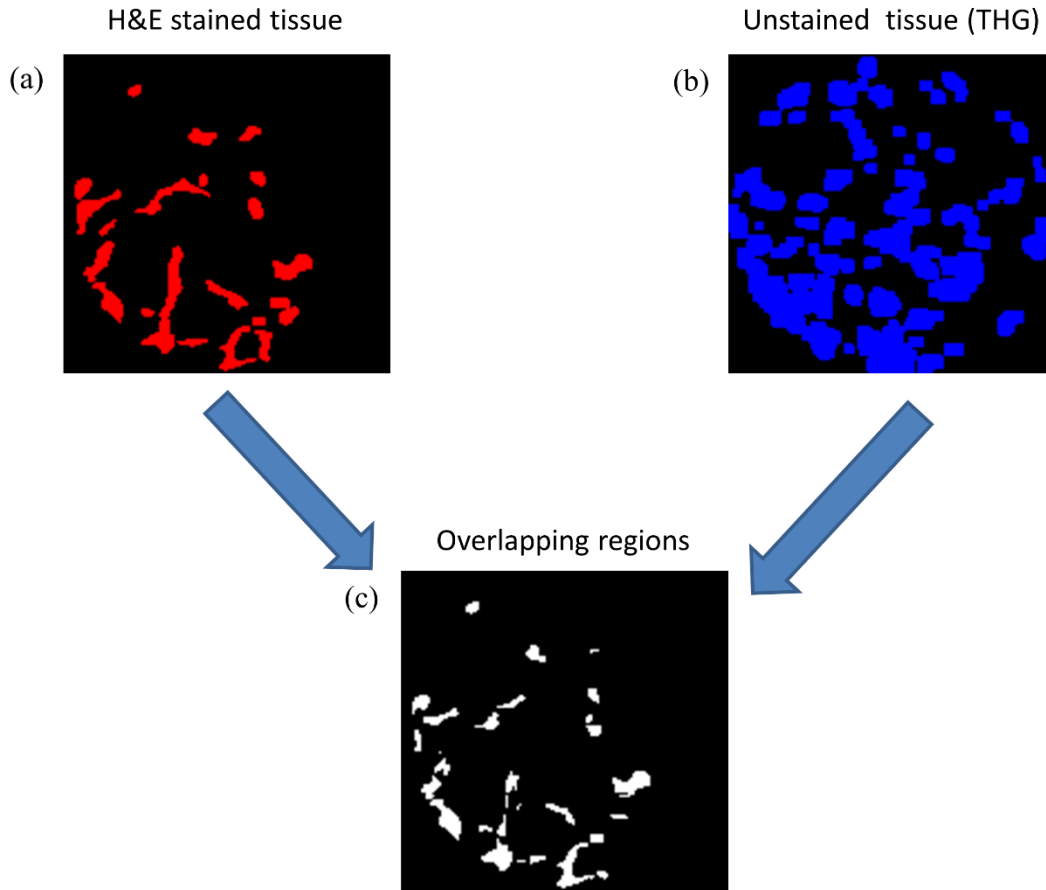


Figure A.3: Lymphocyte rich region comparison. (a) Lymphocyte rich regions identified by a Pathologist on the H&E stained tissue and (b) lymphocyte rich regions detected by the algorithm on unstained THG images. (c) The results of the two analyses are superimposed, and the overlapped areas are shown. Adapted from [61].

From the results obtained in our analysis, we identify a few factors to account for the discrepancy with the pathologist's observation (Fig. A.3(a)). In the algorithm developed in this work, a lymphocyte is approximated as a spherical particle having a 2D Gaussian intensity profile across its cross-section. This means that any lymphocyte that is not spherical in shape or smaller than the assumed diameter would possibly not be picked up by the algorithm. The algorithm also ignores lymphocytes that are clustered together due to the difficulty in obtaining individual intensity profiles across their cross-sections.

A.4 Conclusion

In this section, we demonstrated THG imaging of a breast TMA containing unstained normal and malignant tissues. We showed that compared to conventional imaging methods such as PL and phase contrast microscopy, THG images provided high contrast with respect to phase contrast microscopy and avoided the imaging artifacts prevalent in PL microscopy, which impede resolving finer structures in the tissue. In addition, we developed a simple algorithm to quantitatively detect TLs and identified lymphocyte rich regions in breast tissue. More than 60% of the lymphocyte rich region detected by the pathologist overlapped with the regions identified by our analysis. This study highlights the potential of THG imaging as a label-free modality for analyzing breast tissue biopsies.

REFERENCES

- [1] P. A. Franken, A. E. Hill, C. W. Peters, and G. Weinreich, "Generation of optical harmonics," *Phys. Rev. Lett.* **7**, 118–119 (1961).
- [2] B. Masters and P. So, *Handbook of Biomedical Nonlinear Optical Microscopy* (Oxford University Press, 2008).
- [3] F. S. Pavone and P. J. Campagnola, *Second Harmonic Generation Imaging* (CRC Press, 2016).
- [4] G. A. Di Lullo, S. M. Sweeney, J. Korkko, L. Ala-Kokko, and J. D. San Antonio, "Mapping the ligand-binding sites and disease-associated mutations on the most abundant protein in the human, type I collagen," *J. Biol. Chem.* **277**, 4223–4231 (2002).
- [5] R. Ambekar, M. Chittenden, I. Jasiuk, and K. C. Toussaint, "Quantitative second-harmonic generation microscopy for imaging porcine cortical bone: Comparison to SEM and its potential to investigate age-related changes," *Bone* **50**, 643–650 (2012).
- [6] A. Gosain and L. A. DiPietro, "Aging and wound healing," *World J. Surg.* **28**, 321–326 (2004).
- [7] F. Aptel, N. Olivier, A. Deniset-Besseau, J. M. Legeais, K. Plamann, M. C. Schanne-Klein, and E. Beaurepaire, "Multimodal nonlinear imaging of the human cornea," *Investig. Ophthalmol. Vis. Sci.* **51**, 2459–2465 (2010).
- [8] M. Han, G. Giese, and J. Bille, "Second harmonic generation imaging of collagen fibrils in cornea and sclera," *Opt. Express* **13**, 1–7 (2005).
- [9] K. Schenke-Layland, I. Riemann, O. Damour, U. A. Stock, and K. König, "Two-photon microscopes and in vivo multiphoton tomographs - Powerful diagnostic tools for tissue engineering and drug delivery," *Adv. Drug Deliv. Rev.* **58**, 878–896 (2006).
- [10] O. Nadiarnykh, R. LaComb, M. Brewer, and P. Campagnola, "Alterations of the extracellular matrix in ovarian cancer studied by second harmonic generation imaging microscopy," *BMC Cancer* **10**, 94 (2010).
- [11] O. Nadiarnykh, S. Plotnikov, W. A. Mohler, I. Kalajzic, D. Redford-Badwal, and P. J. Campagnola, "Second harmonic generation imaging microscopy studies of osteogenesis imperfecta," *J. Biomed. Opt.* **12**, 51805 (2007).
- [12] K. Tilbury, J. Hocker, B. L. Wen, N. Sandbo, V. Singh, and P. J. Campagnola, "Second harmonic generation microscopy analysis of extracellular matrix changes in human idiopathic pulmonary fibrosis," *J. Biomed. Opt.* **19**, 086014 (2014).
- [13] S.-J. Lin, R.-J. Wu, H.-Y. Tan, W. Lo, W.-C. Lin, T.-H. Young, C.-J. Hsu, J.-S. Chen, S.-H. Jee, et al., "Evaluating cutaneous photoaging by use of multiphoton fluorescence and second-harmonic generation microscopy," *Opt. Lett.* **30**, 2275–2277 (2005).
- [14] M. L. Akins, K. Luby-Phelps, and M. Mahendroo, "Second harmonic generation imaging as a potential tool for staging pregnancy and predicting preterm birth," *J. Biomed. Opt.* **15**, 026020 (2010).
- [15] K. Eliceiri, M. Conklin, J. Bredfeldt, T. Mackie, Y. Liu, and P. Keely, "Automated quantification of aligned collagen for human breast carcinoma prognosis," *J. Pathol. Inform.* **5**, 28 (2014).
- [16] M. Strupler, A. Pena, M. Hernest, P. Tharaux, J. Martin, E. Beaurepaire, and M. Schanne-Klein, "Second harmonic imaging and scoring of collagen in fibrotic tissues," *Opt. Express*

- 15**, 4054–4065 (2007).
- [17] R. Akhtar, M. J. Sherratt, J. K. Cruickshank, and B. Derby, “Characterizing the elastic properties of tissues,” *Eur. PMC Funders Gr.* **14**, 96–105 (2011).
- [18] N. Ozkaya, D. Leger, D. Goldsheyder, and M. Nordin, “Mechanical properties of biological tissues,” in *Fundam. Biomech. Equilibrium, Motion, Deform.* (Springer, 2016).
- [19] M. Sivaguru, S. Durgam, R. Ambekar, D. Luedtke, G. Fried, A. Stewart, and K. C. Toussaint, “Quantitative analysis of collagen fiber organization in injured tendons using Fourier transform-second harmonic generation imaging,” *Opt. Express* **18**, 24983–24993 (2010).
- [20] R. Ambekar, T. Y. Lau, M. Walsh, R. Bhargava, and K. C. J. Toussaint, “Quantifying collagen structure in breast biopsies using second-harmonic generation imaging,” *Biomed. Opt. Express* **3**, 2021–2035 (2012).
- [21] T. Y. Lau, R. Ambekar, and K. C. Toussaint, Jr., “Quantification of collagen fiber organization using three-dimensional Fourier transform-second-harmonic generation imaging,” *Opt Express* **20**, 21821–21832 (2012).
- [22] T. Y. Lau, H. K. Sangha, E. K. Chien, B. L. Mcfarlin, A. J. Wagoner Johnson, and K. C. Toussaint, “Application of Fourier transform-second-harmonic generation imaging to the rat cervix,” *J. Microsc.* **251**, 77–83 (2013).
- [23] W. Lee, H. Rahman, M. E. Kersh, and K. C. Toussaint, Jr., “Application of quantitative second-harmonic generation microscopy to posterior cruciate ligament for crimp analysis studies,” *J Biomed Opt* **22**, 046009 (2017).
- [24] W. Lee and K. C. Toussaint, Jr., “Quantitative analysis of the effect of environmental-scanning electron microscopy on collagenous tissues,” *Sci. Rep.* **8** (2018).
- [25] G. N. Ramachandran, “Structure of collagen,” *Nature* **174**, 269–270 (1954).
- [26] A. V Persikov, J. A. Ramshaw, A. Kirkpatrick, and B. Brodsky, “Amino acid propensities for the collagen triple-helix,” *Biochemistry* **39**, 14960–14967 (2000).
- [27] G. N. Ramachandran, “Molecular structure of collagen,” in *International Review of Connective Tissue Research* (Elsevier, 1963).
- [28] E. J. Miller and S. Gay, “The collagens: An overview and update,” *Methods Enzymol.* **144**, 3–41 (1987).
- [29] “The collagen molecule,” *Proto-col*, 2014, <<https://www.protocol.com/blog/2014/07/30/collagen/>>.
- [30] P. Fratzl, *Collagen: Structure and Mechanics* (Springer US, 2008).
- [31] K. Gelse, E. Po, and T. Aigner, “Collagens — structure , function , and biosynthesis,” *Adv. Drug Deliv. Rev.* **55**, 1531–1546 (2003).
- [32] Y. Nishimori, C. Edwards, A. Pearse, K. Matsumoto, M. Kawai, and R. Marks, “Degenerative alterations of dermal collagen fiber bundles in photodamaged human skin and uv-irradiated hairless mouse skin: Possible effect on decreasing skin mechanical properties and appearance of wrinkles,” *J. Invest. Dermatol.* **117**, 1458–1463 (2001).
- [33] W. F. Vogel, “Collagen-receptor signaling in health and disease,” *Eur. J. Dermatol.* **11**, 506–514 (2001).
- [34] P. Balasubramanian, M. P. Prabhakaran, M. Sireesha, and S. Ramakrishna, “Collagen in human tissues: Structure, function, and biomedical implications from a tissue engineering perspective,” in *Polym. Compos - Polyolefin Fractionation - Polym. Pept. - Collagens*, (Springer Berlin Heidelberg, 2013).
- [35] L. J. Martin and N. F. Boyd, “Mammographic density. Potential mechanisms of breast

- cancer risk associated with mammographic density: Hypotheses based on epidemiological evidence,” *Breast Cancer Res.* **10**, 201 (2008).
- [36] W. Han, S. Chen, W. Yuan, Q. Fan, J. Tian, X. Wang, L. Chen, X. Zhang, W. Wei, et al., “Oriented collagen fibers direct tumor cell intravasation,” *PNAS.* **113**, 11208–11213 (2016).
- [37] S. L. Schor, “Cell proliferation and migration on collagen substrata in vitro,” *J. Cell Sci.* **41**, 159 LP-175 (1980).
- [38] F. Rauch and F. H. Glorieux, “Osteogenesis imperfecta,” *Lancet (London, England)* **363**, 1377–1385 (2004).
- [39] R. Ambekar, K. C. J. Toussaint, and A. Wagoner Johnson, “The effect of keratoconus on the structural, mechanical, and optical properties of the cornea,” *J. Mech. Behav. Biomed. Mater.* **4**, 223–236 (2011).
- [40] T. T. Andreassen, A. H. Simonsen, and H. Oxlund, “Biomechanical properties of keratoconus and normal corneas,” *Exp. Eye Res.* **31**, 435–441 (1980).
- [41] S. Bretaud, P. Nauroy, M. Malbouyres, and F. Ruggiero, “Fishing for collagen function: About development, regeneration and disease,” *Semin. Cell Dev. Biol.* **89**, 100–108 (2019).
- [42] R. W. Boyd and D. Prato, *Nonlinear Optics* (Elsevier Science, 2008).
- [43] D. J. Prockop and A. Fertala, “The collagen fibril: The almost crystalline structure,” *J. Struct. Biol.* **122**, 111–118 (1998).
- [44] B.-M. Kim, J. Eichler, and L. B. Da Silva, “Frequency doubling of ultrashort laser pulses in biological tissues,” *Appl. Opt.* **38**, 7145–7150 (1999).
- [45] R. M. Williams, W. R. Zipfel, and W. W. Webb, “Interpreting second-harmonic generation images of collagen I fibrils,” *Biophys J* **88**, 1377–1386 (2005).
- [46] M. Rivard, C. Couture, A. K. Miri, M. Laliberté, A. Bertrand-Grenier, L. Mongeau, and F. Légaré, “Imaging the bipolarity of myosin filaments with interferometric second harmonic generation microscopy,” *Biomed. Opt Express* **4**, 2078–2086 (2013).
- [47] W. H. Stoothoff, B. J. Bacskai, and B. T. Hyman, “Monitoring Tau-Tubulin interactions utilizing second harmonic generation in living neurons,” *J Biomed Opt* **13**, 064039 (2008).
- [48] D. J. Hulmes and A. Miller, “Quasi-hexagonal molecular packing in collagen fibrils,” *Nature* **282**, 878–880 (1979).
- [49] R. Z. Kramer, L. Vitagliano, J. Bella, R. Berisio, L. Mazzarella, B. Brodsky, A. Zagari, and H. M. Berman, “X-ray crystallographic determination of a collagen-like peptide with the repeating sequence (Pro-Pro-Gly),” *J. Mol. Biol.* **280**, 623–638 (1998).
- [50] S. Roth and I. Freund, “Second harmonic generation in collagen,” *J. Chem. Phys.* **70**, 1637–1643 (1979).
- [51] J. Mertz and L. Moreaux, “Second-harmonic generation by focused excitation of inhomogeneously distributed scatterers,” *Opt. Commun.* **196**, 325–330 (2001).
- [52] M. Sivaguru, M. M. Kabir, M. R. Gartia, D. S. C. Biggs, B. S. Sivaguru, V. A. Sivaguru, G. A. Fried, G. L. Liu, S. Sadayappan, et al., “Application of an advanced maximum likelihood estimation restoration method for enhanced-resolution and contrast in second-harmonic generation microscopy,” *J. Microsc.* **267**, 397–408 (2017).
- [53] C. M. Hsueh, W. Lo, W. L. Chen, V. A. Hovhannisyanyan, G. Y. Liu, S. S. Wang, H. Y. Tan, and C. Y. Dong, “Structural characterization of edematous corneas by forward and backward second harmonic generation imaging,” *Biophys. J.* **97**, 1198–1205 (2009).
- [54] C. Y. Park, J. K. Lee, and R. S. Chuck, “Second harmonic generation imaging analysis of collagen arrangement in human cornea,” *Investig. Ophthalmol. Vis. Sci.* **56**, 5622–5629

- (2015).
- [55] B. Weigelin, G.-J. Bakker, and P. Friedl, “Intravital third harmonic generation microscopy of collective melanoma cell invasion,” *IntraVital* **1**, 32–43 (2012).
 - [56] R. A. R. Rao, M. R. Mehta, S. Leithem, and K. C. Toussaint, “Quantitative analysis of forward and backward second-harmonic images of collagen fibers using Fourier transform second-harmonic-generation microscopy,” *Opt. Lett.* **34**, 3779–3781 (2009).
 - [57] F. Légaré, C. Pfeffer, and B. R. Olsen, “The role of backscattering in SHG tissue imaging,” *Biophys. J.* **93**, 1312–1320 (2007).
 - [58] X. Han and E. Brown, “Measurement of the ratio of forward-propagating to back-propagating second harmonic signal using a single objective,” *Opt Express* **18**, 10538–10550 (2010).
 - [59] W. R. Zipfel, R. M. Williams, and W. W. Webb, “Nonlinear magic: Multiphoton microscopy in the biosciences,” *Nat. Biotechnol.* **21**, 1369–1377 (2003).
 - [60] J. Pawley, *Handbook of Biological Confocal Microscopy* (Springer US, 2013).
 - [61] W. Lee, M. M. Kabir, R. Emmadi, and K. C. Toussaint, Jr., “Third-harmonic generation imaging of breast tissue biopsies,” *J Microsc* **264**, 175–181 (2016).
 - [62] C. Manning, M. J. Morgan, C. T. W. Allen, and E. Pellicano, “Susceptibility to Ebbinghaus and Müller-Lyer illusions in autistic children: A comparison of three different methods,” *Mol. Autism* **8**, 16 (2017).
 - [63] DK Publishing Inc, *Optical Illusions* (DK Publishing, 2012).
 - [64] R. LaComb, O. Nadiarnykh, and P. J. Campagnola, “Quantitative second harmonic generation imaging of the diseased state osteogenesis imperfecta: Experiment and simulation,” *Biophys. J.* **94**, 4504–4514 (2008).
 - [65] S. Puschmann, C.-D. Rahn, H. Wenck, S. Gallinat, and F. Fischer, “Approach to quantify human dermal skin aging using multiphoton laser scanning microscopy,” *J. Biomed. Opt.* **17**, 036005 (2012).
 - [66] P. P. Provenzano, K. W. Eliceiri, J. M. Campbell, D. R. Inman, J. G. White, and P. J. Keely, “Collagen reorganization at the tumor-stromal interface facilitates local invasion,” *BMC Med.* **4**, 1–15 (2006).f
 - [67] H. M. Shieh, C.-H. Chung, and C. L. Byrne, “Resolution enhancement in computerized tomographic imaging,” *Appl. Opt.* **47**, 4116–4120 (2008).
 - [68] H. G. Adelman, “Butterworth equations for homomorphic filtering of images,” *Comput. Biol. Med.* **28**, 169–181 (1998).
 - [69] J. W. Goodman, *Introduction to Fourier Optics* (W. H. Freeman, 2005).
 - [70] B. E. A. Saleh and M. C. Teich, *Fundamentals of Photonics* (Wiley, 2019).
 - [71] N. Pears, Y. Liu, and P. Bunting, *3D Imaging, Analysis and Applications* (Springer London, 2012).
 - [72] C. Macias-Romero, C. Teulon, M. Didier, and S. Roke, “Endogenous SHG and 2PEF coherence imaging of substructures in neurons in 3D,” *Opt. Express* **27**, 2235–2247 (2019).
 - [73] L. F. Ochoa, A. Kholodnykh, P. Villarreal, B. Tian, R. Pal, A. N. Freiberg, A. R. Brasier, M. Motamedi, and G. Vargas, “Imaging of murine whole lung fibrosis by large scale 3D microscopy aided by tissue optical clearing,” *Sci. Rep.* **8**, 13348 (2018).
 - [74] J. Dvorak, E. Schneider, P. Saldinger, and B. Rahn, “Biomechanics of the craniocervical region: The alar and transverse ligaments,” *J. Orthop. Res.* **6**, 452–461 (1988).
 - [75] J. Goodfellow and J. O’Connor, “The mechanics of the knee and prosthesis design,” *J. Bone*

- Jt. Surg.* **60–B**, 358–369 (1978).
- [76] U. Meyer, T. Meyer, J. Handschel, and H. Wiesmann, *Fundamentals of Tissue Engineering and Regenerative Medicine* (Springer Science & Business Media, 2009).
- [77] L. Yahia, *Ligament and Ligamentoplasties* (Springer Science & Business Media, 2012).
- [78] F. Noyes, D. Butler, E. Grood, and M. Hefzy, “Biomechanical analysis of human ligament grafts used in knee-ligament repairs and reconstructions,” *J. Bone Jt. Surg.* **66**, 344–352 (1984).
- [79] M. Yamamoto, Sota. Saito, Akinori. Nagasaka, Kei. Sugimoto, Satoshi. Mizuno, Koji. Tanaka, Eiichi. Kabayama, “The strain-rate dependence of mechanical properties of rabbit knee ligament,” in *Int. Tech. Conf. Enhanc. Saf. Veh.*, (2003).
- [80] J. Diamant, A. Keller, E. Baer, and M. Litt, “Collagen; ultrastructure and its relations to mechanical properties as a function of ageing,” *Proc. R. Soc. London, Ser. B* **180**, 293–315 (1972).
- [81] K. A. Hansen, J. A. Weiss, and J. K. Barton, “Recruitment of tendon crimp with applied tensile strain,” *J. Biomech. Eng.* **124**, 72–77 (2002).
- [82] L. U. Bigliani, R. G. Pollock, L. J. Soslowky, E. L. Flatow, R. J. Pawluk, and V. C. Mow, “Tensile properties of the inferior glenohumeral ligament,” *J. Orthop. Res.* **10**, 187–197 (1992).
- [83] Y. Lanir, “Structure-strength relations in mammalian tendon,” *Biophys. J.* **24**, 541–554 (1978).
- [84] L. J. Gathercole and A. Keller, “Crimp morphology in the fibre-forming collagens,” *Matrix* **11**, 214–234 (1991).
- [85] K. S. Miller, B. K. Connizzo, E. Feeney, and L. J. Soslowky, “Characterizing local collagen fiber re-alignment and crimp behavior throughout mechanical testing in a mature mouse supraspinatus tendon model,” *J. Biomech.* **45**, 2061–2065 (2012).
- [86] T. York, L. Kahan, S. P. Lake, and V. Gruev, “Real-time high-resolution measurement of collagen alignment in dynamically loaded soft tissue,” *J. Biomed. Opt.* **19**, 066011-6 (2014).
- [87] N. W. Skelley, R. M. Castile, T. E. York, V. Gruev, S. P. Lake, and R. H. Brophy, “Differences in the microstructural properties of the anteromedial and posterolateral bundles of the anterior cruciate ligament,” *Am. J. Sports Med.* **43**, 928–936 (2015).
- [88] K. Hayashi and P. Muir, “Etiopathogenesis of cruciate ligament rupture,” in *Adv. Canine Cranial Cruciate Ligament* (John Wiley & Sons, Hoboken, 2011).
- [89] B. de Campos Vidal, “Form birefringence as applied to biopolymer and inorganic material supraorganization,” *Biotech. Histochem.* **85**, 365–378 (2010).
- [90] M. Franchi, M. Fini, M. Quaranta, V. De Pasquale, M. Raspanti, G. Giavaresi, V. Ottani, and A. Ruggeri, “Crimp morphology in relaxed and stretched rat Achilles tendon,” *J. Anat.* **210**, 1–7 (2007).
- [91] L. H. Yahia and G. Drouin, “Collagen structure in human anterior cruciate ligament and patellar tendon,” *J. Mater. Sci.* **23**, 3750–3755 (1988).
- [92] L. H. Yahia and G. Drouin, “Microscopical investigation of canine anterior cruciate ligament and patellar tendon: Collagen fascicle morphology and architecture,” *J. Orthop. Res.* **7**, 243–251 (1989).
- [93] J. Zhu, X. Zhang, Y. Ma, C. Zhou, and Y. Ao, “Ultrastructural and morphological characteristics of human anterior cruciate ligament and hamstring tendons,” *Anat. Rec.* **295**, 1430–1436 (2012).
- [94] M. Franchi, V. Ottani, R. Stagni, and A. Ruggeri, “Tendon and ligament fibrillar crimps

- give rise to left-handed helices of collagen fibrils in both planar and helical crimps,” *J. Anat.* **216**, 301–309 (2010).
- [95] M. Franchi, M. Quaranta, M. Macciocca, L. Leonardi, V. Ottani, P. Bianchini, A. Diaspro, and A. Ruggeri, “Collagen fibre arrangement and functional crimping pattern of the medial collateral ligament in the rat knee,” *Knee Surgery, Sport. Traumatol. Arthrosc.* **18**, 1671–1678 (2010).
- [96] S. M. Wilson and A. Bacic, “Preparation of plant cells for transmission electron microscopy to optimize immunogold labeling of carbohydrate and protein epitopes,” *Nat. Protoc.* **7**, 1716–1727 (2012).
- [97] P. K. Chu and X. Liu, *Biomaterials Fabrication and Processing Handbook* (CRC Press, 2008).
- [98] J. E. Kelleher, T. Siegmund, and R. W. Chan, “Collagen microstructure in the vocal ligament: Initial results on the potential effects of smoking,” *Laryngoscope* **124**, 361–367 (2014).
- [99] N. Y. Ignatieva, A. E. Guller, O. L. Zakharkina, B. Sandnes, A. B. Shekhter, V. A. Kamensky, and A. V. Zvyagin, “Laser-induced modification of the patellar ligament tissue: Comparative study of structural and optical changes,” *Lasers Med. Sci.* **26**, 401–413 (2011).
- [100] H. Chen, X. Zhao, Z. C. Berwick, J. F. Krieger, S. Chambers, and G. S. Kassab, “Microstructure and mechanical property of Glutaraldehyde-treated porcine pulmonary ligament,” *J. Biomech. Eng.* **138**, 1–9 (2016).
- [101] B. de Campos Vidal and M. L. S. Mello, “Structural organization of collagen fibers in chordae tendineae as assessed by optical anisotropic properties and Fast Fourier transform,” *J. Struct. Biol.* **167**, 166–175 (2009).
- [102] B. de Campos Vidal and M. L. S. Mello, “Optical anisotropy of collagen fibers of rat calcaneal tendons: An approach to spatially resolved supramolecular organization,” *Acta Histochem.* **112**, 53–61 (2010).
- [103] N. I. Fisher, “Statistical Analysis of Circular Data,” in *Stat. Anal. Circ. data* (Cambridge University Press, 1993).
- [104] T. Diethe, N. Twomey, and P. Flach, “Bayesian modeling of the temporal aspects of smart home activity with circular statistics,” Springer International Publishing. 279–294 (2015).
- [105] D. L. Butler, E. S. Grood, F. R. Noyes, and R. F. Zernicke, “Biomechanics of ligaments and tendons,” *Exerc. Sport Sci. Rev.* **6**, 125–181 (1978).
- [106] P. Fratzl, “Restraining cross-links responsible for the mechanical properties of collagen fibers: Natural and artificial,” in *Collagen Struct. Mech.* (Springer US, 2008).
- [107] E. Yew and C. Sheppard, “Effects of axial field components on second harmonic generation microscopy,” *Opt. Express* **14**, 1167–1174 (2006).
- [108] W. Maurel, Y. Wu, N. Thalmann, and D. Thalmann, “Soft tissue physiology,” in *Biomech. Model. Soft Tissue Simul.* (Springer Science & Business Media, 2013).
- [109] C. Krafft and J. Popp, “Raman-based technologies for biomedical diagnostics,” in *Compr. Biomed. Phys.* (Newnes, 2014).
- [110] M. Shribak and R. Oldenbourg, “Techniques for fast and sensitive measurements of two-dimensional birefringence distributions,” *Appl. Opt.* **42**, 3009–3017 (2003).
- [111] A. H. Reshak, “Second harmonic generation from thick leaves using the two-photon laser scanning microscope,” *Micron* **40**, 455–462 (2009).
- [112] B. de Campos Vidal, “Image analysis of tendon helical superstructure using interference and polarized light microscopy,” *Micron* **34**, 423–432 (2003).

- [113] S. P. Reese, S. A. Maas, and J. A. Weiss, “Micromechanical models of helical superstructures in ligament and tendon fibers predict large Poisson’s ratios,” *J. Biomech.* **43**, 1394–1400 (2010).
- [114] A. K. Harvey, M. S. Thompson, and S. M. Brady, “Helical crimp model predicts material properties from tendon microstructure,” *Med. Img. Und. Anal.*, 1–5 (2010).
- [115] W. Lee, H. Rahman, M. E. Kersh, and K. C. Toussaint, “Crimp analysis of connective tissue using quantitative second-harmonic generation microscopy,” *Front. Opt. 2017* (2017).
- [116] B. de Campos Vidal, “Crimp as part of a helical structure,” *C. R. Acad. Sci. III.* **318**, 173–178 (1995).
- [117] R. Reichelt, “Scanning electron microscopy,” in *Sci. Microsc.* (Springer, 2007).
- [118] R. F. Egerton, “The scanning electron microscope,” in *Phys. Princ. Electron Microsc.* (Springer, 2016).
- [119] G. Danilatos and R. Postle, “The environmental scanning electron microscope and its applications,” *Scan. Electron Microsc.* 1–16 (1982).
- [120] P. Mestres, N. Pütz, S. Garcia Gómez de las Heras, E. G. Pobleto, A. Morguet, and M. Laue, “The surface topography of the choroid plexus. environmental, low and high vacuum scanning electron microscopy,” *Ann. Anat.* **193**, 197–204 (2011).
- [121] S. E. Kirk, J. N. Skepper, and A. M. Donald, “Application of environmental scanning electron microscopy to determine biological surface structure,” *J. Microsc.* **233**, 205–224 (2009).
- [122] F. S. Utku, E. Klein, H. Saybasili, C. A. Yucesoy, and S. Weiner, “Probing the role of water in lamellar bone by dehydration in the environmental scanning electron microscope,” *J. Struct. Biol.* **162**, 361–367 (2008).
- [123] P. Moran and B. Coats, “Biological sample preparation for SEM imaging of porcine retina,” in *Micros. Today* **20** (2012).
- [124] S. Inaga, S. Hirashima, K. Tanaka, T. Katsumoto, T. Kameie, H. Nakane, and T. Naguro, “Low vacuum scanning electron microscopy for paraffin sections utilizing the differential stainability of cells and tissues with platinum blue,” *Arch. Histol. Cytol.* **72**, 101–106 (2009).
- [125] P. J. R. Uwins, M. Murray, and R. Gould, “Effects of four different processing techniques on the micorstructure of potatoes: Comparison with fresh samples in the ESEM,” *Microsc. Res. Tech.* **25**, 412–418 (1993).
- [126] G. Danilatos, “The examination of fresh or living plant material in an environmental scanning electron microscope,” *J. Microsc.* **121**, 235–238 (1981).
- [127] E. Stabentheiner, A. Zankel, and P. Pölt, “Environmental scanning electron microscopy (ESEM)-a versatile tool in studying plants,” *Protoplasma* **246**, 89–99 (2010).
- [128] J. Winter, “Using the student’s t -test with extremely small sample sizes,” *Pr. Assessment, Res. Evalutaion* **18**, 1–12 (2013).
- [129] T. McMahon, P. C. M. Van Zijl, and A. A. Gilad, “Quantification of collagen organization using fractal dimensions and Fourier transforms,” *Acta Histochem.* **27**, 320–331 (2015).
- [130] W. Lo, W. L. Chen, C. M. Hsueh, A. A. Ghazaryan, S. J. Chen, D. Hui-Kang Ma, C. Y. Dong, and H. Y. Tan, “Fast Fourier transform-based analysis of second-harmonic generation image in keratoconic cornea,” *Investig. Ophthalmol. Vis. Sci.* **53**, 3501–3507 (2012).
- [131] M. D. Johnson and S. C. Mueller, “Three dimensional multiphoton imaging of fresh and whole mount developing mouse mammary glands,” *BMC Cancer* **13**, 373 (2013).

- [132] J. Gehring and A. Zyball, “Radiation crosslinking of polymers - status, current issues, trends and challenges,” *Radiat. Phys. Chem.* **46**, 931–936 (1995).
- [133] J. Gehring, “With radiation crosslinking of engineering plastics into the next millennium,” *Radiat. Phys. Chem.* **57**, 361–365 (2000).
- [134] G. Adler, “Cross-linking of polymers by radiation,” *Science*. **141**, 321–329 (1963).
- [135] K. Shimazaki, M. A. Colombo, E. Moura, and N. Mastro, “Gelatin/piassava composites treated by electron beam radiation,” *Rev. Matéria* **15**, 303–308 (2010).
- [136] H. Mrázová, J. Koller, K. Kubišová, G. Fujeříková, E. Klincová, and P. Babál, “Comparison of structural changes in skin and amnion tissue grafts for transplantation induced by gamma and electron beam irradiation for sterilization,” *Cell Tissue Bank*. **17**, 255–260 (2016).
- [137] B. Jiang, Z. Wu, H. Zhao, F. Tang, J. Lu, Q. Wei, and X. Zhang, “Electron beam irradiation modification of collagen membrane,” *Biomaterials* **27**, 15–23 (2006).
- [138] W. A. Parejo Calvo, C. L. Duarte, L. D. B. Machado, J. E. Manzoli, A. B. C. Geraldo, Y. Kodama, L. G. A. Silva, E. S. Pino, E. S. R. Somessari, et al., “Electron beam accelerators-trends in radiation processing technology for industrial and environmental applications in Latin America and the Caribbean,” *Radiat. Phys. Chem.* **81**, 1276–1281 (2012).
- [139] N. Sartori Blanc, D. Studer, K. Ruhl, and J. Dubochet, “Electron beam-induced changes in vitreous sections of biological samples,” *J. Microsc.* **192**, 194–201 (1998).
- [140] S. Kitching and A. M. Donald, “Beam damage of polypropylene in the environmental scanning electron microscope: An FTIR study,” *J. Microsc.* **190**, 357–365 (1998).
- [141] C. P. Royall, B. L. Thiel, and A. M. Donald, “Radiation damage of water in environmental scanning electron microscopy,” *J. Microsc.* **204**, 185–195 (2001).
- [142] R. F. Egerton, P. Li, and M. Malac, “Radiation damage in the TEM and SEM,” *Micron* **35**, 399–409 (2004).
- [143] A. Boyde and S. J. Jones, “Scanning electron microscopy of bone: Instrument, specimen, and issues,” *Microsc. Res. Tech.* **33**, 92–120 (1996).
- [144] J. E. Mcgregor, Z. Wang, C. Ffrench-Constant, and A. M. Donald, “Microscopy of myelination,” in *Microsc. Sci. Technol. Appl. Educ.* (Formatex Research Center, 2010).
- [145] M. M. Kabir, V. V. G. K. Inavalli, T.-Y. Lau, and K. C. Toussaint, “Application of quantitative second-harmonic generation microscopy to dynamic conditions,” *Biomed. Opt. Express* **4**, 2546–2554 (2013).
- [146] J. Lead and E. Smith, *Environmental and Human Health Impacts of Nanotechnology* (John Wiley & Sons, 2009).
- [147] V. Eroschenko and M. Fiore, *DiFiore’s Atlas of Histology with Functional Correlations* (Lippincott Williams & Wilkins, 2004).
- [148] C. T. Thorpe, H. L. Birch, P. D. Clegg, and H. R. C. Screen, “The role of the non-collagenous matrix in tendon function,” *Int. J. Exp. Pathol.* **94**, 248–259 (2013).
- [149] C. T. Thorpe, C. P. Udeze, H. L. Birch, P. D. Clegg, and H. R. C. Screen, “Specialization of tendon mechanical properties results from interfascicular differences,” *J. R. Soc. Interface* **9**, 3108–3117 (2012).
- [150] C. Gerber, D. C. Meyer, A. G. Schneeberger, H. Hoppeler, and B. von Rechenberg, “Effect of tendon release and delayed repair on the structure of the muscles of the rotator cuff: An experimental study in sheep,” *J. Bone Joint Surg. Am.* **86–A**, 1973–1982 (2004).
- [151] N. W. Skelley, R. M. Castile, P. C. Cannon, C. I. Weber, R. H. Brophy, and S. P. Lake, “Regional variation in the mechanical and microstructural properties of the human anterior cruciate ligament,” *Am J Sport. Med* **44**, 2892–2899 (2016).

- [152] K. Komatsu, L. Mosekilde, A. Viidik, and M. Chiba, “Polarized light microscopic analysis of collagen fibers in the rat incisor periodontal ligament in relation to areas, regions, and ages,” *Anat Rec* **268**, 381–387 (2002).
- [153] J. O. Wright, N. W. Skelley, R. P. Schur, R. M. Castile, S. P. Lake, and R. H. Brophy, “Microstructural and mechanical properties of the posterior cruciate ligament: A comparison of the anterolateral and posteromedial bundles,” *J Bone Jt. Surg Am* **98**, 1656–1664 (2016).
- [154] A. A. Dunkman, M. R. Buckley, M. J. Mienaltowski, S. M. Adams, S. J. Thomas, L. Satchell, A. Kumar, L. Pathmanathan, D. P. Beason, et al., “Decorin expression is important for age-related changes in tendon structure and mechanical properties,” *Matrix Biol* **32**, 3–13 (2013).
- [155] M. R. Hee, D. Huang, E. A. Swanson, and J. G. Fujimoto, “Polarization-sensitive low-coherence reflectometer for birefringence characterization and ranging,” *J. Opt. Soc. Am. B* **9**, 903–908 (1992).
- [156] J. C. Simon, H. Kang, M. Staninec, A. T. Jang, K. H. Chan, L. Darling, R. C. Lee, and D. Fried, “Near-IR and CP-OCT Imaging of Suspected Occlusal Caries Lesions,” *Lasers Surg Med* **49**, 215–224 (2017).
- [157] B. Baumann, E. Götzinger, M. Pircher, H. Sattmann, C. Schütze, F. Schlanitz, C. Ahlers, U. Schmidt-Erfurth, and C. K. Hitzenberger, “Segmentation and quantification of retinal lesions in age-related macular degeneration using polarization-sensitive optical coherence tomography,” *J Biomed Opt* **15**, 061704 (2010).
- [158] S. Zotter, M. Pircher, T. Torzicky, B. Baumann, H. Yoshida, F. Hirose, P. Roberts, M. Ritter, C. Schütze, et al., “Large-field high-speed polarization sensitive spectral domain OCT and its applications in ophthalmology,” *Biomed. Opt Express* **3**, 2720–2732 (2012).
- [159] M. Pircher, E. Goetzinger, R. Leitgeb, and C. K. Hitzenberger, “Three dimensional polarization sensitive OCT of human skin in vivo,” *Opt Express* **12**, 3236–3244 (2004).
- [160] K. H. Kim, M. C. Pierce, G. Maguluri, H. B. Park, S. J. Yoon, M. Lydon, R. Sheridan, and J. F. de Boer, “In vivo imaging of human burn injuries with polarization-sensitive optical coherence tomography,” *J. Biomed. Opt.* **17**, 066012 (2012).
- [161] Z. Liu, D. Pouli, D. Sood, A. Sundarakrishnan, C. K. Hui, L. M. Arendt, C. Alonzo, K. P. Quinn, C. Kuperwasser, et al., “Automated quantification of three-dimensional organization of fiber-like structures in biological tissues,” *Biomaterials* **116**, 34–47 (2017).
- [162] R. M. Kottmann, J. Sharp, K. Owens, P. Salzman, G. Xiao, R. P. Phipps, P. J. Sime, E. B. Brown, and S. W. Perry, “Second harmonic generation microscopy reveals altered collagen microstructure in usual interstitial pneumonia versus healthy lung,” *Respir. Res.* **16**, 1–13 (2015).
- [163] N. Morishige, N. Yamada, S. Teranishi, T. Chikama, T. Nishida, and A. Takahara, “Detection of subepithelial fibrosis associated with corneal stromal edema by second harmonic generation imaging microscopy,” *Invest Ophthalmol Vis Sci* **50**, 3145–3150 (2009).
- [164] A. Pena, A. Fabre, D. Debarre, J. Marchal-Somme, B. Crestani, J.-L. Martin, E. Beaurepaire, and M.-C. Schanne-Klein, “Three-dimensional investigation and scoring of extracellular matrix remodeling during lung fibrosis using multiphoton microscopy,” *Microsc. Res. Tech* **70**, 162–170 (2007).
- [165] K. E. Eliceiri, P. J. Campagnola, M. Patankar, P. J. Keely, V. Ajeti, K. Tilbury, and M. A. Brewer, “SHG imaging of cancer,” *Biomed. Opt. 3D Imaging OSA 2012*, (2012).

- [166] Z. Liu, K. P. Quinn, L. Speroni, L. Arendt, C. Kuperwasser, C. Sonnenschein, A. M. Soto, and I. Georgakoudi, "Rapid three-dimensional quantification of voxel-wise collagen fiber orientation," *Biomed. Opt Express* **6**, 2294–2310 (2015).
- [167] M. B. Lilledahl, D. M. Pierce, T. Ricken, G. A. Holzapfel, and C. D. L. Davies, "Structural analysis of articular cartilage using multiphoton microscopy: Input for biomechanical modeling," *IEEE Trans Med Imaging* **30**, 1635–1648 (2011).
- [168] T. C. Gasser, R. W. Ogden, and G. A. Holzapfel, "Hyperelastic modelling of arterial layers with distributed collagen fibre orientations," *J. R. Soc. Interface* **3**, 15–35 (2006).
- [169] M. S. Sacks, "Incorporation of experimentally-derived fiber orientation into a structural constitutive model for planar collagenous tissues," *J Biomech Eng* **125**, 280–287 (2003).
- [170] R. Grytz and G. Meschke, "Constitutive modeling of crimped collagen fibrils in soft tissues," *J. Mech. Behav. Biomed. Mater.* **2**, 522–533 (2009).
- [171] M. W. Pickup, J. K. Mouw, and V. M. Weaver, "The extracellular matrix modulates the hallmarks of cancer," *EMBO Rep.* **15**, 1243–1253 (2014).
- [172] J. K. Kular, S. Basu, and R. I. Sharma, "The extracellular matrix : Structure , composition , age-related differences , tools for analysis and applications for tissue engineering," *J Tissue Eng* **5**, 1–17 (2014).
- [173] M. A. Meyers, P.-Y. Chen, A. Y.-M. Lin, and Y. Seki, "Biological materials: Structure and mechanical properties," *Prog. Mater. Sci.* **53**, 1–206 (2008).
- [174] P. A. Netti, D. A. Berk, M. A. Swartz, A. J. Grodzinsky, and R. K. Jain, "Role of extracellular matrix assembly in interstitial transport in solid tumors," *Cancer Res* **60**, 2497–2503 (2000).
- [175] G. Wollensak, E. Spoerl, and T. Seiler, "Stress-strain measurements of human and porcine corneas after riboflavin-ultraviolet-A-induced cross-linking," *J Cataract Refract Surg* **29**, 1780–1785 (2003).
- [176] C. S. Chamberlain, E. M. Crowley, H. Kobayashi, K. W. Eliceiri, and R. Vanderby, "Quantification of collagen organization and extracellular matrix factors within the healing ligament," *Microsc Microanal* **17**, 779–787 (2011).
- [177] S. L. M. Dahl, M. E. Vaughn, and L. E. Niklason, "An ultrastructural analysis of collagen in tissue engineered arteries," *Ann Biomed Eng* **35**, 1749–1755 (2007).
- [178] C. J. Doillon, M. G. Dunn, E. Bender, and F. H. Silver, "Collagen fiber formation in repair tissue: Development of strength and toughness," *Coll. Relat. Res.* **5**, 481–492 (1985).
- [179] P. Fratzl, "Collagen in arterial walls: Biomechanical aspects," in *Collagen Struct. Mech.* (Springer US, 2008).
- [180] M. Franchi, A. Trirè, M. Quaranta, E. Orsini, and V. Ottani, "Collagen structure of tendon relates to function," *ScientificWorldJournal.* **7**, 404–420 (2007).
- [181] L. Zhao, A. Thambyah, and N. Broom, "Crimp morphology in the ovine anterior cruciate ligament," *J. Anat.* **226**, 278–288 (2015).
- [182] A. Freed and T. C. Doehring, "Elastic model for crimped collagen fibrils," *J. Biomech. Eng.* **127**, 587–593 (2005).
- [183] J.-Y. Rho, L. Kuhn-Spearing, and P. Zioupos, "Mechanical properties and the hierarchical structure of bone," *Med. Eng. Phys.* **20**, 92–102 (1998).
- [184] P. Kannus, "Structure of the tendon connective tissue," *Scand. J. Med. Sci. Sport.* **10**, 312–320 (2000).
- [185] J. Canny, "A computational approach to edge detection," *IEEE Trans. Pattern Anal. Mach. Intell.* **PAMI-8**, 679–698 (1986).

- [186] R. H. Bamberger and M. J. T. Smith, “A filter bank for the directional decomposition of images: Theory and design,” *IEEE Trans. Signal Process.* **40**, 882–893 (1992).
- [187] “3D arrow with many color/parameter options,” *MATLAB Cent. File Exch.*, 2006, <<https://www.mathworks.com/matlabcentral/fileexchange/12274-3d-arrow-with-many-color-parameter-options>>.
- [188] K. V. Mardia, “Distributions on spheres,” in *Stat. Dir. Data* (Academmic Press, 2014).
- [189] M. Shen, Y. Tian, S. P. Chong, J. Zhao, H. Zeng, and S. Tang, “Quantifying the backscattering of second harmonic generation in tissues with confocal multiphoton microscopy,” *J. Biomed. Opt.* **18**, 115003 (2013).
- [190] C. T. Thorpe, H. L. Birch, P. D. Clegg, and H. R. C. Screen, “Tendon physiology and mechanical behavior: Structure-function relationships,” in *Tendon Regen* (Academmic Press, 2015).
- [191] A. Fedorov, R. Beichel, J. Kalpathy-Cramer, J. Finet, J.-C. Fillion-Robbin, S. Pujol, C. Bauer, D. Jennings, F. Fennessy, et al., “3D slicer as an image computing platform for the quantitative imaging network,” *Magn Reson Imaging* **30**, 1323–1341 (2012).
- [192] Z. Liang, F. E. Boda, R. T. Constable, E. M. Haacke, P. C. Lauterbur, and M. R. Smith, “Constrained reconstruction methods in MR Imaging,” *Rev. Magn. Reson. Med.* **4**, 67–185 (1992).
- [193] B. R. Freedman, A. Zuskov, J. J. Sarver, M. R. Buckley, and L. J. Soslowsky, “Evaluating changes in tendon crimp with fatigue loading as an ex vivo structural assessment of tendon damage,” *J Orthop Res* **33**, 904–910 (2015).
- [194] M. Franchi, P. Torricelli, G. Giavaresi, and M. Fini, “Role of moderate exercising on Achilles tendon collagen crimping patterns and proteoglycans,” *Connect. Tissue Res.* **54**, 267–274 (2013).
- [195] O. Waisbourd-Zinman, H. Koh, S. Tsai, P. M. Lavrut, C. Dang, X. Zhao, M. Pack, J. Cave, M. Hawes, et al., “The toxin biliatresone causes mouse extrahepatic cholangiocyte damage and fibrosis through decreased glutathione and SOX17,” *Hepatology* **64**, 880–893 (2016).
- [196] G. Khandekar, J. Llewellyn, A. Kriegermeier, O. Waisbourd-Zinman, N. Johnson, Y. Du, R. Giwa, X. Liu, T. Kisseleva, et al., “Coordinated development of the mouse extrahepatic bile duct: Implications for neonatal susceptibility to biliary injury,” *bioRxiv* (2019).
- [197] N. Kobelska-Dubiel, B. Klinecicz, and W. Cichy, “Liver disease in cystic fibrosis,” *Prz. Gastroenterol.* **9**, 136–141 (2014).
- [198] M. Ahmed, “Acute cholangitis - an update.,” *World J. Gastrointest. Pathophysiol.* **9**, 1–7 (2018).
- [199] P. C. Benias, R. G. Wells, B. Sackey-Aboagye, H. Klavan, J. Reidy, D. Buonocore, M. Miranda, S. Kornacki, M. Wayne, et al., “Structure and distribution of an unrecognized interstitium in human tissues,” *Sci. Rep.* **8**, 1–8 (2018).
- [200] T. Sellaro, D. Hildebrand, Q. Lu, N. Vyanahare, M. Scott, and M. Sacks, “Effects of collagen fiber orientation on the response of biologically derived soft tissue biomaterials to cyclic loading,” *J Biomed Mater Res A* **80**, 194–205 (2007).
- [201] E. M. Spiesz, C. T. Thorpe, P. J. Thurner, and H. R. C. Screen, “Structure and collagen crimp patterns of functionally distinct equine tendons, revealed by quantitative polarised light microscopy (qPLM),” *Acta Biomater.* **70**, 281–292 (2018).
- [202] V. Ayyalasomayajula, B. Pierrat, and P. Badel, “A computational model for understanding the micro-mechanics of collagen fiber network in the tunica adventitia,” *Biomech. Model. Mechanobiol.* (2019).

- [203] K. S. Miller, B. K. Connizzo, E. Feeney, J. J. Tucker, and L. J. Soslowsky, “Examining differences in local collagen fiber crimp frequency throughout mechanical testing in a developmental mouse supraspinatus tendon model,” *J. Biomech. Eng.* **134**, 041004 (2012).
- [204] T. K. Tonge, J. W. Ruberti, and T. D. Nguyen, “Micromechanical modeling study of mechanical inhibition of enzymatic degradation of collagen tissues,” *Biophys. J.* **109**, 2689–2700 (2015).
- [205] Y. Kuboki, T. Takagi, S. Sasaki, S. Saito, and G. L. Mechanic, “Comparative collagen biochemistry of bovine periodontium, gingiva, and dental pulp,” *J Dent Res* **60**, 159–163 (1981).
- [206] T. Ida, K. Uoshima, M. Nagasawa, J. M. Rosales Rocabado, M. Kitami, M. Yamauchi, M. Terajima, Y. Akiba, and M. Kaku, “Extracellular matrix with defective collagen cross-linking affects the differentiation of bone cells,” *PLoS One* **13**, e0204306 (2018).
- [207] M. Terajima, I. Perdivara, M. Sricholpech, Y. Deguchi, N. Pleshko, K. B. Tomer, and M. Yamauchi, “Glycosylation and cross-linking in bone type I collagen,” *J. Biol. Chem.* **289**, 22636–22647 (2014).
- [208] K. M. Myers, H. Feltovich, E. Mazza, J. Vink, M. Bajka, R. J. Wapner, T. J. Hall, and M. House, “The mechanical role of the cervix in pregnancy,” *J. Biomech.* **48**, 1511–1523 (2015).
- [209] H. Feltovich, T. J. Hall, and V. Berghella, “Beyond cervical length: Emerging technologies for assessing the pregnant cervix,” *Am. J. Obstet. Gynecol.* **207**, 345–354 (2012).
- [210] H. Feltovich and M. House, “Innovative methods of cervical assessment and potential for novel treatment,” *Clin Obs. Gynecol* **57**, 531–536 (2014).
- [211] B. L. McFarlin, J. Balash, V. Kumar, T. A. Bigelow, X. Pombar, J. S. Abramowicz, and W. D. O’Brien Jr., “Development of an ultrasonic method to detect cervical remodeling in vivo in full-term pregnant women,” *Ultrasound Med Biol* **41**, 2533–2539 (2015).
- [212] Y. Gan, W. Yao, K. M. Myers, J. Y. Vink, R. J. Wapner, and C. P. Hendon, “Analyzing three-dimensional ultrastructure of human cervical tissue using optical coherence tomography,” *Biomed. Opt. Express* **6**, 1090 (2015).
- [213] W. Yao, Y. Gan, K. M. Myers, J. Y. Vink, R. J. Wapner, and P. Hendon, “Collagen fiber orientation and dispersion in the upper cervix of non-pregnant and pregnant women,” *PLoS One* **11**, 1–20 (2016).
- [214] Y. Zhang, M. L. Akins, K. Murari, J. Xi, M. Li, and K. Luby-phelps, “A compact fiber-optic SHG scanning endomicroscope and its application to visualize cervical remodeling during pregnancy,” *PNAS* **109**, 12878–12883 (2012).
- [215] L. M. Reusch, L. C. Carlson, P. J. Campagnola, K. W. Eliceiri, and T. J. Hall, “Nonlinear optical microscopy and ultrasound imaging of human cervical structure,” *J. Biomed. Opt.* **18**, 031110 (2013).
- [216] H. Jia, Y. Wang, R. Harris, J. Vink, K. Myers, and E. Donnelly, “Characterization of the collagen microstructural organization of human cervical tissue,” *Reproduction* **156**, 71–79 (2018).
- [217] C.-K. Tsai, Y.-S. Chen, P.-C. Wu, T.-Y. Hsieh, H.-W. Liu, C.-Y. Yeh, W.-L. Lin, J.-S. Chia, and T.-M. Liu, “Imaging granularity of leukocytes with third harmonic generation microscopy,” *Biomed. Opt. Express* **3**, 2234–2243 (2012).
- [218] D. Debarre, W. Supatto, A.-M. Pena, A. Fabre, T. Tordjmann, L. Combettes, M.-C. Schanne-Klein, and E. Beaurepaire, “Imaging lipid bodies in cells and tissues using third-harmonic generation microscopy,” *Nat. Methods* **3**, 47–53 (2006).

- [219] S. Witte, A. Negrean, J. C. Lodder, C. P. J. de Kock, G. Testa Silva, H. D. Mansvelder, and M. Louise Groot, “Label-free live brain imaging and targeted patching with third-harmonic generation microscopy,” *PNAS* **108**, 5970–5975 (2011).
- [220] L. A. Torre, F. Bray, R. L. Siegel, J. Ferlay, J. Lortet-Tieulent, and A. Jemal, “Global cancer statistics, 2012,” *CA. Cancer J. Clin.* **65**, 87–108 (2015).
- [221] P. Bindhu, R. Krishnapillai, P. Thomas, and P. Jayanthi, “Facts in artifacts,” *J. Oral Maxillofac. Pathol.* **17**, 397–401 (2013).
- [222] G. H. C. New and J. F. Ward, “Optical third-harmonic generation in gases,” *Phys. Rev. Lett.* **19**, 556–559 (1967).
- [223] Muller, Squier, Wilson, and Brakenhoff, “3D microscopy of transparent objects using third-harmonic generation,” *J. Microsc.* **191**, 266–274 (1998).
- [224] J. A. Squier, M. Müller, G. J. Brakenhoff, and K. R. Wilson, “Third harmonic generation microscopy,” *Opt. Express* **3**, 315–324 (1998).
- [225] V. A. Loiko, G. I. Ruban, O. A. Gritsai, A. D. Gruzdev, S. M. Kosmacheva, N. V. Goncharova, and A. A. Miskevich, “Morphometric model of lymphocyte as applied to scanning flow cytometry,” *J. Quant. Spectrosc. Radiat. Transf.* **102**, 73–84 (2006).
- [226] N. Anderson, “Color atlas of differential diagnosis in exfoliative and aspiration cytopathology,” *J. Clin. Pathol.* **52**, 629–630 (1999).
- [227] J. I. Pitt and A. D. Hocking, *Fungi and Food Spoilage* (Springer US, 2009).
- [228] Y. Barad, H. S. Eisenberg, M. Horowitz, and Y. R. Silberberg, “Nonlinear scanning laser microscopy by third harmonic generation,” *Appl. Phys. Lett* **70**, 922–924 (1997).
- [229] P. Wang, R. K. Bista, W. Qiu, W. E. Khalbuss, L. Zhang, R. E. Brand, and Y. Liu, “An insight into statistical refractive index properties of cell internal structure via low-coherence statistical amplitude microscopy,” *Opt. Express* **18**, 21950–21958 (2010).